

© 2014 by Kevin Zielnicki. All rights reserved.

PURE SOURCES AND EFFICIENT DETECTORS FOR OPTICAL QUANTUM
INFORMATION PROCESSING

BY

KEVIN ZIELNICKI

DISSERTATION

Submitted in partial fulfillment of the requirements
for the degree of Doctor of Philosophy in Physics
in the Graduate College of the
University of Illinois at Urbana-Champaign, 2014

Urbana, Illinois

Doctoral Committee:

Professor Lance Cooper, Chair
Professor Paul Kwiat, Director of Research
Professor Steve Errede
Professor John Stack

Abstract

Over the last sixty years, classical information theory has revolutionized the understanding of the nature of information, and how it can be quantified and manipulated. Quantum information processing extends these lessons to quantum systems, where the properties of intrinsic uncertainty and entanglement fundamentally defy classical explanation. This growing field has many potential applications, including computing, cryptography, communication, and metrology. As inherently mobile quantum particles, photons are likely to play an important role in any mature large-scale quantum information processing system. However, the available methods for producing and detecting complex multi-photon states place practical limits on the feasibility of sophisticated optical quantum information processing experiments.

In a typical quantum information protocol, a source first produces an interesting or useful quantum state (or set of states), perhaps involving superposition or entanglement. Then, some manipulations are performed on this state, perhaps involving quantum logic gates which further manipulate or entangle the initial state. Finally, the state must be detected, obtaining some desired measurement result, e.g., for secure communication or computationally efficient factoring. The work presented here concerns the first and last stages of this process as they relate to photons: sources and detectors.

Our work on sources is based on the need for optimized non-classical states of light delivered at high rates, particularly of single photons in a pure quantum state. We seek to better understand the properties of spontaneous parametric downconversion (SPDC) sources of photon pairs, and in doing so, produce such an optimized source. We report an SPDC source which produces pure heralded single photons with little or no spectral filtering, allowing a significant rate enhancement.

Our work on detectors is based on the need to reliably measure single-photon states. We have focused on optimizing the detection efficiency of visible light photon counters (VLPCs), a single-photon detection technology that is also capable of resolving photon number states. We report a record-breaking quantum efficiency of $91 \pm 3\%$ observed with our detection system. Both sources and detectors are independently interesting physical systems worthy of study, but together they promise to enable entire new classes and applications of information based on quantum mechanics.

Acknowledgments

Thank you to everyone who supported me on this long strange trip, in good times and in hard times. Thanks especially to my parents, Robert and Eugenia Zielnicki. I am who I am mostly because of you (my dad might try to tell you different, but don't listen to him).

Thanks also to all my other friends and family: everyone I have learned from, joked with, debated, loved, and shared incredible adventures with. If you're reading this, that almost certainly includes *you*. So thank you for being there. I'm honored to know all of you, more than I can find the words to express.

Funding for this work has been provided in part by NSF Grant No. PHY 09-03865 ARRA, NASA Grant No. NNX13AP35A and Office of Naval Research (ONR) Grant No. N00014-13-1-0627. This money comes from your taxes; funding for science only happens because we as a society continue to decide that it should.

Speaking of funding, a special thanks is due to Paul Kwiat. Paul is an imperturbable zen master, an exceptionally dedicated scientist, and an unmatched advisor.

Finally, this document originally contained many missing hyphens, typos, ambiguous antecedents, inelegant turns of phrase, incomplete explanations, and other unseemliness. Surely some of these remain, but this dissertation was greatly improved by the dedicated editorial work of Paul Kwiat and Rebecca Holmes.

Table of Contents

A Note on Electronic Formatting	vi
List of Tables	vii
List of Figures	viii
List of Abbreviations	x
Chapter 1 Scalable Optical Quantum Information Processing	1
1.1 Introduction to Engineered Photon Pair Sources	1
1.1.1 Introduction to Spontaneous Parametric Downconversion	2
1.1.2 Motivation: Indistinguishability	5
1.1.3 Motivation: Unentanglement for Entanglement’s Sake	8
1.2 Introduction to Efficient Photon-Number Resolving Detectors	11
Chapter 2 Engineering Unentanglement	13
2.1 A Simple Model	13
2.1.1 Schmidt Modes	14
2.1.2 The Spectrally Filtered Source	16
2.2 A Sophisticated Model	17
2.2.1 The Engineered Source	18
2.3 Polarization Entanglement	21
2.3.1 Two-crystal Scheme	21
2.3.2 Which-Crystal Distinguishability	22
2.3.3 Measuring Entanglement	23
2.3.4 Migdall Effect	24
2.4 Preview: Characterizing the Engineered Source	25
Chapter 3 Measuring the Joint Spectrum	27
3.1 Overview of Joint Spectral Measurement	27
3.2 Fourier Spectroscopy	29
3.2.1 Two-Dimensional Fourier Spectroscopy	30
3.2.2 Diagonal Fourier Spectroscopy	31
3.2.3 Measurements	32
3.3 Fiber Spectroscopy	35
3.3.1 Calibration	36
3.3.2 Joint Spectral Measurement and Simulation	40
Chapter 4 Measuring Heralded Photon Purity	43
4.1 Correlation Function Measurement	43
4.1.1 Photon Bunching	43
4.1.2 Electric Field Correlation Functions	45
4.1.3 Measuring Photon Correlation	46
4.2 Two-Source Hong-Ou-Mandel Interference	50

Chapter 5	Detector Operation and Characterization	53
5.1	VLPC Operation	54
5.2	Measurement Apparatus	56
5.3	Photon Counting	59
5.3.1	Pulse Height Analysis	59
5.3.2	Photon Number Resolution	61
5.3.3	Pulse Area Analysis	61
Chapter 6	Detector Optimization	63
6.1	Anti-reflection Coating	64
6.2	Fiber selection	67
6.3	Saturation Effects	68
6.4	Proposed Modifications	71
6.4.1	Detector Area	71
6.4.2	Wavelength Sensitivity	72
Chapter 7	Conclusions	73
7.1	Unentangled Source	73
7.2	Detectors	74
7.3	Final Thoughts	74
Appendix A	Dispersion Effects	77
A.1	Introduction to Dispersion	77
A.2	Transform-Limited Pulses	78
A.3	Temporal Profile Measurement	82
A.3.1	Autocorrelation	82
A.3.2	FROG	82
A.4	Prism Compression	84
A.5	Doubling 810 \rightarrow 405 nm	85
A.5.1	Lens Selection	85
A.5.2	Crystal Thickness	86
References		88

A Note on Electronic Formatting

If you are reading a printed copy of this document, you may notice that numbers in the text referring to figures, chapters, sections, and references are blue or violet; please ignore this, I hope it is not distracting.

If you are reading a PDF copy, I've tried to take advantage of the medium to make the use of this document as reference a little bit easier. So, clicking a page number in the table of contents will take you to that location in the text. Similarly, clicking on a reference in the text to a particular figure, footnote, section, or citation will take you to that location in the document. Finally, clicking on a journal article reference in the bibliography will open that journal article in your web browser, using the Document Object Identifier system. This is made possible by the admirable work of the L^AT_EX open source community and by the International DOI Foundation.

List of Tables

2.1	Conditions for SPDC separability	20
2.2	Comparison of experimental characterization techniques for the joint spectrum	26
6.1	VLPC troubleshooting	65
A.1	Minimum time-bandwidth products for various pulse shapes.	79
A.2	Lens comparison	86

List of Figures

1.1	Energy and momentum conservation in SPDC	4
1.2	Diagram of Hong-Ou-Mandel interferometer	5
1.3	Beamsplitter bunching and the Hong-Ou-Mandel dip	6
1.4	Quantum repeater for quantum communication	9
2.1	Simple filtered JSI model	15
2.2	Schmidt decomposition of modeled JSI	15
2.3	Schmidt modes of the JSI	15
2.4	Phase-matching correlations in SPDC	19
2.5	SPDC source geometry	20
2.6	Joint spectral dependence on emission angle	21
2.7	Polarization entanglement schematic	22
2.8	Measurement of polarization interference	24
3.1	Phase correlation in the joint spectrum	29
3.2	Fourier spectroscopy with Michelson interferometers	30
3.3	Diagonal Fourier spectroscopy	31
3.4	Fourier spectroscopy schematic	33
3.5	Measured joint spectrum from Fourier spectroscopy	34
3.6	Purity vs. pump bandwidth	34
3.7	Fiber spectroscopy schematic	35
3.8	Fiber spectroscopy jitter	37
3.9	Detector jitter comparison	38
3.10	Fiber dispersion calibration	39
3.11	Simulation of fiber spectroscopy jitter	40
3.12	Comparison of joint spectrum measurements	42
4.1	Simulated photon statistics	44
4.2	Correlation function measurement scheme	48
4.3	Correlation function measurement results	49
4.4	Two-source HOM interferometer	49
4.5	Measured two-source HOM interference	51
5.1	Simulated VLPC saturation	55
5.2	VLPC device structure	56
5.3	VLPC Jitter	56
5.4	Cryogenic detector system	57
5.5	Copper block detail	58
5.6	Four-channel analyzer schematic	60
5.7	VLPC signal detection	61
6.1	Measured VLPC SiO ₂ layer thickness	64

6.2	VLPC reflectivity measurements	66
6.3	Measured PMMA transmission	68
6.4	VLPC saturation simulation	70
6.5	VLPC detector area effect on QE	71
7.1	Word frequency trends	75
A.1	Dispersion in human vision	78
A.2	Dispersion curve in BBO	79
A.3	Chirped pulse field and spectrogram	81
A.4	Pulse broadening from dispersion	81
A.5	Autocorrelation schematic	83
A.6	Autocorrelation measurements	83
A.7	Prism compressor	84
A.8	Lens dispersion	85

List of Abbreviations

APD	Avalanche photodiode
AR	Anti-reflection
BBO	Barium borate
BS	Beamsplitter
ENF	Excess noise factor
EPR	Einstein-Podolsky-Rosen
FCA	Four-channel analyzer
FROG	Frequency-resolved optical gating
FWHM	Full width at half maximum
GDD	Group delay dispersion
GVD	Group velocity dispersion
HOM	Hong-Ou-Mandel
HWP	Half-wave plate
IR	Infrared
JSI	Joint-spectral intensity
JTPA	Joint two-photon amplitude
PBS	Polarizing beamsplitter
PD	Photodiode
PMMA	Poly(methyl methacrylate)
PNR	Photon number resolution
QE	Quantum efficiency
QM	Quantum mechanics
RF	Radio frequency
SHG	Second-harmonic generation
SPDC	Spontaneous parametric downconversion

SSPM	Solid State Photomultiplier
TPA	Two-photon amplitude
TTL	Transistor-transistor logic
UV	Ultraviolet
VLPC	Visible light photon counter

Chapter 1

Scalable Optical Quantum Information Processing

*Make and Detect Quantum States of Light With
This One Weird Trick*

Alternate dissertation title, Buzzfeed edition

Non-classical¹ light has found diverse uses from producing entanglement [1], tests of quantum nonlocality [2], and quantum teleportation [3, 4], to practical applications like cryptography [5, 6] and quantum computation [7, 8]. However, quantum cryptography and computation² are limited by the difficulty of coaxing many quantum states to interact with each other over a long period of time without introducing undesired systematic errors or being forced out of the quantum regime by decoherence. A truly large-scale system would have implications from long-distance high-data-rate secure communication to efficiently factoring the large numbers that form the basis of classical public-key cryptography [11], but such a system remains out of reach. There is an enormous, multi-disciplinary effort dedicated to realizing such a system, of which this work is just one small part. We will focus on two critical aspects of any optical quantum information processing system: sources and detectors. Section 1.1 introduces sources of non-classical light and describes some of the difficulties encountered when optimizing such sources for scalable optical quantum information processing. Of course, generating and manipulating quantum states of light has little purpose if these states cannot be meaningfully resolved, and Section 1.2 describes the need for efficient single-photon detectors in addressing this issue.

1.1 Introduction to Engineered Photon Pair Sources

Pairs of polarization-entangled photons are a critical resource for optical quantum information processing. The nonlinear optical process of spontaneous downconversion is commonly used to produce photon pairs,

¹That is, light which exhibits properties beyond classical electromagnetism.

²Quantum cryptography and computation are not discussed in detail in this work. In short, quantum cryptography delivers provably secure encryption by detecting potential eavesdroppers using the property that quantum measurement fundamentally alters the state being measured [9]. Quantum computation generalizes classical computation using *qubits* as the fundamental unit of information. In contrast to bits (which have a definite value of 0 or 1), qubits can be in superposition states $\alpha|0\rangle + \beta|1\rangle$, and can be entangled with other qubits [10].

usually with additional (and often undesirable) correlations in frequency and spatial mode [12, 13]. Typical sources achieve high purity using spectral filtering, but this significantly decreases source brightness. We have implemented a method which uses group-velocity matching and a broad bandwidth pump to engineer a factorable source (i.e., free of correlations) with much higher brightness than a typical spectrally filtered source. This Section provides some background on the phenomena that we take advantage of to generate these photon pairs, as well as a description of what a factorable source is and motivation for why we would concern ourselves with designing and building one. Chapter 2 follows with more details of precisely how such a source is designed, and Chapters 3-4 describe the principles, methods, and results of characterizing this source.

1.1.1 Introduction to Spontaneous Parametric Downconversion

Spontaneous parametric downconversion (SPDC) is well known as the technique of choice for producing pairs of photons to study and exploit the non-classical nature of light. Here we will go over some of the relevant details of this process, but much more has been written about SPDC and its applications in optical quantum information [1, 14, 15].

Creating Photon Pairs

Spontaneous parametric downconversion is a long name for a relatively simple process. We could leave it at that, but names are chosen for a reason³ and there’s insight in exploring this, so let’s unpack the name. SPDC is commonly referred to as just *downconversion*, which captures the essential nature of the process: one high-energy pump photon converts downward in energy to two “daughter” photons. The process is *spontaneous* because it happens randomly, stimulated by vacuum fluctuations (in contrast to an optical parametric amplifier, which amplifies an input signal beam). The use of *parametric* is more esoteric. In optics, the term refers to a process that leaves the state of the system unaltered (that is to say, any interactions with the nonlinear medium are instantaneous, no energy is deposited or removed, and the medium remains in the same state). The historic use of the term arises from the mathematical study of parametric oscillators, a generalization of the harmonic oscillator in which the parameters (coefficients) in the differential equation are allowed to vary in time. In the field of electronics, this is used in a parametric amplifier to amplify a signal in the presence of a pump. This also explains the origin of the terms “signal” and “idler” for the daughter photons: in an optical parametric amplifier (the optical analog of the parametric amplifier which

³What’s in a name? that which we call a rose
by any other name would smell as sweet
but an ideal technical term should be
memorable and evocative of the thing that it names.

acts on light rather than electronic signals), the signal is the input beam being amplified, while the idler is the unintended secondary beam produced to maintain energy and momentum conservation.

SPDC is a nonlinear optical process, and the full theoretical background is beyond the scope of this work, but an excellent treatment is given by Boyd [16]. For our purposes, it is enough to know that some materials⁴ exhibit induced electric dipoles that vary as the square (or higher powers) of the optical field strength. In SPDC, it is this second-order nonlinear susceptibility $\chi^{(2)}$ in an optical medium that leads to the conversion of a single pump photon into two daughter photons. It’s worth a moment of reflection that this process is doubly strange: it lies outside the scope of not just linear optics, but classical optics as well, being fundamentally a quantum effect (because it relies on non-classical vacuum fluctuations).

It is precisely this quantum nature that we will take advantage of. For example, because the daughter photons are always produced in pairs, and because SPDC satisfies conservation of energy and momentum, detection of a single photon always indicates the presence of exactly one other “heralded” photon at a known position in space and time [17]. This simple property by itself provides for generation of (probabilistic) single-photon states, and can be generalized to produce many other non-classical states of light, including n -photon “Fock” states, squeezed light, and entangled states (in various degrees of freedom, including polarization, time, frequency, and spatial mode). Polarization entanglement is a particularly useful resource, and is discussed in detail in Sec. 2.3. First we will look at phase-matching, which governs the conditions under which SPDC occurs by accounting for momentum conservation.

Phase-matching in SPDC

The fact that the state of the optical medium is unchanged by SPDC implies that energy is conserved between the pump and signal and idler photons. This is easily satisfied by requiring the frequency relationship

$$\nu_p = \nu_s + \nu_i, \tag{1.1}$$

where ν_p is the pump frequency and ν_s and ν_i are the respective signal and idler frequencies (shown in Fig. 1.1). This relationship is exact for a monochromatic pump, or otherwise is conserved within the envelope of the pump bandwidth. The implications of energy conservation are analyzed in Sec. 2.1. We know that momentum must be conserved as well, but this is more challenging, primarily due to the dependence of

⁴The crystal geometries of certain materials (including β -barium borate, bismuth borate, lithium triborate, lithium niobate and potassium titanyl phosphate) lead to particularly high $\chi^{(2)}$ nonlinear susceptibilities.

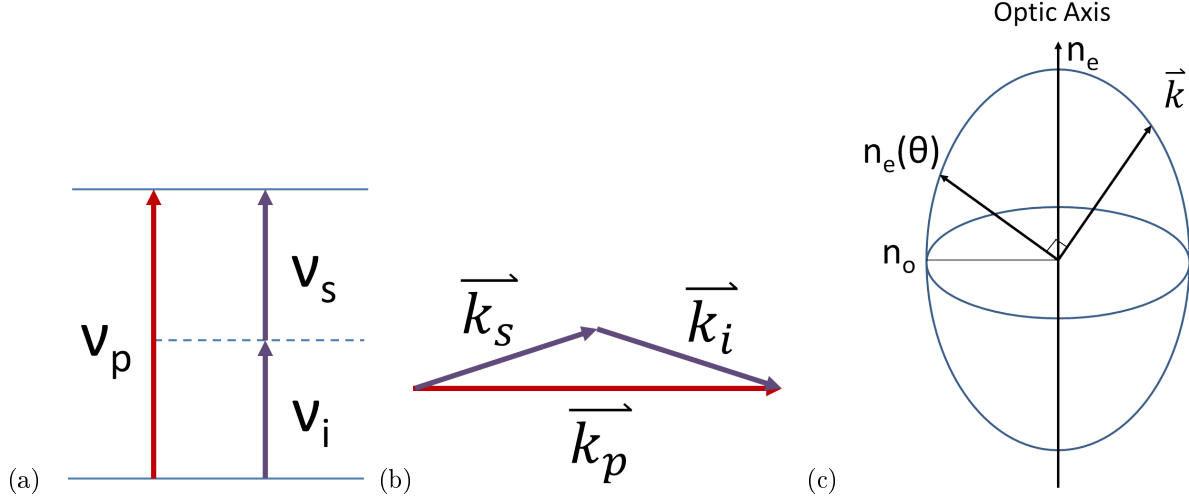


Figure 1.1: Diagram of (a) energy and (b) momentum conservation between the pump, signal, and idler photons in SPDC. For degenerate SPDC, the signal and idler photons each have half the energy of the pump. For degenerate type-I SPDC, the signal and idler have identical longitudinal momentum, and equal transverse momentum in opposite directions. The signal and idler momenta depend on an index of refraction which varies depending on the angle between the propagation direction and optic axis, characterized by the “index ellipsoid” shown in (c).

index of refraction on wavelength. Specifically, the momentum of light in a medium is given by

$$p = \frac{n(\nu)h\nu}{c}, \quad (1.2)$$

where ν is the frequency of the photon and $n(\nu)$ is the frequency-dependent index of refraction.⁵ In typical materials, this index is smaller for lower frequencies and larger for higher frequencies⁶, which leads to a problem for SPDC: the lower-frequency daughter photons together have less momentum than the higher-frequency pump photon, so momentum cannot be conserved!

Fortunately, we can take advantage of birefringent materials to circumvent this problem. Such materials have an index of refraction which depends on the polarization of a photon with respect to an optic axis, with a high-index “slow” axis and a low-index “fast” axis. Thus, we can obtain downconversion by starting with a low-momentum “fast” pump photon. The characteristics of the source vary significantly depending on where we go from here, with two types of phase-matching being commonly used in bulk optics. If we convert from a fast pump photon to two slow daughter photons, this is known as *type-I* phase-matching, and has a

⁵Somewhat counter-intuitively, a photon in a high-index material has more momentum than a photon in a low-index material, even though it is traveling at a slower speed. This can be explained by observing that the photon in the high-index material has a shorter wavelength, and that photon momentum in terms of wavelength is $p = h/\lambda$.

⁶This is *normal dispersion*, the same effect that causes blue light to be deflected most strongly by prisms and appear as the inner arc in rainbows. The opposite relationship, *anomalous dispersion*, can be observed at certain frequencies in certain materials. See Appendix A for more details about dispersion.

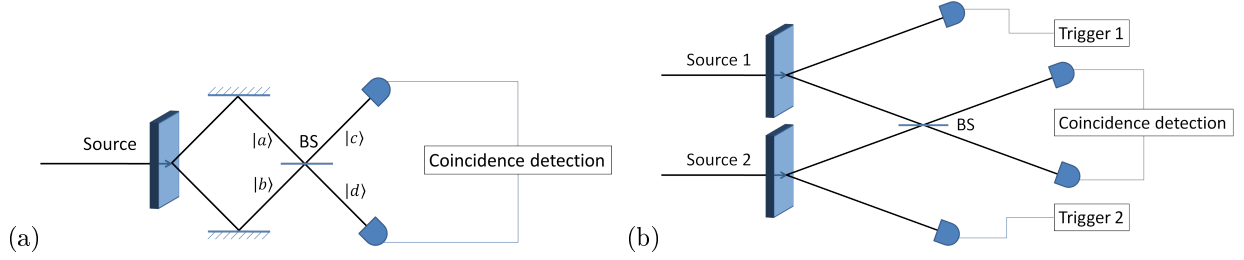


Figure 1.2: Diagram of Hong-Ou-Mandel interferometer for (a) one source and (b) two independent sources.

characteristic symmetry due to the downconverted photons having identical polarization.⁷ Another option is *type-II* phase-matching, which conserves momentum by converting from a fast pump photon to one slow and one fast photon ($e \rightarrow o + e$ or $o \rightarrow o + e$ depending on the crystal).

In a birefringent crystal, the sum of the magnitudes of the momenta of the daughter photons will be either greater than or equal to that of the pump. If it is equal, the downconversion process is *collinear*: the pump, signal, and idler all share the same spatial mode. If it is greater, momentum conservation mandates that the daughter photons are emitted at some angle relative to the pump, forming the characteristic cone (or cones in the type-II case) of *non-collinear* SPDC.⁸ Similar to the pump envelope for energy conservation, the exact conditions for momentum conservation in the longitudinal direction depend on the crystal length, and in the transverse direction on the pump focusing. Taken together, these constraints constitute the phase-matching function. Engineering a factorable source—which is motivated in the next subsection—depends critically on the phase-matching function, which is analyzed in detail in Sec. 2.2.

1.1.2 Motivation: Indistinguishability

To understand what a factorable source is and why it is important, let's consider the nature of indistinguishability. A key notion of quantum mechanics is that all elementary particles of a given type are perfectly identical. If two particles are also identical in all measurable degrees of freedom, they can be said to be indistinguishable: there is absolutely no way to label the particles and be able to determine at some later time which one is which.

The Hong-Ou-Mandel (HOM) effect provides an excellent illustration of this property as applied to photons [18]. In the HOM interferometer, two photons are combined on a 50-50 beam splitter, as shown in Figure 1.2(a). Two detectors look at the two output ports of the beam splitter, and register coincidence

⁷In this work, we use type-I phase-matching in BBO, which is a negative uniaxial crystal: it has a lower index of refraction for extraordinary polarization (parallel to the optic axis) than for ordinary polarization (perpendicular to the optic axis). This allows type-I phase-matching for SPDC with an extraordinary-polarized pump downconverting to two ordinary-polarized daughter photons ($e \rightarrow o + o$). A positive uniaxial crystal would satisfy type-I phase-matching with $o \rightarrow e + e$.

⁸The emission angle of this cone can be chosen by specifying the crystal cut angle with respect to the optic axis. For reasons we'll see in Sec. 2.2, it can be useful to choose this angle such that the pump and daughter photons are group-velocity matched, i.e., such that the signal and idler photons have the same group velocity in the crystal as the pump.

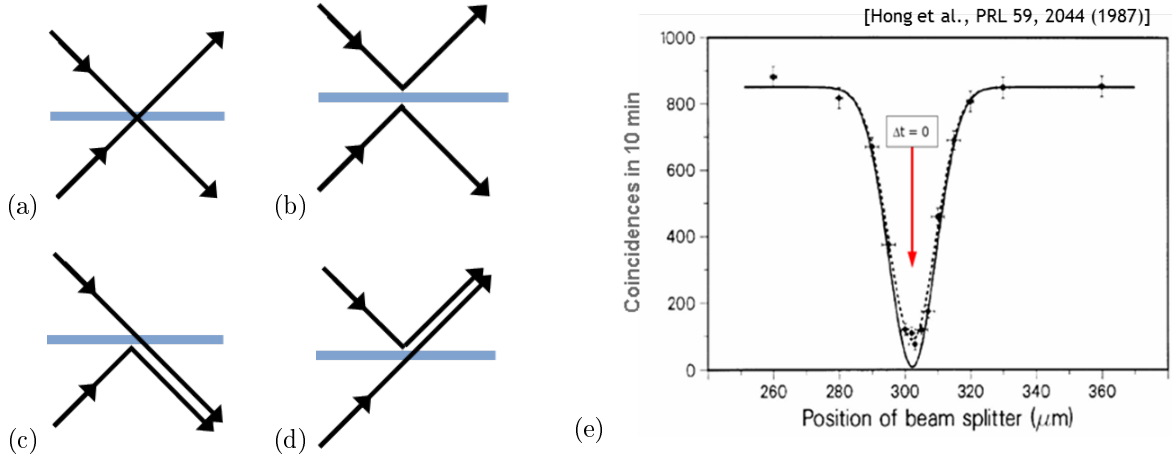


Figure 1.3: (a-d) Possible paths for reflection or transmission on beamsplitter. Terms (a) and (b) have opposite signs, so if the input photons are indistinguishable, these terms cancel when adding probability amplitudes. This leads to photons exiting together on one side of the beamsplitter or the other, and (e) the characteristic HOM dip in coincidence counts (from [18]).

counts if they both simultaneously detect a photon. The photons can exit the beam splitter through the same port, but a coincidence event will only be registered if the photons exit through different ports. There are two ways this outcome can occur, as shown in Fig. 1.3(a-b): either the photons are both transmitted through the beam splitter,

$$\begin{aligned} |a\rangle &\rightarrow |d\rangle \\ |b\rangle &\rightarrow |c\rangle, \end{aligned} \tag{1.3}$$

or they are both reflected,

$$\begin{aligned} |a\rangle &\rightarrow i|c\rangle \\ |b\rangle &\rightarrow i|d\rangle, \end{aligned} \tag{1.4}$$

where reflection has a phase shift of $\pi/2$ relative to transmission.⁹ Taken together, the beamsplitter will transform either input into an equal superposition of reflected and transmitted,

$$\begin{aligned} |a\rangle &\rightarrow \frac{|d\rangle + i|c\rangle}{\sqrt{2}} \\ |b\rangle &\rightarrow \frac{|c\rangle + i|d\rangle}{\sqrt{2}}. \end{aligned} \tag{1.5}$$

If the photons are distinguishable, this process occurs independently for both photons, and the probability of exiting in different ports is 50%. However, if the photons are indistinguishable, the processes must be

⁹This is a consequence of requiring the beamsplitter to be a unitary operator. That is to say, for a beamsplitter acting on some input state, $\psi_{out} = \hat{B}\psi_{in}$, we require the beamsplitter operator \hat{B} to satisfy $\hat{B}^*\hat{B} = I$.

summed at the amplitude level. Thus, for the two-photon input state

$$|a\rangle|b\rangle \rightarrow \frac{1}{2}(|d\rangle + i|c\rangle)(|c\rangle + i|d\rangle) = \frac{|2\rangle_c + |2\rangle_d}{\sqrt{2}}, \quad (1.6)$$

the cross-terms cancel, leaving zero probability of photons leaving different ports of the beam splitter, and no coincidence counts. This “bunching” of the photons into the same output mode is a consequence of the fact that photons are bosons. It should be noted that this is not an all-or-nothing effect: because of the nature of quantum states, it is possible for two photons to be partially indistinguishable. In the original experimental demonstration of the HOM effect, Hong et al. exploited this to measure the relative arrival time Δt of two photons on a beam splitter. For large Δt , the photons are distinguishable, and the rate of coincidence counts is high. However, as Δt becomes smaller than the coherence time, the coincidence counts decrease, approaching zero as Δt —and thus the distinguishability of the photons—approaches zero, in a characteristic “HOM dip”. The visibility of this dip, defined in terms of the measured maximum and minimum rates of coincidence counts C as

$$V \equiv \frac{C_{max} - C_{min}}{C_{max} + C_{min}}, \quad (1.7)$$

provides an excellent measure of the degree of indistinguishability of two photons.

The above discussion is most straightforward when applied to two photons generated from a single SPDC source. However, with some care, it can be generalized to two independent sources, as shown in Figure 1.2(b). Here, there are two SPDC sources which produce two photons incident on the beam splitter when both trigger detectors register a photon. This generalized version has all of the properties of the single-source HOM experiment, with the additional complication that for the photons on the beam splitter to be indistinguishable, there must be no way to tell which source the photon came from. Spectral or spatial correlations between the signal and idler photons from a given source will run afoul of this requirement: the photon hitting the trigger detector will then carry information about its partner at the beam splitter. This can be quantified in the density matrix picture. If we write the density matrix for the joint signal-idler system as ρ^{SI} , then heralded single photons produced by detecting an idler photon will be in the state $\rho^S = \text{tr}_I [\rho^{SI}]$. If the signal and idler photons are entangled, then this operation shows the resulting heralded single photons to be in a mixed state¹⁰. Only photons in identical pure states can interfere, so heralding a mixed state will inhibit the HOM effect. The visibility V of the HOM dip is in fact identical to the purity

¹⁰If the photons are maximally entangled, the heralded state is completely mixed. The purity is then related to the dimensionality d of the state, $P = 1/d$, as the state is a statistical mixture of d pure states. Intuitively, the visibility of a HOM dip is then equal to the chance of finding the same pure state on both inputs of the beamsplitter, also $1/d$.

$P \equiv \text{tr} [\rho^2]$ of heralded single photons, so measuring V provides a measurement of the factorability of the SPDC source.

1.1.3 Motivation: Unentanglement for Entanglement’s Sake

The previous subsection motivates the need for factorability in the two-photon state in the context of a two-source HOM experiment. However, quantum information processing schemes often demand instead that we produce entangled photon pairs, which are explicitly *not* factorable. Since entanglement is such an important resource for quantum information, one could be forgiven for wondering why we would want to engineer *unentanglement* in an entangled source. Surely if some entanglement is beneficial, then more is better still!

Lossy Channels

Unfortunately, this is not true in general, which we will illustrate by way of a detour through an important enabling technology for long-distance quantum communication: the quantum repeater [19–21]. Fiber-optic cables are the best known transmission method for both classical and quantum communication, but unavoidable losses in glass lead to the degradation of a signal when transmitting light over large distances. Typical fiber-optic losses in the telecom band are approximately 0.2 dB/km, leading to a signal loss of 99% in just 100 km (62 mi). In classical communication, this loss is overcome with the use of fiber-optic repeaters, which act as amplifiers by detecting an attenuated signal and then re-transmitting it at full power. However, this is impossible to do in a quantum channel, as measuring a quantum state destroys the state and “collapses” it onto a single basis. Classically, it is also possible to use optical amplifiers (e.g., based on nonlinear optical fiber), but this technique cannot be used in a quantum channel without distorting the initial state. This can be most easily seen by observing that such a quantum amplifier would violate the no-cloning theorem [22].¹¹

Suppose two researchers, Alice and Bob, wish to be able to send quantum states to each other (we’ll assume these states are single qubits in the polarization basis, i.e., the superposition state $|\psi\rangle = \alpha|H\rangle + \beta|V\rangle$, but this can be generalized). Without the possibility of amplifying a quantum signal, operating a quantum channel over long distances becomes prohibitively difficult.¹² Suppose we try to send 10,000 photons per second over a 200-km cable: on average we would expect only one of them to reach the other end.

¹¹If quantum states could be cloned, superluminal communication would also be possible. One can use entanglement to instantly prepare a distant particle in a desired state by a measurement of its entangled partner. If quantum cloning were possible, that distant qubit could be duplicated an arbitrary number of times so that its state could be perfectly reconstructed, allowing instantaneous transmission of information.

¹²This can be especially problematic for cryptographic protocols, where losses typically must be assumed to be due to an eavesdropper.

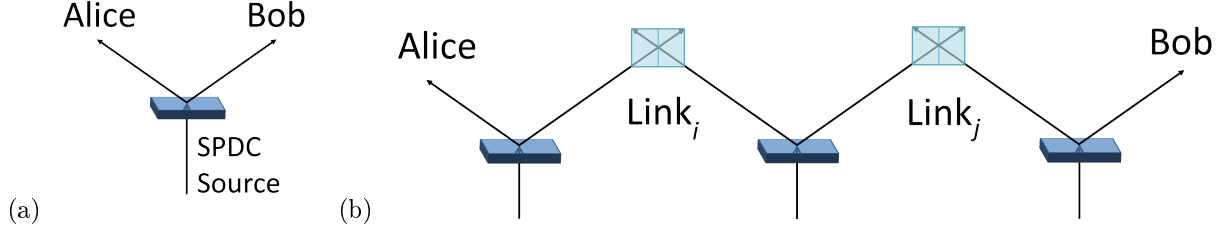


Figure 1.4: (a) Alice and Bob use an EPR pair (see Eq. 1.9) to form a quantum communication channel. (b) Alice and Bob use a series of quantum repeaters for an enhanced quantum channel.

Quantum Repeaters

Another way to operate this channel is by using quantum teleportation, which allows Alice to send Bob an arbitrary, unknown quantum state, assuming Alice and Bob share an EPR pair and have the ability to communicate over a classical channel [3, 4]. The second assumption is easily met by the global telecommunications network, while the first can be achieved using a polarization-entangled SPDC source. However, sending the photons in the entangled pair to Alice and Bob uses the same lossy optical channel, so this doesn't offer any improvement. Now instead imagine that we split that distance into four “segments”, each 50 km long, where each segment has an SPDC source in the middle (see Fig. 1.4). Assume for the moment that at the interfaces between each segment, there are “links” that have the property that if each segment successfully transmits an entangled pair, Alice and Bob will share an entangled pair. Now every 100 μ s, we fire each SPDC source, producing a pair of photons. In each segment, there is a 10% chance of successful transmission, so we would expect the overall transmission probability to be $0.1 * 0.1 * 0.1 * 0.1 = 0.0001$, or exactly what it was without using quantum repeaters.

The real advantage comes only when we can treat the segments independently. If we wait 2 ms, each source will produce 20 photon pairs, with an 88% chance that at least one of those photon pairs is successfully transmitted. At each link, we combine only one successfully transmitted pair from the 20 attempts,¹³ so the overall success probability for the attempt is $0.88 * 0.88 * 0.88 * 0.88 \approx 60\%$. We do this 500 times per second, so on average it will succeed about 300 times per second, compared to only once without using repeaters. This can be improved even further by increasing the number of repeaters, with the number of photons successfully transmitted per second given by

$$\frac{10000}{N} \left(1 - \left(1 - 0.0001^{\frac{1}{k}} \right)^N \right)^k, \quad (1.8)$$

where N is the number of photons collected per attempt and k is the number of quantum repeaters used

¹³This is intended to give an intuitive picture of the quantum repeater. Actual proposals instead use a more sophisticated entanglement distillation scheme to increase the probability of successful entanglement, but the general effect is the same.

(20 and 4 respectively in this example). Because of the exponential loss in the optical channel, this scales impressively with distance, offering a relative improvement of over 10^{100} for a hypothetical intercontinental New York-to-London quantum channel. In general, the success probability scales linearly with distance (compared to exponentially without repeaters), with the number of repeaters required scaling only logarithmically [19]. But for this to work, we need our sources of polarization entangled photons to also be unentangled in every other basis, as we will see shortly.

Teleportation, Entanglement Swapping, and Bell State Measurement

Quantum repeaters are great news for long-distance quantum communication, but they have one difficulty that turns up constantly in large-scale quantum information processing schemes: how to link together multiple independent sources? This is an extension of quantum teleportation, where Alice and Bob share a pair of qubits in a maximally entangled (EPR) state, such as one of the Bell states,

$$|\Phi^+\rangle = \frac{1}{\sqrt{2}} (|0_A 0_B\rangle + |1_A 1_B\rangle), \quad (1.9)$$

where the subscripts A and B denote Alice's and Bob's qubit, respectively. Additionally, Alice has a qubit in some unknown state

$$|\psi\rangle = \alpha |0\rangle + \beta |1\rangle, \quad (1.10)$$

which she wishes to transfer to Bob. To do this, she performs a joint measurement on the unknown qubit and her entangled qubit in the Bell-state basis. She then classically communicates to Bob which Bell state she detected, which information Bob uses to prepare his qubit into the unknown state. For example, if Alice reports that she measured the Bell state

$$|\Psi^+\rangle = \frac{1}{\sqrt{2}} (|0_A 1_B\rangle + |1_A 0_B\rangle), \quad (1.11)$$

then Bob knows that his photon is in the state $|\psi\rangle = \beta |0\rangle + \alpha |1\rangle$, so he need only perform a unitary operation to swap the amplitudes of $|0\rangle$ and $|1\rangle$. If Alice reports one of the other three Bell states, Bob simply performs a different unitary operation to recover the initial state. Note that this does not violate the no-cloning theorem, as the original state is destroyed in the process. Further, Bob does not actually know the state of his photon, only that it is in the same state as the original unknown photon.

Actually performing this Bell-state measurement on photons is difficult (and in fact is impossible using just linear optics). But most importantly for the unentangled source, even partial Bell-state discrimination

requires observing HOM-style interference of two photons on a beamsplitter [23]. Since this interference fails if the two photons are not in identical pure states, it follows that any other source of correlations (besides polarization entanglement) in the photon pair must be eliminated.

Now we can extend this process of teleportation to an arbitrary number of links (see Fig. 1.4b). Instead of teleporting a qubit immediately to Bob, suppose Alice first shares an entangled pair with an intermediary Ingrid, who shares another pair with John, who shares a pair with Bob. Ingrid and John act as links using teleportation to pass along the entanglement with Alice’s particle from Ingrid to John and from John to Bob (so-called “entanglement swapping”) [24].¹⁴ Because no party needs to know the state of the photon being teleported, this can be done in the same way with an arbitrary number of quantum repeater links.

1.2 Introduction to Efficient Photon-Number Resolving Detectors

High-efficiency photon-number resolving detectors can be applied to many areas of optical quantum information processing, such as state preparation, quantum computing, and metrology. A high detection efficiency η is nearly always useful for increasing data collection rates, but is absolutely essential for some applications. In particular, tests of quantum nonlocality require detection efficiencies of $\eta > 66 - 83\%$ depending on the scheme [2]. Similarly, scalable linear optical quantum computing (LOQC) requires $\eta > 66\%$, with performance gains scaling with efficiency [8]. Additionally, because the probability of detecting N photons scales as η^N , low efficiency detectors quickly cause prohibitively slow data collection for large-scale multiphoton experiments. For example, in an experiment requiring the detection of 6 simultaneous photons, one would have to collect data for 130 times as long with a 40%-efficient detector compared to a 90%-efficient detector.

Tests of non-locality are especially interesting, particularly the so-called “loophole-free” test of Bell’s inequality. Bell’s inequality famously demonstrates that a hidden variable theory cannot reproduce the non-local features of quantum entanglement [25, 26]. Experiments have succeeded in violating Bell’s inequality to confirm that local hidden variable theories do not suffice [27], but they have not done so unambiguously. In particular, two possible loopholes continue to allow the possibility of valid local realistic theories of quantum mechanics. Roughly, the detection loophole states that although the observed outcomes may violate Bell’s inequality, the measured sample may not be a valid representation of the entire space. This loophole can be closed with photons by employing high efficiency detectors. Additionally, the timing loophole states that if the measurement events are not space-like separated, there could be an unexplained causal relationship between them without relying on quantum nonlocality. This loophole can be closed by spatially separating

¹⁴The protocol relies on being able to store the photons until all the entanglement swapping has succeeded, using a “quantum memory”, another practical difficulty not addressed here.

entangled photons by more than the duration of the measurement process, which would require fast detectors to avoid the losses associated with long-distance fiber optics. Performing such an experiment is predicated on having detectors which are simultaneously fast and incredibly efficient, a combination that has not yet been realized by available detectors.

Conventional technologies for detecting single photons include photomultiplier tubes and avalanche photodiodes. These devices are well established and commercially packaged for turn-key operation, but are limited to detection efficiencies of less than 70% [28]. In recent years, several alternative technologies have emerged, including superconducting transition edge sensors (TESs), superconducting nanowire single-photon detectors (SNSPDs), and visible light photon counters (VLPCs). TESs have managed to achieve efficiencies of up to 98% [29, 30]; unfortunately, the detectors suffer from relatively long response times, high jitters, and long dead-times [31]. On the other hand, SNSPDs have been able to achieve much faster speeds as well as 93% system efficiency, but still require cooling to below 2 K [32–34]. VLPC detectors have the desirable characteristics of extremely high efficiency (estimated $95\% \pm 5\%$ intrinsic quantum efficiency, 88% observed with coupling losses), high speed (approximately 250 ps jitter), and photon number-resolving capability [35–39]. This efficiency is among the highest of any single-photon detection system. Though they require cryogenic cooling, their 7 K operating temperature is much easier to achieve than the sub-2 K temperatures of SNSPD or TES detectors. Also, the ability to differentiate between different photon numbers is critical for some experiments, and beneficial for nearly all, as it can be difficult to guarantee the presence of only one photon per desired detection event, and additional photons can confound experimental results.¹⁵ In Chapters 5 and 6, we discuss the details of the VLPC detector, our system for operating it, and efficiency optimizations that have lead to a measured 91% system efficiency.

¹⁵For example, SPDC produces photon pairs probabilistically with each pump pulse. Often it necessary to deal with only a single photon pair at a time, or at least to exclude the multipair events by detecting them. If detectors cannot resolve more than one photon at a time, however, the only option is to operate at very low count rates such that the chance of generating multiple photons pairs at a time is extremely small.

Chapter 2

Engineering Unentanglement

SPDC: Super Photon Duos in a Cone

Lab whiteboard, attributed to Aditya Sharma

In this and the following chapters, we are primarily concerned with the joint spectrum of the two-photon state produced by downconversion. The joint spectral intensity describes a probability distribution in the frequency space of the two-photon state. We are particularly concerned with whether this joint spectrum is *separable* or *correlated*. That is to say, whether it describes a two-photon state that can be written as a separable product state of two single-photon states, or an entangled state that cannot.

Having motivated the need for sources of unentangled photons in Section 1.1, let's examine how we can achieve this goal. We will consider the joint spectrum arising from downconversion, how spectral filtering eliminates those correlations at the cost of a reduced count rate, and how to eliminate correlations without spectral filtering.

2.1 A Simple Model

Before jumping in to the full theory of the engineered source in Section 2.2, let's consider first a simplified version of the joint spectrum of downconversion photon pairs. This model will motivate the more complete theory, as well as provide an intuition for how to think about the joint spectrum. The joint spectrum and its Schmidt decomposition¹ are absolutely critical to understanding a downconversion source, but can be difficult to understand intuitively; often the theoretical background is either completely hand-waved over, or else done in a mathematical rigor that obscures intuition. This section aims to strike a balance between the two.

Suppose the only constraint in the downconversion process is conservation of energy between the pump and signal and idler photons, i.e., $\omega_s + \omega_i = \omega_p$. If the pump energy is described by a Gaussian distribution

¹See Sec. 2.1.1.

$f(\omega_p)$ characterized by average frequency $2\omega_0$ and standard deviation σ , we can write

$$f(w_p) = A \exp \left[-\frac{(\omega_p - 2\omega_0)^2}{2\sigma^2} \right], \quad (2.1)$$

where A is a normalization constant to preserve unit area. To simplify the analysis, we can redefine the pump spectrum in terms of $\nu_p \equiv \omega_p - 2\omega_0$, such that it has a mean of zero. This applies to the signal and idler frequencies as well, where for degenerate SPDC we have $\nu_s = \omega_s - \omega_0$ and $\nu_i = \omega_i - \omega_0$. We also neglect the fact that this joint spectrum contains negative frequencies, which are physically impossible. Substituting this definition for the signal and idler frequencies into Eq. 2.1, we can write the joint spectrum as

$$f(\nu_s, \nu_i) = A \exp \left[-\frac{\nu_s^2 + \nu_i^2}{2\sigma^2} - \frac{2\nu_s \nu_i}{2\sigma^2} \right], \quad (2.2)$$

as plotted in Fig. 2.1(a).

2.1.1 Schmidt Modes

Before continuing with the joint spectrum, we will touch briefly on the Schmidt decomposition² [10, 40], which allows a pure state of a composite system AB to be decomposed into a sum over products of orthonormal states of A and B as follows,

$$f_{A,B} = \sum_i \sqrt{\lambda_i} g_{A,i} g_{B,i}, \quad (2.3)$$

where the Schmidt coefficients $\sqrt{\lambda_i}$ satisfy the normalization condition $\sum_i \lambda_i = 1$. In a highly multi-dimensional space, this answers the difficult question of exactly which mode(s) to collect to maximize the probability of detection (the answer being the one(s) with the largest coefficients λ_i). The Schmidt coefficients can be used to define an exceptionally useful quantity known as the Schmidt number³ K , which can be described as the effective number of populated eigenmodes:

$$K = \frac{1}{\sum_i \lambda_i^2}. \quad (2.4)$$

Why is this so useful? First, it is a natural measurement of the amount of entanglement in a system that also conveniently relates to the entropy in the system in terms of $\sum \lambda \log_2 \lambda$ [41]. Also, the inverse Schmidt number $1/K$ of the *collected* spectrum is equal to two other relevant quantities in an SPDC source: the purity

²A practical note for calculating Schmidt decompositions: this process is functionally equivalent to singular value decomposition, which is easily performed by any capable linear algebra package.

³Confusingly, the Schmidt number is also sometimes defined as the total number of eigenmodes without weighting by eigenvalues, and K is sometimes referred to as the “cooperativity parameter.”

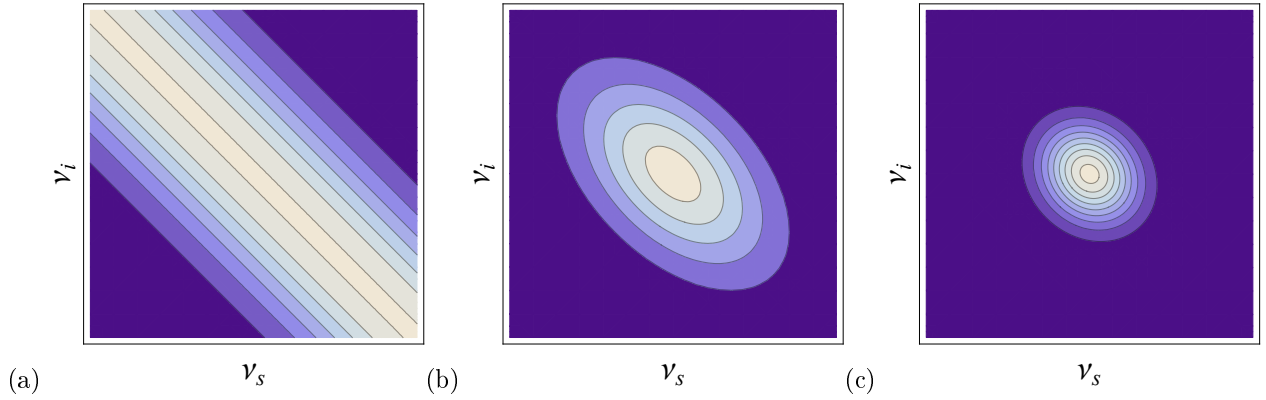


Figure 2.1: Modeled JSI with (a) no filtering (Eq. 2.2), (b) filter width equal to the pump bandwidth (Eq. 2.5), and (c) filter width equal to $\frac{1}{5}$ of the pump bandwidth.

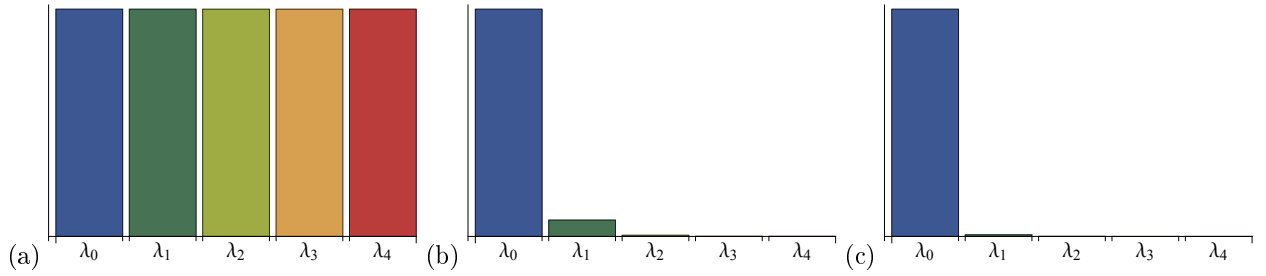


Figure 2.2: Relative values of Schmidt decomposition eigenvalues for the (unfiltered/filtered/highly-filtered) joint spectra of Fig. 2.1. The resulting Schmidt numbers (defined by Eq. 2.4) for the three cases are (a) $K = \infty$, (b) $K = 1.15$, and (c) $K = 1.001$.

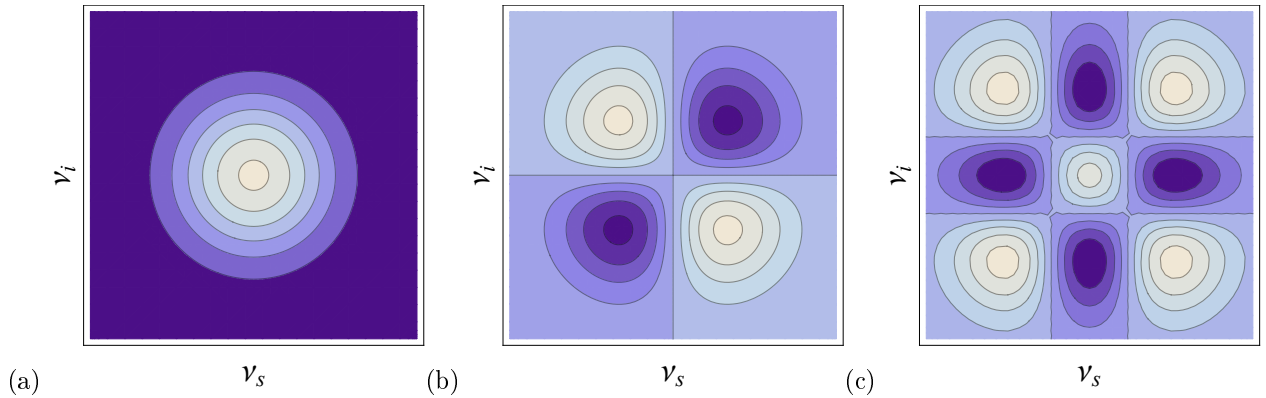


Figure 2.3: (a-c) The first three Schmidt modes for a two-dimensional diagonal Gaussian ellipse. Lightly colored areas are maxima, darkly colored areas are minima.

P of a heralded single-photon and the visibility V of a two-source HOM interferometer [42]. Note that if $f_{A,B}$ is separable, this sum is trivial, as by definition we can simply write $f_{A,B} = g_A g_B$, and $K = 1$. Similarly, for a maximally (polarization-)entangled two-photon state $f_{A,B} = (H_A H_B + V_A V_B) / \sqrt{2}$, the number of modes is $K = 1/(\frac{1}{4} + \frac{1}{4}) = 2$. However, in the case of Eq. 2.2 the continuous basis and symmetry of the problem indicate that the Schmidt number becomes a sum of $N \rightarrow \infty$ equally weighted terms, $\lambda_i = \frac{1}{N}$. Thus, the Schmidt number is $K = 1/(\sum_{i=1}^N 1/N^2)$, but the denominator goes to zero as $N \rightarrow \infty$, indicating that an infinite number of modes are required to describe this distribution.

Now suppose that we apply a Gaussian spectral filter (with standard deviation σ_f) to the signal and idler modes. After filtering, the joint spectrum from Eq. 2.2 becomes

$$f(\nu_s, \nu_i) = A \exp \left[-\frac{\nu_s^2 + \nu_i^2}{2\sigma^2} - \frac{2\nu_s \nu_i}{2\sigma^2} \right] \exp \left[-\frac{\nu_s^2}{2\sigma_f^2} \right] \exp \left[-\frac{\nu_i^2}{2\sigma_f^2} \right], \quad (2.5)$$

which is plotted in Figure 2.1(b-c) for different filter bandwidths. Note that if σ_f is large, we recover the unfiltered case of Eq. 2.2, while if σ_f is small, the filter terms dominates and the joint spectrum becomes separable. In this general case, it can be shown [13] that the inverse Schmidt number $1/K$ is given by

$$\frac{1}{K} = \sqrt{1 - \frac{1}{\left(1 + \left(\frac{\sigma}{\sigma_f}\right)^2\right)^2}}, \quad (2.6)$$

which has the expected behavior that $K \rightarrow \infty$ as $\sigma_f \rightarrow \infty$ (the unfiltered case), and $K \rightarrow 1$ as $\sigma_f \rightarrow 0$ (the tightly filtered case).

2.1.2 The Spectrally Filtered Source

As discussed in the previous chapter, an ideal photon pair source for scalable optical quantum information processing should not have correlations between signal and idler photons. The calculations we have just carried out demonstrate how these correlations occur, and also how to eliminate them: all we have to do is use narrow spectral filters. But this solution has a significant downside: if the photons are highly correlated, the filters will block the majority of the photon pairs. This can be easily seen from a plot of the joint spectrum in Fig. 2.1(a): an uncorrelated subset of the joint spectrum will contain only a small fraction of the total coincidence counts (in the theoretical case of a perfectly correlated joint spectrum, the fraction is actually zero). Another way to see this is through the Schmidt decomposition: the best filtered, uncorrelated collection mode one can hope for is the most populated Schmidt mode. If the Schmidt number is large, there are many significantly populated Schmidt modes, and any one of them will contain only a small fraction of

the total intensity.

Instead of employing spectral filtering to “fix” a highly-correlated source, it would be desirable⁴ to produce a joint spectrum which is already intrinsically uncorrelated. The following section describes how this can be achieved by manipulating the SPDC phase-matching conditions, using one of the family of “engineered source” techniques [12, 13, 43]. The equations presented here are based on the work of our collaborators Alfred U’Ren and Luis Vicent, and the full derivation is given in [42].

2.2 A Sophisticated Model

The simplified model of the previous section only accounts for conservation of energy between the pump envelope and the signal and idler photons, instead of using the full SPDC phase-matching function. We also consider only the joint spectral *intensity*, whereas correlation can also be present in the phase, which is critical for the case of a chirped pump. Finally, we entirely neglected spatial correlations, another important source of non-separability. In practice, spatial correlations are generally eliminated by collecting into single-mode fiber. However, this has the same effect as spectral filtering in reducing source brightness, so ideally we wish to reduce spatial correlations before collection and carefully choose a collection mode which is highly populated. Moreover, there can be cross-correlations between spatial and spectral modes that need to be properly accounted for.

To engineer a source of factorable photons, one must calculate the dependence of frequency and spatial correlations on the physical parameters of the SPDC scheme. The state produced by SPDC can be expressed in terms of creation operators, the signal and idler wavevectors \vec{k}_s and \vec{k}_i , and a constant η as

$$|\psi\rangle = |\text{vac}\rangle + \eta \int d\vec{k}_s \int d\vec{k}_i F(\vec{k}_s, \vec{k}_i) \hat{a}_s^\dagger(\vec{k}_s) \hat{a}_i^\dagger(\vec{k}_i) |\text{vac}\rangle. \quad (2.7)$$

Here, F is the joint two-photon amplitude (JTPA), which can be written as

$$F(\vec{k}_s, \vec{k}_i) = \ell(\vec{k}_s) \ell(\vec{k}_i) \alpha(\omega_s + \omega_i) \phi(\vec{k}_s, \vec{k}_i), \quad (2.8)$$

where $\ell(\vec{k}_s)$ and $\ell(\vec{k}_i)$ are separable terms, α is the pump spectral amplitude (assumed to be Gaussian), and ϕ is the phase-matching function. Ideally, all the terms in the JTPA would be separable, so we could write $F(\vec{k}_s, \vec{k}_i) = S(\vec{k}_s)I(\vec{k}_i)$ for some functions S and I which depend only on the signal and idler photons,

⁴It is worth noting that a filtered correlated source can actually be more desirable in some cases. For example, it is possible take advantage of correlations to improve heralding efficiency (the chance of detecting an idler photon in a given mode coincident on the detection of a signal photon). However, this is achieved at the expense of reduced source brightness.

respectively. If this were the case, there would be no correlations between the signal and idler photons, the source would be factorable, and each photon would individually be in a pure state. Unfortunately, α and ϕ are *not* in general separable. However, by adjusting the appropriate parameters of the system, these terms can be made approximately separable. To see how, first consider the full form of the phase-matching function [42],

$$\phi(\vec{k}_s, \vec{k}_i) = \exp\left(i \frac{|\underline{k}_\perp|^2}{2k_p} z_0\right) \exp\left[i \frac{L}{2} (\Delta k + k_{\perp y} \tan \rho_0)\right] \exp\left(-\frac{1}{4} w_0^2 |\underline{k}_\perp|^2\right) \text{sinc}\left(\frac{L \Delta k}{2}\right), \quad (2.9)$$

where L is the length of the downconversion crystal, k_p is the pump wavenumber, w_0 is the pump beam waist, z_0 is the distance from the pump beam waist to the center of the downconversion crystal, ρ_0 is the spatial walkoff angle, Δk is the longitudinal phase mismatch, and \underline{k}_\perp is the transverse phase mismatch, represented as a two-dimensional vector.

Transforming this into spherical coordinates $\{\omega_s, \theta_s, \phi_s, \omega_i, \theta_i, \phi_i\}$ and Taylor-expanding to first order provides of a set of constraints to satisfy in order for non-separable cross terms to vanish, and thus for the source to be factorable. These constraints are detailed in Table 2.1, but roughly they are: (1) choosing the collection angles θ_s and θ_i so the longitudinal component of the signal and idler group velocities match the pump group velocity, (2) selecting the pump beam waist and crystal length according to the collection angles, (3) using a pump bandwidth⁵ larger than a threshold value which is inversely proportional to crystal length, and (4) collecting photons in a small angular spread around θ_s and θ_i [42]. The conservation constraints of the pump envelope and phase-matching function are shown graphically in Fig. 2.4, demonstrating how a nearly separable joint spectrum can be obtained by appropriate selection of source parameters.

2.2.1 The Engineered Source

We have applied these conditions to type-I degenerate SPDC in β -barium borate (BBO), pumped with a pulsed 405-nm source, which is produced by frequency doubling an ultrashort (35 fs) pulsed (76 MHz) 810-nm Tsunami Ti-Saph laser. The wavelength is chosen based on the availability of ultrafast sources and efficient detectors, compared to telecom wavelengths where detector efficiencies are much lower ($\sim 30\%$ and $\sim 60\%$ for commercial APD quantum efficiencies for 1550 nm and 810 nm respectively). The optimal external collection angle is found to be the angle that matches the group velocity of the pump and daughter photons ($\theta_{s0} = -\theta_{i0} = 16^\circ$ in our source), as shown in Fig. 2.6. The additional constraints of Table 2.1 are

⁵ In practice, the extremely short pulses and consequently large bandwidths required for this scheme lead to substantial practical difficulties with dispersion. In general, the index of refraction of an optical material is not fixed, but rather varies with wavelength (this same effect we exploit to our benefit in Section 3.3). The effect is particularly devastating for the engineered source, as this serves as an additional source of spectral correlations. Further details about the impact of dispersion on ultrafast laser systems and methods for measuring and mitigating it are discussed in detail in Appendix A.

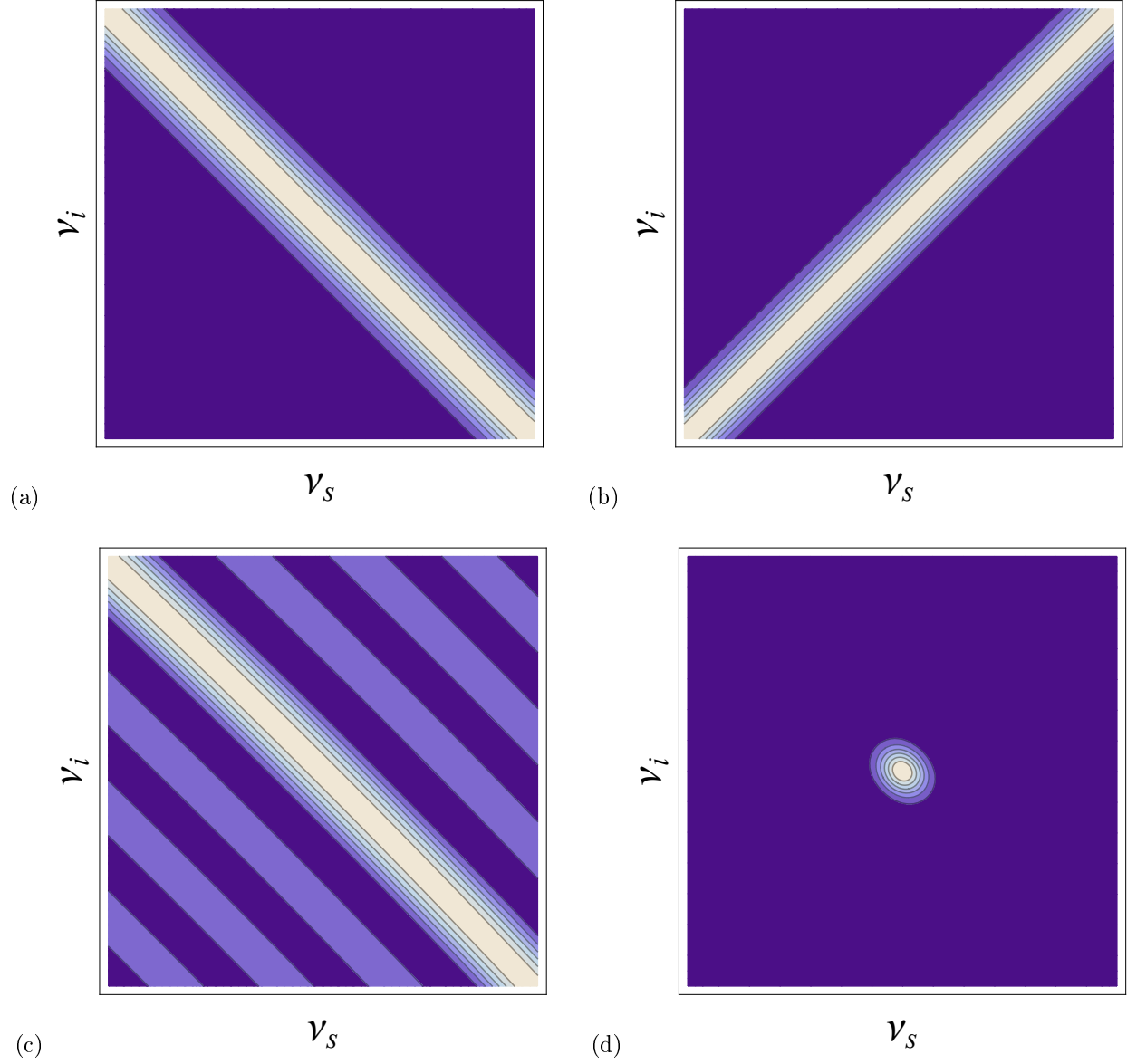


Figure 2.4: Joint spectral intensity correlations arising from the various components of the phase-matching function, including (a) energy envelope, (b) transverse momentum, (c) longitudinal momentum, and (d) the overall JSI formed by the product of these. This demonstrates how energy and momentum conservation constraints can compensate each other to produce an approximately factorable joint spectrum without spectral filtering. Also note the exponential suppression of the longitudinal phase-matching sinc lobes.

$$\begin{aligned}
(1) \quad & \begin{cases} k'_s = k'_p \cos \theta_s \\ k'_i = k'_p \cos \theta_i \end{cases} \\
(2) \quad & \frac{w_o^2}{0.193L^2} = -\tan \theta_s \tan \theta_i \\
(3) \quad & \sigma \gg \frac{2}{0.193L(k'_p - k'_s \cos \theta_s)} \\
(4) \quad & \Phi_{mas}^2 (w_0^2 + 0.193\rho_0 L^2) \lesssim \frac{1}{4k^2}
\end{aligned}$$

Table 2.1: Conditions for SPDC separability [15, 42] where k' is the group velocity ($\frac{dk}{d\omega}$), w_o and σ are the pump beam waist and bandwidth respectively, L is the crystal length, θ_s and θ_i are the signal and idler emission angles inside the crystal, Φ_{mas} is the maximum angular spread about the signal and idler emission angles, and ρ_0 is the walkoff angle.

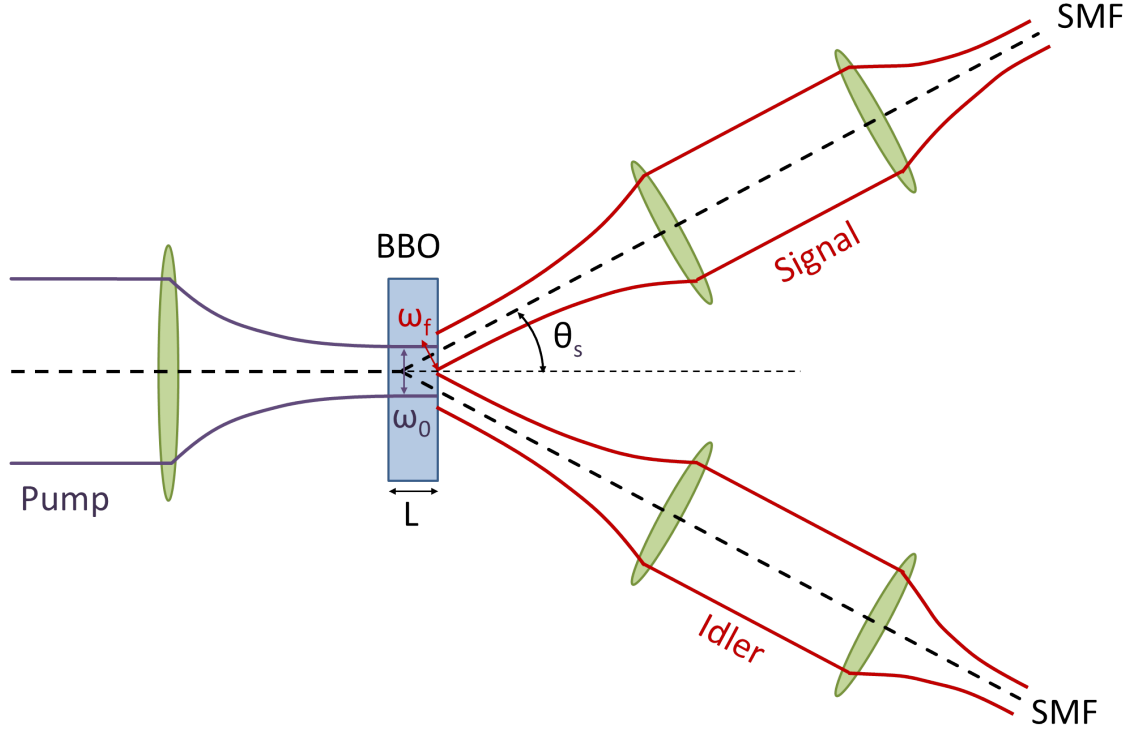


Figure 2.5: Diagram of source geometry, relevant parameters, and their values in our implementation of the engineered source. The collimated pump is focused to a waist of ω_0 ($60 \mu\text{m}$). Focused collection of the signal and idler modes with an external collection angle of θ (16°) and a beam waist of ω_f ($55 \mu\text{m}$) at the SPDC crystal of length L (0.3 mm) of BBO. The signal and idler modes are collimated before passing through additional measurement-dependent optics (not shown), and finally are collected into single-mode fiber. For simplicity, other diagrams in this work show just the average k-vector for the pump and collection modes, leaving out the focusing and collection optics. However, these focusing and collection optics are still present in all configurations of this source.

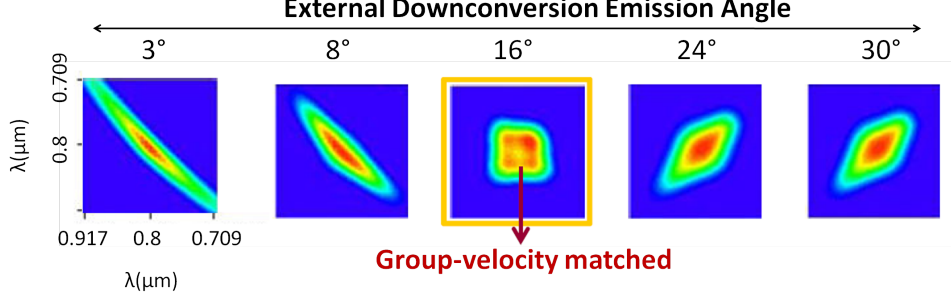


Figure 2.6: Predicted dependence of joint spectrum on downconversion emission angle. The optimally separable case occurs when the pump group velocity matches the signal and idler group velocities [44].

satisfied by choosing a crystal length of $L = 300 \mu\text{m}$ and a pump beam waist of $w_0 = 23.15 \mu\text{m}$ [15]. These source parameters are diagrammed in Fig. 2.5. For experimental practicality, rather than the theoretically optimal waist of $23.15 \mu\text{m}$, we use a quasi-optimal pump beam waist of $w_0 = 60 \mu\text{m}$. Due to astigmatism and ellipticity in the pump, the larger beam waist is more symmetric and thus leads to a higher purity than attempting a tighter focus where these effects are more pronounced. Using a 100-mW pump beam, we observe a *detected* pair collection rate into single-mode fiber of 10,000 pairs per second.

2.3 Polarization Entanglement

2.3.1 Two-crystal Scheme

An advantage of this engineered source is the relative ease of employing it as a source of polarization-entangled photons using a standard two-crystal geometry [45], as shown in Fig. 2.7. This method uses two identical but orthogonally oriented type-I SPDC crystals, such that the first converts horizontally (H) polarized pump photons to pairs of vertically (V) polarized photons, while the second takes V pump photons to H pairs. Thus, by pumping with the state

$$|\psi_p\rangle = \cos \theta |H\rangle + e^{i\phi} \sin \theta |V\rangle, \quad (2.10)$$

we can produce the two-photon state

$$|\psi_{spdc}\rangle = \cos \theta |VV\rangle + e^{i\phi'} \sin \theta |HH\rangle, \quad (2.11)$$

where the relative phase ϕ' is determined by the relative pump phase ϕ and the crystal parameters. By choosing a diagonally polarized pump ($\theta = 45^\circ$), we obtain a maximally entangled polarization state.

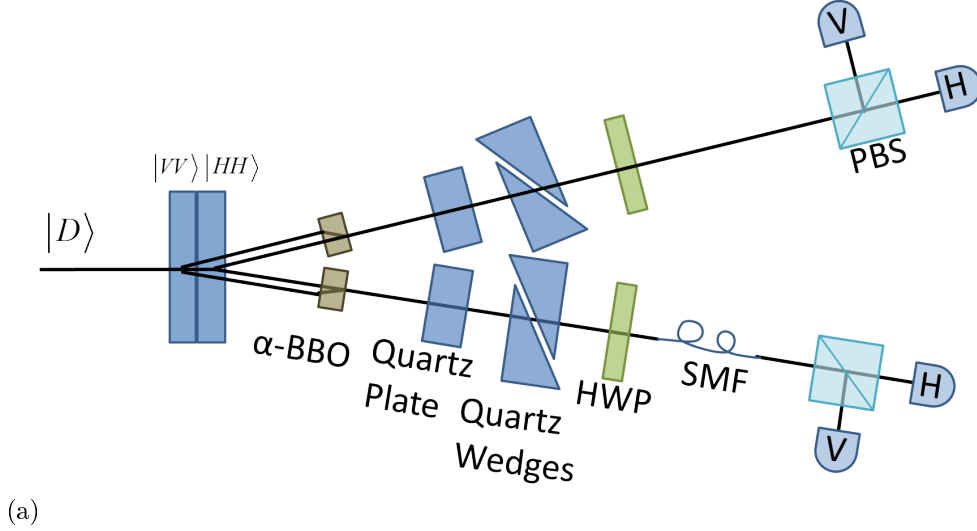


Figure 2.7: Diagram of the two-crystal scheme for polarization entanglement. We use a diagonally polarized pump and two orthogonally oriented type-I SPDC crystals to produce pairs of polarization-entangled photons. The crystal labels indicate the polarization of the SPDC cone produced by each crystal. Due to the spatial separation of the two crystals, we use walk-off in birefringent α -BBO to combine the photons into a single spatial mode. The quartz plate and quartz wedges compensate for the temporal delay between the photons.

Note that order of the SPDC crystals in the two-crystal scheme is important. Due to birefringent effects in the crystals and the 16° collection angle, there is an asymmetry between the signal and idler modes. Specifically, because the collection modes lie in the same horizontal plane, the polarization angle with respect to the SPDC crystal is identical for vertically polarized pairs, but not for horizontally polarized pairs. Because the crystals are birefringent, the horizontally polarized single and idler modes will experience an asymmetric walk-off.⁶ So, to preserve symmetry, the $H \rightarrow VV$ crystal should be in front of the $V \rightarrow HH$ crystal, as is the case in Fig. 2.7.

2.3.2 Which-Crystal Distinguishability

We can take advantage of birefringent walk-off to solve another problem with the source: the distinguishability of photons produced by the two crystals. To produce a polarization-entangled state, there must be no way to determine which crystal a particular photon was produced in. Otherwise, rather than the entangled state

$$|\psi\rangle = \frac{1}{\sqrt{2}} (|HH\rangle + |VV\rangle), \quad (2.12)$$

⁶Walk-off occurs because the propagation direction of extraordinary light in a birefringent material is not normal to the wavefront. See Chapter 8.4 of Hecht for an intuitive explanation of the properties of birefringent materials [46].

we will instead produce the mixed state

$$\rho = \frac{1}{2} (|HH\rangle\langle HH| + |VV\rangle\langle VV|). \quad (2.13)$$

The distinguishing information can be present spectrally, spatially, or temporally. Spectral distinguishability is taken care of almost by default, as the two crystals are identical up to a 90° rotation and the spectral distribution of SPDC rotationally symmetric about the pump.

Spatially, the SPDC crystals have a center-to-center offset of $300\text{ }\mu\text{m}$, which leads to a $(300\text{ }\mu\text{m}) \sin 16^\circ = 82.69\text{-}\mu\text{m}$ separation of the desired collection modes. This separation makes it impossible to efficiently collect from both crystals unless compensated for. Fortunately, the two crystals produce orthogonal polarizations, so a birefringent compensation crystal can be chosen such that extraordinarily polarized photons will experience precisely enough walk-off to be displaced onto the ordinarily polarized mode, thus “stitching” together the two modes. In our source, this compensation can be achieved with 0.952 mm of α -BBO, cut with optic axis at 45° to the front surface. In practice, we use 1 mm of α -BBO and adjust the angle of the crystal slightly with respect to the incident light to fine-tune the displacement.⁷

Temporal distinguishability arises from geometrical and birefringent collection time differences between H and V photons, and is especially important given the femtosecond-scale coherence lengths of our source. For temporal compensation, we use a quartz plate and a pair of quartz wedges in the style of a Soleil-Babinet compensator. Here again we rely on birefringence, but rather than walk-off, the critical property is just the optical path length difference (and thus time delay) between ordinary and extraordinary polarization. This time delay is controlled by varying the thickness of quartz, and can be set anywhere on a range of approximately $\pm 300\text{ fs}$ as needed to compensate time-of-arrival differences between the crystals.

2.3.3 Measuring Entanglement

There are many approaches to detecting and quantifying entanglement, including Bell inequality violation, quantum state tomography, and a variety of entanglement witnesses [25, 47]. In our case, we demonstrate that we have produced entanglement by observing correlation/anticorrelation in two mutually unbiased bases [48]. Briefly stated, a set of mutually unbiased bases (MUBs) is defined by the property that if a state is prepared in one basis in the set, the outcome of a measurement in any other basis in the set is uniformly randomly distributed over all possible outcomes. A polarization qubit has three mutually unbiased bases, typically defined as H/V (horizontal/vertical), D/A (diagonal/anti-diagonal), and L/R (left/right circular). Correlations in each of these bases can be determined by measuring the visibility of fringes in two-photon

⁷Tilting about the optic axis increases the displacement, tilting perpendicular to the optic axis decreases the displacement.

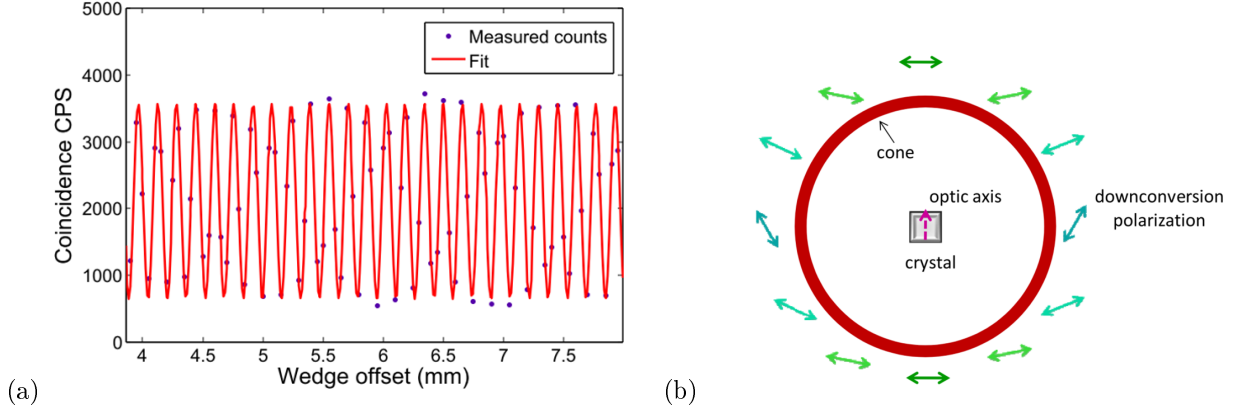


Figure 2.8: (a) Diagonal-diagonal coincidence counts as a function of phase offset between H and V, demonstrating polarization correlation / anticorrelation. (b) Sketch of the asymmetric photon-pair polarization caused by the Migdall effect, as a function of angle around the downconversion cone with respect to the optic axis (the optic axis shown is oriented vertically and slightly out of the page).

coincidences as a function of relative phase (see Fig. 2.8a). A maximally entangled two-qubit state can have perfect correlation (unit visibility) in each mutually unbiased basis, while a separable state can only have perfect correlation in one basis, or a total visibility of 1 summed over all MUBs [49]. We observe a visibility of 85% in the H/V basis and 75% in the D/A basis, which exceeds the classical threshold and clearly demonstrates entanglement, though not a maximally entangled state. The reduction in visibility indicates that there remains some which-crystal distinguishing information, and the quality of entanglement could be improved by more careful calibration and alignment. However, it is also limited by asymmetric polarization in type-I SPDC, described below.

2.3.4 Migdall Effect

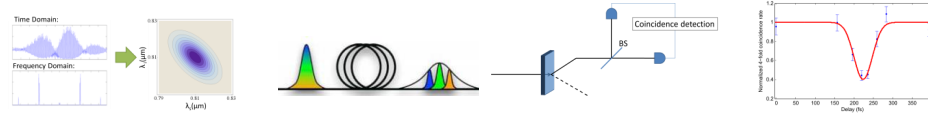
In a simple model of type-I phase-matched SPDC, we assume that the daughter photons are polarized exactly orthogonally to the pump photon. However, this is not strictly true, as first observed by Migdall [50]. This “Migdall effect” arises because the daughter photons are ordinarily polarized, but ordinary polarization is defined as perpendicular to the optic axis of the crystal (and also perpendicular to the direction of propagation of the photon). Thus, this polarization depends also on the emission angle of the SPDC cone, as shown in Fig. 2.8(b). Unfortunately for the engineered source, this effect is especially dramatic for large cone angles, and reaches a 12° deviation from vertical polarization for a 16° SPDC cone opening half-angle [15]. This leads to non-orthogonal polarizations even when the two crystals are orthogonally oriented, and results in a 4% reduction in fidelity with the maximally entangled state.

2.4 Preview: Characterizing the Engineered Source

The next two chapters discuss characterization measurements performed on the engineered source. Chapter 3 describes two independent measurements of the joint spectrum, using two-dimensional Fourier transform spectroscopy and dispersive fiber spectroscopy. These measurements have the advantage of either reconstructing or directly measuring the joint spectrum, which can be a useful diagnostic tool. The disadvantage of these methods is that they are not sensitive to correlations in the joint spectral *phase* which arise from a temporally chirped pump.⁸ Chapter 4 discusses measurements based on correlation functions and two-source HOM interference that directly relate to heralded single-photon purity without regard to the exact form of the joint spectrum. While these techniques do not provide a way to visualize the joint spectrum and thus convey less information, they do directly relate to the heralded single-photon purity, which is typically the value one is most interested in.

These techniques are detailed in the following chapters, but Table 2.2 summarizes them, their relative advantages and disadvantages, and the results of applying them to our engineered source, indicating what techniques one may want to pursue based on the properties one wishes to measure.

⁸For more on temporal chirp and other dispersive effects, see Appendix A.



	Fourier transform	Dispersive Fiber	Correlation Function	Two-Source HOM
Reconstruct Joint spectrum?	Yes	Yes	No	No
Phase-sensitive?	No	No	Yes	Yes
Measurement time	1D: < hour 2D: ~day	< hour	< hour	~day
Implied purity [engineered source]	0.88 ± 0.02 (w/o filters)	0.87 ± 0.03 (w/o filters)	0.66 ± 0.02 (w/o filters)	0.61 ± 0.05 (w/o filters)
	0.99 ± 0.01 (20nm filters)	0.995 ± 0.04 (20nm filters)	1.02 ± 0.02 (20nm filters)	
Other Notes	Most abstract; relatively low resolution	Requires fast detectors and long fibers	Simple measurement and alignment	Most rigorous proof of photon purity

Table 2.2: Comparison of experimental characterization techniques for the joint spectrum

Chapter 3

Measuring the Joint Spectrum

Joint Spectrum? I 'ardly know 'em!

Alternate dissertation title, terrible pun edition

The capability to measure the joint spectral intensity (JSI) is desirable for two practical reasons. First, although a two-source HOM interferometer is the ultimate test for the purity of the single-photon state (a test which we describe in Sec. 4.2), it requires two synchronized sources for a 4-photon experiment. Performing a characterization on a single 2-photon source provides information on factorability with considerably less experimental complexity. Second, examining the joint spectral intensity provides a more detailed view of the source compared to the single-parameter result of the visibility of an HOM interferometer. Indeed, spectral correlations are not the only factor limiting the purity: spatial (polar and azimuthal) correlations will also manifest as a reduction in purity which cannot be immediately separated from the visibility reduction due to the spectral correlations. Therefore, even when a two-source HOM interferometer is used, spectral correlations can only be isolated if spatial alignment is perfect, an impractical assumption.

3.1 Overview of Joint Spectral Measurement

Before evaluating different experimental methods, let's consider the properties of an ideal joint spectral measurement. We would like the measurement to be *accurate*, *simple*, *fast*, and *complete*. *Accurate* meaning the measurement should retrieve the true value of the joint spectrum with minimal distortion or uncertainty. For a *simple* measurement, we require a minimal number of optical components and straightforward alignment, data-collection, and analysis. *Fast* data collection and processing are always desirable, and can make the difference between a practical and impractical measurement. Finally, the measurement should ideally be *complete* in the sense that it is sensitive to any type of spectral correlation, in particular those that are present in either the amplitude or the phase of the joint spectrum. These characteristics sometimes complement each other. For example, a simple measurement is also more likely to be accurate, because fewer optical components and less complex analysis leaves less of a chance for distortions and systematic errors.

Other times they run against each other: a measurement which is fast to perform may also be less accurate and less complete.

Next, we consider the constraints. This is fundamentally a two-photon measurement, so any measurement scheme must rely on some kind of two-photon interaction, either in optics or electronically through coincidence counts between two single-photon detectors. Also, our measurement must somehow be sensitive to the frequency of the photons, because we are after all measuring the joint *spectrum*.

These criteria immediately suggest some possible measurement schemes. The most direct possible measurement would be to measure the frequency of each photon in the pair and estimate a probability distribution from many successive pairs. However, directly measuring the frequency of a single photon is a difficult proposition due to the extremely low energies and very high frequencies involved. Photon frequency is directly related by fundamental constants to energy and wavelength, but these are similarly impractical to measure directly. Fortunately (and sometimes unfortunately), the interactions between photons and optical media often depend directly on frequency, allowing conversion between frequency and some more easily accessible degree of freedom. For example, the angle at which light refracts from a prism or reflects from an optical grating depends on frequency, allowing a measurement of the *position* of a photon to determine its *frequency*.

This principle is used in a scanning monochromator, which uses a narrow slit to determine the position (and thus the frequency) of a photon after a prism or grating. Thus, one could use two scanning monochromators counting photons in coincidence to construct a joint spectral intensity. Such a technique would be relatively simple and accurate, especially if using commercially available monochromators. However, it cannot be particularly fast, as any given photon pair is detected only if both photons pass through their monochromator slits, which for a reasonable resolution leads to a pair collection rate on the order of 0.1%. One could upgrade the scanning monochromator technique to one which determines position with an array of single-photon counters (requiring an array of approximately 20-40 single-photon counters, which must be independently time-resolved or otherwise able to count in coincidence). Such a scheme would extract usable information from every photon pair, but is impractical (though possible) with readily available technology due to the detection and timing analysis electronics required. Thus, we do not use scanning monochromators in this work.

Another possibility is to use Fourier transform spectroscopy to measure frequency in the time domain, as in Sec. 3.2. This exploits a self-interference effect and the property that the extremely short (\sim femtosecond) time regime of the electric field oscillations is easily accessible by an optical delay in a bulk optical medium. This provides a useful characterization of the joint spectrum, but is not an ideal measurement. It is not particularly simple due to the required scanning interferometers and the Fourier transform that relates the

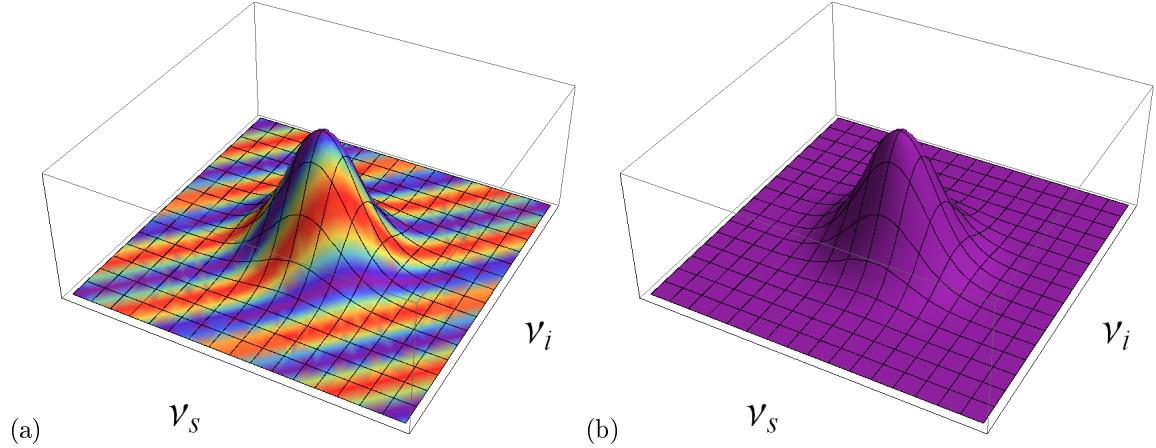


Figure 3.1: Example joint spectra showing joint spectral amplitude (on the vertical axis), and phase (coloring) for both (a) correlated and (b) uncorrelated joint spectra. In both cases, the joint spectral amplitude shows no correlations, illustrating how correlations may be present only in the phase.

time domain measurement to the desired frequency domain result. It is also relatively slow, though Sec. 3.2.2 describes a speed-up that makes the measurement more practical.

Dispersive-fiber spectroscopy, described in Sec. 3.3 provides another useful measurement of the joint spectral intensity [51]. In this scheme, we make use of dispersion in a long optical fiber to convert the spectrum of a photon into a time delay. This technique is one of the most direct measurements of the joint spectral intensity available, and is fast and simple. The main disadvantage of dispersive-fiber spectroscopy is its high sensitivity to timing accuracy in detection electronics.

All the measurements described above have one further flaw: they are not complete in the sense that they only measure the joint spectral intensity, and not the joint spectral phase.¹ However, correlations between the signal and idler photons can be easily present in the phase (see Fig. 3.1) as well as the intensity of the joint spectrum, for example when pumping SPDC with a pump pulse which is not transform-limited². Chapter 4 will discuss measurements that get around this problem. However, if the pump is transform-limited, it is typically acceptable to measure just the joint spectral intensity.

3.2 Fourier Spectroscopy

With this in mind, we turn to the well-established technique of Fourier spectroscopy [52]. This technique relies on the fact that an interferometer with a variable relative path length acts like a Fourier transform from

¹This is analogous to the problem of ultrashort pulse characterization: a spectrometer can easily measure the spectrum of the electric field, but one must take more care when measuring its duration. For example, the self-interference of a pulse after, e.g., a beamsplitter, depends on the intensity, rather than phase, of the spectrum of the electric field. This is critical for “chirped” pulses, where a spectral phase leads to a pulse with a longer temporal duration. Instead, a nonlinear intensity-based effect must be used, for example second-harmonic generation in an autocorrelator, or two-photon absorption in a photodiode.

²See Appendix A for a full discussion of chirped versus transform-limited pulses.

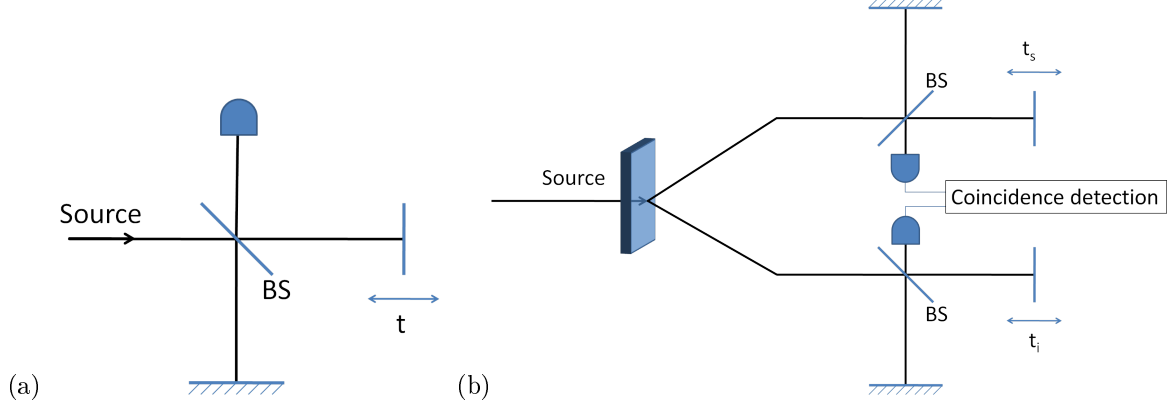


Figure 3.2: Schematic diagram of (a) one-dimensional and (b) two-dimensional Fourier spectroscopy. Both systems use Michelson interferometers, but in the two-dimensional case, the interferometer is duplicated in both arms of an SPDC source, and counts are collected in coincidence.

the frequency domain to the time domain. First, light with an unknown spectrum is sent into a Michelson interferometer, as shown in Fig. 3.2(a). Then, by scanning the relative path length of the interferometer and recording output intensity at regular intervals, a time domain signal is measured. Finally, a Fourier transform can be performed to reconstruct the spectrum of the input light. Mathematically, the interferometer is equivalent to a Fourier cosine transform with an offset term,

$$I(\tau) \propto \int_0^\infty d\omega I(\omega)[1 + \cos(\omega\tau)], \quad (3.1)$$

where $I(\tau)$ is the intensity in the time domain, and $I(\omega)$ is the intensity in the frequency domain. So, by simply computing the inverse transform on the measured data, the spectrum of the signal is recovered:

$$I(\omega) \propto \int_0^\infty d\tau \left(I(\tau) - \frac{1}{2}I(\tau=0) \right) \cos(\omega\tau). \quad (3.2)$$

3.2.1 Two-Dimensional Fourier Spectroscopy

In the context of the downconversion experiment, performing Fourier spectroscopy in either the signal or idler arm allows the measurement of the spectrum of photons in either arm, but gives incomplete information about the joint spectrum. To fully measure the joint spectrum, one can modify this technique, as described by Wasilewski et al. [53]. In this scheme, scanning interferometers are placed in both the signal and idler arms, and coincidence counts are collected, as shown in Fig. 3.2(b). The time-domain data collected by

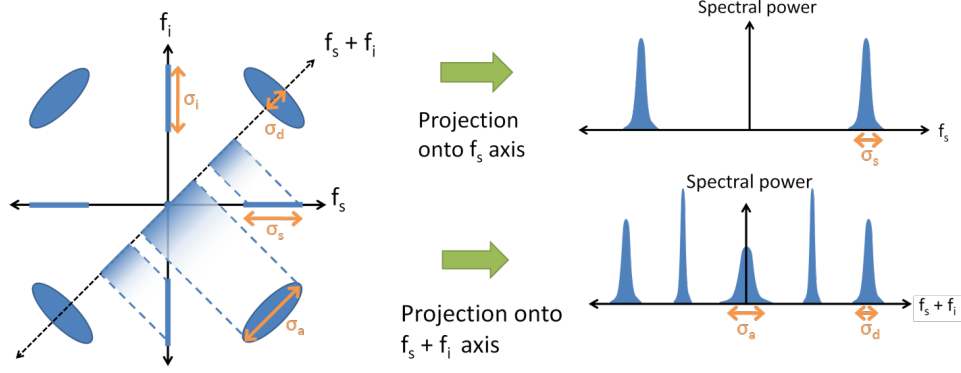


Figure 3.3: Sketch of the frequency-domain signal resulting from two-dimensional Fourier spectroscopy.

independently scanning the interferometers is then related to the Fourier transform of the joint spectrum:

$$I(\tau_s, \tau_i) \propto \int_0^\infty d\omega_s \int_0^\infty d\omega_i I(\omega_s, \omega_i) (1 + \cos(\omega_s \tau_s)) (1 + \cos(\omega_i \tau_i)), \quad (3.3)$$

where $I(\tau_s, \tau_i)$ is the joint temporal intensity (JTI) and $I(\omega_s, \omega_i)$ is the joint spectral intensity (JSI). Analogously to the one dimensional case, performing a 2D Fourier transform on the measured data gives

$$\begin{aligned} \int d\tau_s d\tau_i I(\tau_s, \tau_i) \exp(i\omega_s \tau_s + i\omega_i \tau_i) \\ \propto \delta(\omega_s) \delta(\omega_i) \langle \hat{N}_s \hat{N}_i \rangle + \frac{1}{2} \delta(\omega_s) \langle \hat{N}_s \hat{I}_i(\omega_i) \rangle + \frac{1}{2} \delta(\omega_i) \langle \hat{N}_i \hat{I}_s(\omega_s) \rangle + \frac{1}{4} I(\omega_s, \omega_i), \end{aligned}$$

where \hat{N}_s and \hat{N}_i are the number operators for signal and idler photons, and $\hat{I}_s(\omega_s)$ and $\hat{I}_i(\omega_i)$ are the spectral intensities of the signal and idler beams. The resulting terms are represented visually in Fig. 3.3. Because the Fourier cosine transform is even, the result is symmetric about the ω_s and ω_i axes. The first term is located at the origin and is proportional to the total number of coincidence counts. The middle terms are located on the axes and provide information about the spectrum of the signal or idler photons conditioned on the detection of the conjugate photon. The term of interest is the final term, which is proportional to the JSI.

3.2.2 Diagonal Fourier Spectroscopy

Unfortunately, collecting two dimensional data is very time consuming compared to one dimensional Fourier spectroscopy, requiring N^2 rather than N points to obtain the same resolution. However, under the assumption that the JSI is approximately Gaussian (which is valid for our source), we can take advantage of the

structure of the two-dimensional spectrum to measure the relevant parameters with a one-dimensional scan. Specifically, the correlations between the signal and idler are manifested in the diagonal dimensions of the gaussian ellipse. So, taking the Fourier transform of a 1D scan along the $t_s + t_i$ axis yields the projection of the 2D spectrum along the $f_s + f_i$ axis, as shown in Figure 3.3. If we model the joint frequency spectrum as a 2D Gaussian ellipse, the relevant parameter for spectral correlation is the ratio of the peak widths along the $f_s + f_i$ and $f_s - f_i$ axes, σ_d/σ_a . The parameters σ_d and σ_a can be extracted directly from the 1D scan described above, characterizing the Gaussian ellipse

$$f(\nu_s, \nu_i) = A \exp \left[-(\nu_s^2 + \nu_i^2) \left(\frac{1}{4\sigma_d^2} + \frac{1}{4\sigma_a^2} \right) - 2\nu_s\nu_i \left(\frac{1}{4\sigma_a^2} - \frac{1}{4\sigma_d^2} \right) \right]. \quad (3.4)$$

Recall from Eqs. 2.5 and

$$f(\nu_s, \nu_i) = A \exp \left[-\frac{\nu_s^2 + \nu_i^2}{2\sigma^2} - \frac{2\nu_s\nu_i}{2\sigma^2} \right] \exp \left[-\frac{\nu_s^2}{2\sigma_f^2} \right] \exp \left[-\frac{\nu_i^2}{2\sigma_f^2} \right], \quad (3.5)$$

we can write the heralded single-photon purity P (or equivalently, the inverse Schmidt number $1/K$) as

$$P = \sqrt{1 - \frac{1}{\left(1 + \left(\frac{\sigma}{\sigma_f}\right)^2\right)^2}}. \quad (3.6)$$

Applying a change of variables

$$\frac{1}{2\sigma_d^2} + \frac{1}{2\sigma_a^2} = \frac{1}{\sigma^2} + \frac{1}{\sigma_f^2} \quad (3.7)$$

$$\frac{1}{2\sigma_a^2} - \frac{1}{2\sigma_d^2} = \frac{1}{\sigma^2}, \quad (3.8)$$

we can see that Eq. 3.4 and Eq. 3.5 are equivalent. Solving for σ_a and σ_d in terms of σ and σ_f , we can rewrite Eq. 3.6 as

$$P = \sqrt{1 - \left(\frac{r-1}{r+1} \right)^2}, \quad (3.9)$$

where $r \equiv \sigma_d^2/\sigma_a^2$.

3.2.3 Measurements

Fig. 3.4 shows our experimental setup. The critical difference between this and the theoretical discussion above is the use of a common-path polarization interferometer rather than a Michelson. This achieves the same function by providing an optical path length difference due to the different indices of refraction

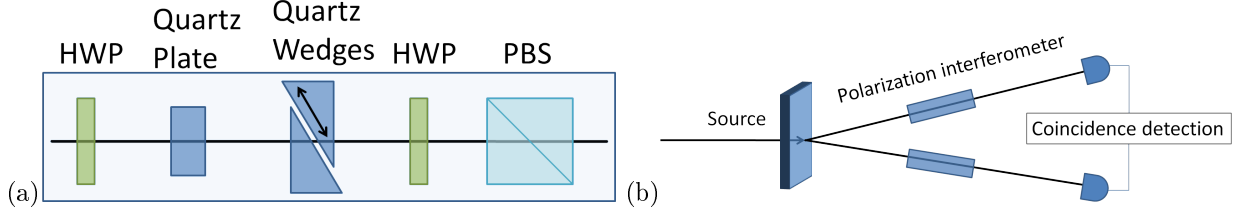


Figure 3.4: Diagram of 2D Fourier spectroscopy setup for measuring the joint spectrum. The common-path polarization interferometer in (a) uses a half-wave plate (HWP) to rotate light into the diagonal basis, followed by a birefringent quartz plate to initially delay horizontally polarized light (H) relative to vertically polarized light (V). Then, quartz wedges are used to variably delay V relative to H. Finally, another HWP rotates back into the H/V basis and a polarizing beam splitter (PBS) is used to pick off the H component. Two of these polarization interferometers are used in (b) to analyze the joint spectrum.

of ordinarily and extraordinarily polarized light in birefringent quartz, rather than a physical path length difference. Specifically, horizontally polarized light is rotated into the diagonal basis using a half-wave plate³ before passing through scanning quartz wedges with a vertical optic axis. Thus, diagonally polarized light is a superposition of ordinary and extraordinary polarization in the crystal, which pick up different phases,

$$|D\rangle = \frac{|e\rangle + |o\rangle}{\sqrt{2}} \rightarrow \frac{1}{\sqrt{2}} \left(e^{2\pi i n_e L/\lambda} |e\rangle + e^{2\pi i n_o L/\lambda} |o\rangle \right), \quad (3.10)$$

where L is the length of quartz, λ is the wavelength and n_o and n_e are the ordinary and extraordinary indices of refraction at that wavelength (see Fig. 1.1c). For our quartz wedges (custom-made by Rocky Mountain Instruments) at 810 nm, with a wedge angle of 32° and one wedge mounted on a translation stage, this corresponds to a relative delay of 15.75 femtoseconds per millimeter of stage motion (where 2.7 fs corresponds to 2π of relative phase). A fixed-length quartz plate is used to provide a delay offset in the opposite direction using an optic axis mounted orthogonally to that of the wedges. Finally, the polarization is rotated back to the H/V basis and analyzed on a polarizing beamsplitter. The probability P of observing a horizontally polarized photon, i.e., the photon exiting the horizontal port of the PBS, depends on the relative phase $\Delta\phi \equiv 2\pi L(n_o - n_e)/\lambda$ as

$$P = \cos(\Delta\phi)^2 = \frac{1}{2} (1 + \cos(2\Delta\phi)). \quad (3.11)$$

The advantage of this technique is that the two optical paths take the same physical path, making the interferometer much more robust against vibrations and thermal fluctuations.

Fig. 3.5 shows typical results from applying this technique to our single-source SPDC setup, and illustrates

³Due to the broad bandwidth involved, one must take care to use waveplates with a flat retardance (that is, the optical path-length difference between ordinary and extraordinary polarization $L_e - L_o$) in the area of interest.

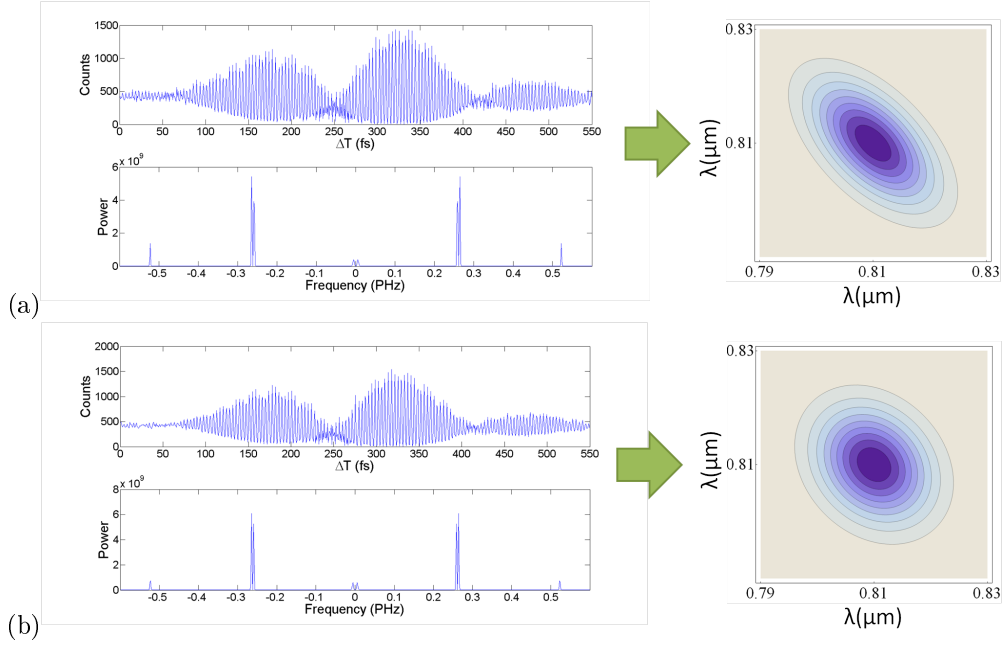


Figure 3.5: Experimental measurement of joint spectrum for (a) a pump bandwidth of 2.6 nm, resulting in an estimated purity of 0.84 and (b) a pump bandwidth of 5.2 nm, resulting in an estimated purity of 0.96. The ellipses represent the joint spectrum, with the eccentricity along the diagonal providing spectral correlation (or in this case, anti-correlation). The purity numbers here apply only to the spectral state of heralded single photons, and represent the degree of factorability of the joint spectrum. This is an upper bound on the expected visibility of a two-source HOM dip.

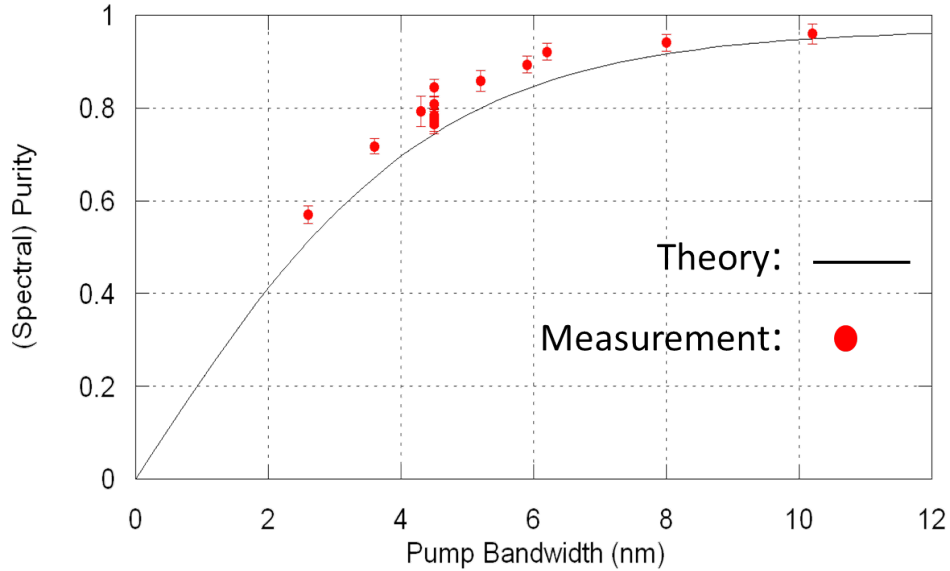


Figure 3.6: Measured purity as a function of pump bandwidth, compared with a theoretical model [44]. The measurements systematically over-estimate the purity due to the approximations used when reconstructing the joint spectrum from the diagonal Fourier transform interferometric data.

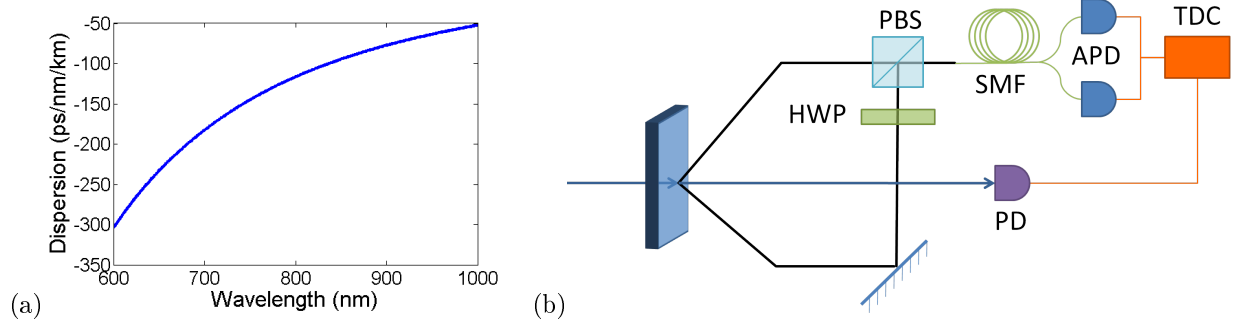


Figure 3.7: (a) Dispersion as a function of wavelength for single-mode 780HP fiber from vendor specifications. (b) Schematic diagram of fiber spectroscopy. A half wave plate (HWP) and polarizing beamsplitter (PBS) are used to combine the signal and idler modes into a 400-m length of single-mode fiber (SMF). A fiber beamsplitter delivers light to two avalanche photodiodes (APD), which are analyzed by a time-to-digital converter (TDC) together with a synchronization signal from the pump via a photodiode (PD).

the reconstruction of the joint spectrum from the measured data. The spectrum is Fourier transformed to the frequency domain, and then a Gaussian fit is applied to peaks corresponding to the diagonal widths of the joint spectrum. From this, the heralded single-photon purity is determined by Eq. 3.9. This measurement was used to show that the spectral purity has the expected dependence on pump bandwidth, as shown in Fig. 3.6.

3.3 Fiber Spectroscopy

As mentioned previously, interferometry is not the only method for transforming the spectral information of the two-photon state into something measurable. Another promising technique—“fiber spectroscopy”—uses dispersion in an optical fiber to convert frequency to time [51]. This exploits the property that short wavelengths travel slower through an optical medium (with ordinary dispersion) than long wavelengths. Fig. 3.7(a) shows this dependence for single-mode 780HP fiber, which has dispersion of approximately -120 ps/nm/km for light near 810 nm. For 400 m of fiber, a photon with a wavelength of 809 nm, for example, will be delayed by approximately 50 ps compared to a photon at 810 nm. Thus, measuring the time of arrival of a photon determines its wavelength, assuming the relative delay exceeds the detector timing jitter.

The experimental schematic is diagrammed in Fig. 3.7(b). The signal and idler photons are combined into a single mode by rotating the polarization of the idler photons and combining with the signal photons on a polarizing beamsplitter. We use 400 m of Nufern 780HP fiber to convert frequency information to timing. Detection is done with two Micro Photon Devices avalanche photodiodes (APDs) with custom circuitry provided by Mario Stipcevic, chosen for low jitter (see Sec. 3.3.1). It may seem that only one APD is

necessary because the extra free-space path length in the idler arm causes the signal photon to always arrive at the APD before the idler photon. However, this time difference is on the order of a nanosecond, while the dead-time of the APD is over 20 nanoseconds, so a fiber beamsplitter delivers the photons to two APDs to probabilistically eliminate the dead-time. There is a 50% chance the photons will arrive at different APDs and can be measured in coincidence, and a 50% chance that the photons will arrive at the same APD and no coincidence will be seen. This could be improved by using two separate lengths of fiber, but resources are typically better spent on obtaining one longer loop of fiber, as the length of fiber determines the amount of dispersion experienced by the photons, and thus the resolution of the measurement. The output pulses from the detectors are registered by an Agilent U1051A time-to-digital converter (“time-tagger”) [with 50 ps time-bin resolution] and counted in coincidence. The coincidence signal is referenced to an Electro-Optics ET-2030 photodiode measuring the pump, also registered by the time-tagger. Data acquisition and post-processing is done with the aid of a custom driver software package written by Daniel Kumor.

The time-tagger is so named because it takes input pulses on a number of channels and “tags” them with a time of arrival. This allows convenient digital post-processing of events, with the ability to find coincidences between arbitrary channels with arbitrary delay and coincidence window, all of which can be changed after the data is collected. The result is a very powerful tool for applications from simple singles and coincidence counting, to correlation-based jitter measurements (Sec. 3.3.1), to complex multi-fold coincidences (Sec. 3.3.2).

3.3.1 Calibration

In fiber spectroscopy, the timing jitter of the detection electronics places a critical limit on the accuracy of the measurement. Essentially, a high-jitter detector will lead to an uncertainty in the frequency-time relationship, as shown in Fig. 3.8. This effect limits the resolution of the measurement, leading to a more circular joint spectrum and an artificially lower Schmidt number. Thus, calibration is essential to determining the accuracy of the measurement.

This calibration entails measuring the jitter of each component in the experimental setup. Jitter can be measured using the time-tagger in two ways: either a low-jitter periodic signal can be used to activate the device in question, or an arbitrary but highly-correlated signal can be used to activate two devices. In the first case, the autocorrelation of time tags on one channel gives a series of peaks where each is the convolution of the time response of the device with itself (in the limit of a perfectly periodic signal). In the second case, the correlation of time tags on two channels gives one peak which is the convolution of the two devices. The autocorrelation method is generally preferable (and was used in these measurements),

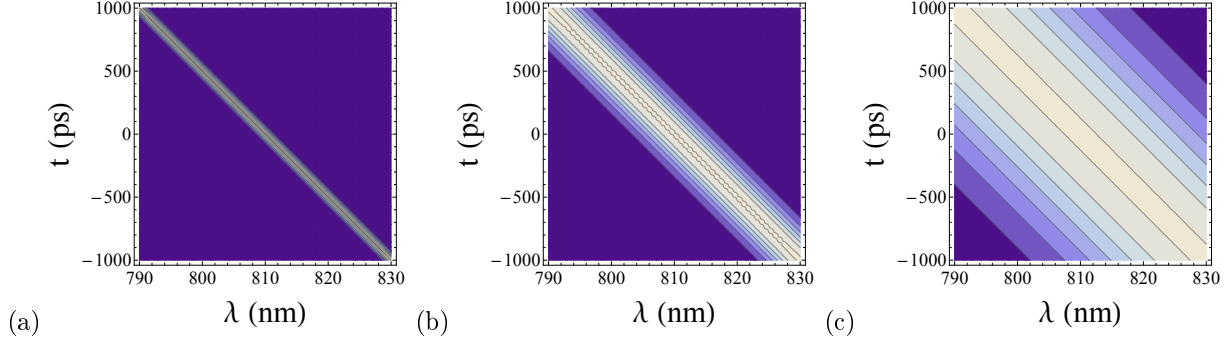


Figure 3.8: Wavelength/time relationship for detection with timing jitter of (a) 50 ps, (b) 240 ps, and (c) 1 ns. Coloring shows the probability of observing a particular relative timing delay for a photon of a given wavelength, or vice-versa. A broader probability distribution leads to a larger uncertainty when determining wavelength from arrival time.

as it isolates the behavior of one device, but the correlation method can be superior in the case where a highly correlated signal can be used and a low-jitter device is available to measure the time response of a high-jitter device. Several detectors were characterized to determine which had the best performance, with measurement results shown in Fig. 3.9. The best-performing detectors were MPD avalanche photodiodes (with custom circuitry from Mario Stipcevic), which have a reasonably low jitter of 174 ps and do not have a significant non-Gaussian tail. Although the ID Quantique detectors have a lower FWHM jitter (70 ps), they also have a long tail with a significant portion of the total power (over 50% outside of FWHM, compared to approximately 24% for a Gaussian), which severely reduces the resolution of the measurement. The time response of the time-tagger itself was measured using the correlation method, with a function generator simultaneously triggering two channels on the time-tagger. This yielded a FWHM jitter of 64 ps, which is deconvolved from all other jitter measurements. Additionally, the time response of the Electro-Optics photodiode was measured, yielding a FWHM jitter of 203 ps. Adding the jitter values in quadrature gives a total-system jitter of $\sqrt{203^2 + 174^2 + 64^2} = 275$ ps.

We can compare this with measurements obtained using fiber spectroscopy on one input. This measurement is similar to that pictured in Fig. 3.7 except that instead of an SPDC source and two APDs measuring in coincidence, there is only the pump, which is sent to a photodiode and a single APD. Additionally, the pump is optionally filtered by a low-pass filter to observe the response to a sharp cutoff. The time response is determined by looking at the correlation between the APD and the photodiode, with the photodiode serving as a fixed point of reference. This is converted to a spectrum by multiplying by a conversion factor determined by the length and dispersion of the fiber, and a manual offset which varies depending on delays present in the experiment, but is not important to the shape of the spectrum. Finally, this is compared to a direct measurement of the pump spectrum with an Ocean Optics HR2000 spectrometer, which is also

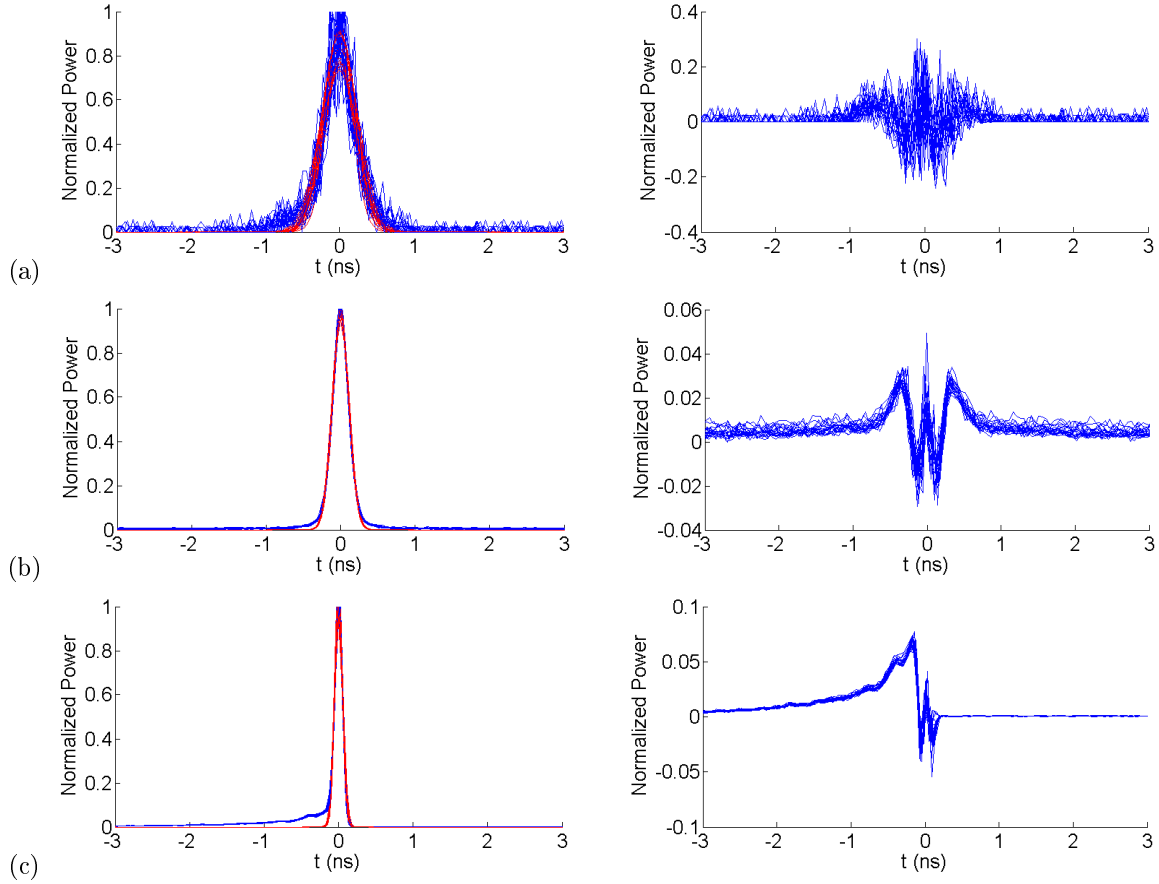


Figure 3.9: Detector autocorrelation (left) with Gaussian fit and residuals with respect to the fit (right) for detectors from (a) Perkin-Elmer (b) ID Quantique, (c) Micro Photon Devices with custom circuitry from Mario Stipcevic. Full-width at half-max detector jitters (after deconvolving the measured 64-ps jitter of the time-tagger) are (a) 358 ps, (b) 70 ps, (c) 174 ps. Although the ID Quantique has the lowest FWHM, it has a large non-Gaussian tail.

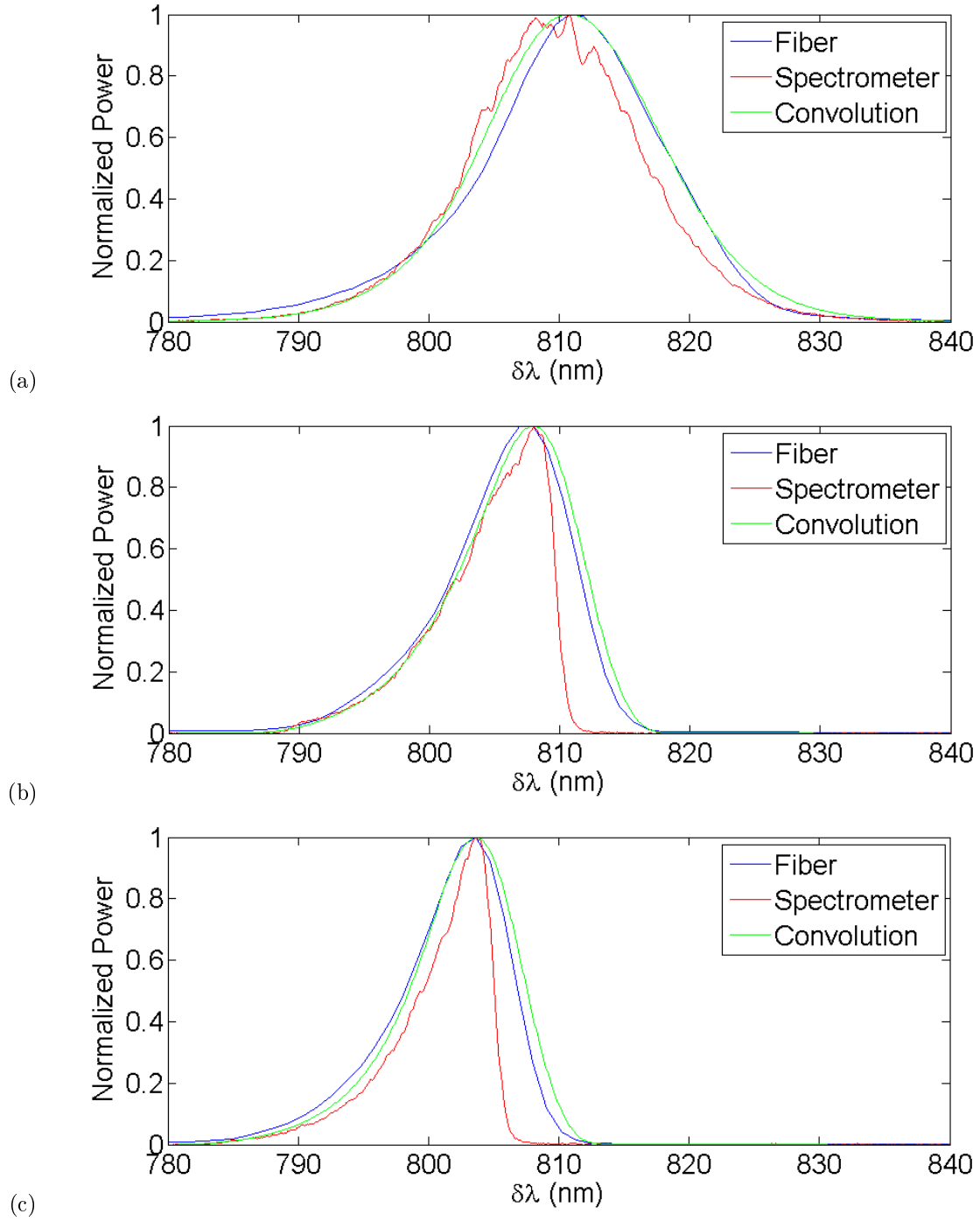


Figure 3.10: Normalized spectral power density measurements under (a) no filtering, (b) 810-nm low-pass filtering, (c) 805-nm low-pass filtering. The measured spectrum from an Ocean Optics HR2000 spectrometer is shown in red. The inferred spectrum from the fiber spectroscopy is shown in blue, re-centered on the peak of the spectrometer measurement (as the measurement only gives wavelength relative to an arbitrary reference). The green line shows the convolution of the spectrometer data with a 276-ps FWHM Gaussian.

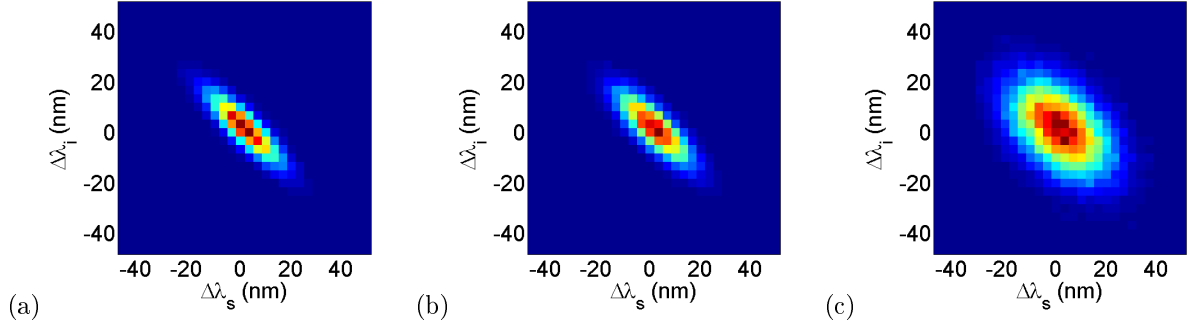


Figure 3.11: Monte Carlo simulations of fiber spectroscopy with a detection timing jitter of (a) 50 ps, (b) 276 ps, and (c) 1 ns. Simulated detector photons are detected with a Gaussian random jitter and binned into a 2D histogram with 50-ps time bin widths (the bin width of the Agilent U1051A time-to-digital converter). The true Schmidt number of this simulated source is 2.0, and the Schmidt numbers after the application of jitter are (a) 1.98 ± 0.02 , (b) 1.68 ± 0.01 , (c) 1.14 ± 0.003 . A Richardson-Lucy deconvolution operation can be applied to attempt to remove the effect of the jitter, but this compensation breaks down for large jitters, resulting in (a) 1.98 ± 0.02 (b) 1.99 ± 0.02 , (c) 1.20 ± 0.007 . The simulation was performed with 32,000 simulated photon pairs, a fairly typical number for our experimental measurements.

mathematically convolved with a Gaussian equivalent to a system jitter of 276 ps. Fig. 3.10 shows the results of this measurement, which exhibits reasonable agreement between the directly measured spectrum and the fiber-spectroscopy-measured spectrum, given the characterized jitter of the system.

3.3.2 Joint Spectral Measurement and Simulation

The effect of jitter can be simulated by convolving an expected joint spectrum with a Gaussian point-spread function, as shown in Fig. 3.11. The simulation uses a Monte Carlo technique, with photons drawn from an assumed spectrum receiving random jitters to produce a transformed spectrum. This allows an estimate for the uncertainty of the experimental measurements. We can also attempt to remove the detector response using a Richardson-Lucy⁴ deconvolution [54]. This is reasonably successful for removing a relatively small jitter, but breaks down as jitter increases. As a rough rule of thumb, deconvolution is unnecessary if the jitter is less than half as large as the smallest spectral feature (i.e., the narrow axis of the ellipses of Fig. 3.11), and is unreliable if the jitter is more than 2-4 times larger than the smallest spectral feature (the latter criteria depends on the amount of noise and the shape of the features). Jitter on the order of the feature size is a “sweet spot” for applying deconvolution.

To perform the full joint spectral measurement, we need to perform a complex multi-channel correlation. This is not a typical use of the time-tagger, and is not directly supported by the default configuration of

⁴Richardson-Lucy is an iterative maximum-likelihood-based deconvolution algorithm developed for image processing, specifically for removing a Gaussian blur from an image. Initially, we attempted to use a naive matrix-inversion-based deconvolution, but this proved to be numerically unstable for this problem due to the high condition number of the joint-spectral matrix.

the driver software, so some modifications must be made. The basic idea of the measurement is to count in three-fold coincidence between the APDs and the photodiode, with each triple-coincidence event being registered as an event with $\Delta\lambda_s \approx t_s - t_{pd}$ and $\Delta\lambda_i \approx t_i - t_{pd}$, where t_s , t_i , and t_{pd} are the timestamps of the signal photon, idler photon, and photodiode pulse. The set of all such events can be binned into a two-dimensional relative-timing histogram, then converted to wavelength to produce a joint spectrum similar to those of Fig. 3.11 (see Fig. 3.12). Finally, the Schmidt decomposition can be applied to this histogram to determine the Schmidt number as in Sec. 2.1.1.

Unfortunately, directly accessing these arrival times on all three channels is not practical given the extremely large number of time-tags involved.⁵ Instead, we make use of a fast and efficient multi-coincidence routine in the driver software. This allows the fast construction of the desired histogram by the following method: first, we observe that each bin in the histogram corresponds to a three-fold coincidence with offsets Δt_s and Δt_i and window size equal to the histogram bin width. Then, by iterating over all offsets in the desired range, we can construct the desired histogram. However, due to the large amount of data collected, even the optimized functions used in this routine run slow enough to make the measurement impractical. Here we can make use of another optimization by noticing that the vast majority of the collected data is from photodiode counts, which occur with every laser pulse. However, the photodiode counts are only useful if they are directly followed or preceded by a (relatively rare) APD count; otherwise they are superfluous. We fix this by modifying the timetagger software such that, rather than recording every event in the buffer, it only records the photodiode events if they are immediately before or after an APD event.⁶ This ends up discarding approximately 99.997% of the data, which enables a speedup of about four orders of magnitude. A comparison of the results of this technique with both Fourier spectroscopy and a fully simulated version of our source from Alfred U'Ren and Karina Garay is shown in Fig. 3.12.

⁵The Tsunami operates at 76 MHz; at 9 bytes per time-tag this is 435 megabytes of data per second from the photodiode alone, a challenge for processing on even a powerful desktop.

⁶How does this work? Picture the timetagger buffer as a long tape with discrete bins, each of which can hold a timetag. The driver normally always writes to one bin and then moves to the next. With the modification, if the timetagger has just written two photodiode counts in a row, it keeps rewriting photodiode counts into the current bin until it receives an APD count, in which case it advances to the next bin.

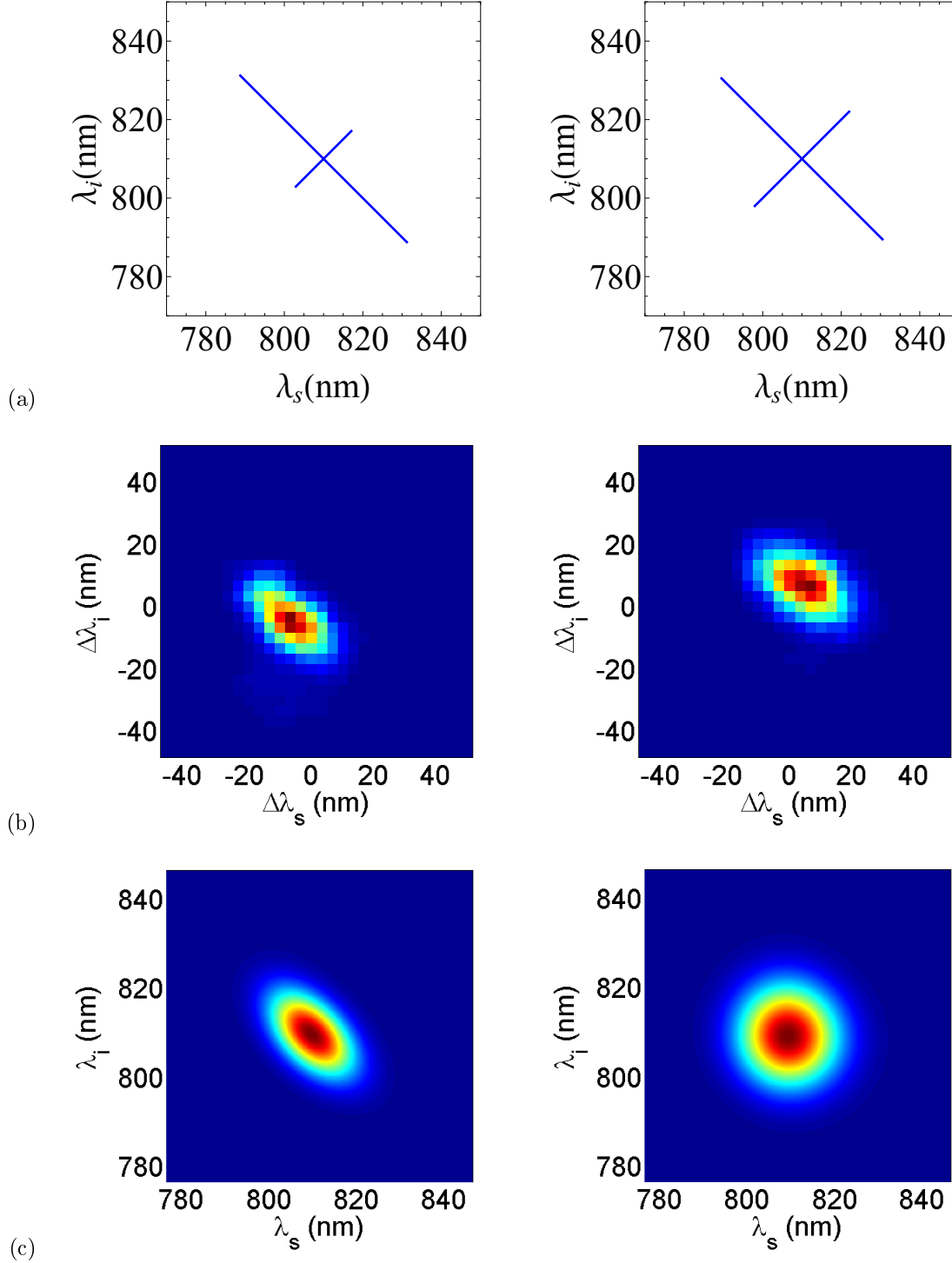


Figure 3.12: Comparison of measurements and simulations from different techniques for a source with no spectral filtering. The left column is for a 4-nm pump, while the right column is for an 8-nm pump. Rows correspond to (a) diagonal Fourier spectroscopy (purity of 0.62 ± 0.02 and 0.88 ± 0.02) and (b) fiber spectroscopy (purity of 0.83 ± 0.02 and 0.87 ± 0.03) are compared to (c) simulations performed by our collaborators Alfred U'Ren and Karina Garay (purity of 0.862 and 0.998). This shows two effects: for both pump bandwidths, the purity of our source is lower than predicted theoretically. Secondly, the two measurement techniques agree for large pump bandwidth, but the detector response of the fiber spectroscopy method limits the accuracy in the low bandwidth case.

Chapter 4

Measuring Heralded Photon Purity

Most of what we do is just an alignment issue.

Heard at group meeting

Chapter 3 described measurements of the two-photon joint spectrum from SPDC, but these all neglect one important component: the joint spectral phase (see Fig. 3.1). Rather than measuring the joint spectral phase directly,¹ we can measure just the quantity we ultimately want: the purity of a heralded single photon. We approach this problem in two ways: indirectly by taking advantage of the statistical properties of SPDC (Sec. 4.1), and directly by interfering heralded single photons from two SPDC sources (Sec. 4.2).

4.1 Correlation Function Measurement

4.1.1 Photon Bunching

If the fundamental difference between quantum and classical optics is that we picture light as a series of discrete photons rather than as a continuous wave, then an obvious question to ask is: How many photons will we see, and when will we see them? The first part of the question is of course easily answered by dividing the optical power by the photon energy, but this leaves considerable ambiguity in the statistics of when the photons arrive. For example, do they arrive one after another at regular intervals, or as completely unpredictable independent random events, or perhaps with a tendency for multiple photons to “bunch” together closely in time? Any of these possibilities can occur depending on the mechanism responsible for producing the photons, and measuring the photon statistics can provide significant insight about a source. For example, it can be shown that a classical light source can lead to photon statistics which are random² (Poissonian) or bunched, but regularly spaced (“anti-bunched”) photons are a distinct marker of quantum

¹Can the joint spectral phase be measured directly? It may be possible to generalize a technique like FROG or SPIDER, but this would not be trivial, and is outside of the scope of this work.

²Specifically, we mean a stream of photons that follows a Poisson process. That is, each photon event is independent of all other photon events, and for any given time interval τ , the expected number of photons observed depends *only* on τ and the time-independent average photon number \bar{n} .

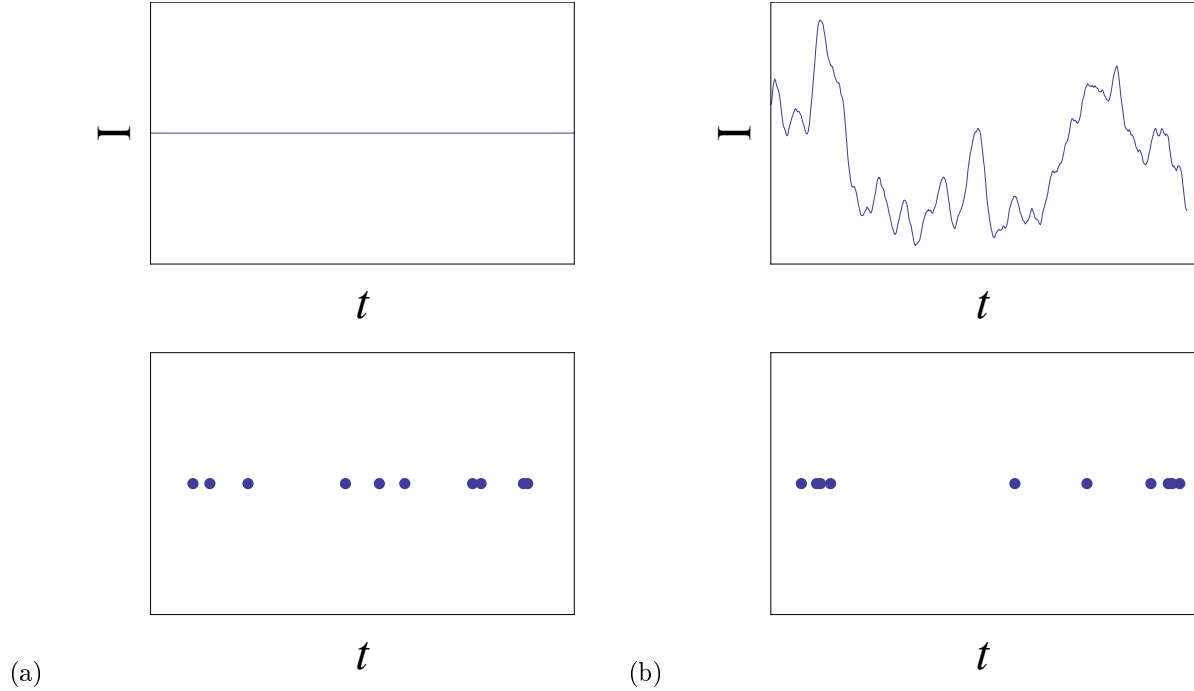


Figure 4.1: Monte Carlo simulations illustrating how photon bunching arises from intensity fluctuations in a (classical) electromagnetic field. Intensity and photon arrival are shown as a function of time for (a) a perfectly coherent (Poissonian) source and (b) a thermal source. The coherent source has a constant intensity and photons are as likely to arrive at one time as at any other, while a thermal source has an intensity which varies chaotically on short timescales due to randomly varying phases of emitters, leading to bunching in photon arrival time.

light and cannot be reproduced in a semi-classical theory.³

Although anti-bunched light is of significant interest in quantum optics, in this section we are primarily concerned with bunched and Poissonian⁴ light. These are both classical phenomena, and can be understood in the semi-classical picture of a classical electromagnetic field coupled to a quantized detector. A coherent electromagnetic field has constant intensity over time, and so a photon is as likely to be detected at any one given time as it is at any other. However, a thermal source has a chaotically fluctuating intensity. Intuitively, this leads to photon bunching [56] because photon probability is proportional to intensity (see Fig. 4.1).

Recalling that SPDC amplifies vacuum fluctuations, one would expect that it would exhibit photon bunching. Indeed, this property is well-studied theoretically [57] and experimentally [58, 59]. Importantly, this is only true when measuring a single spatial-spectral mode. With a detector coupled to multiple modes,

³It's a quick and worthwhile exercise to unfamiliar the reader to consider why this is the case. (Hint: consider the difference between Fig. 4.1(a) and (b) and try to picture an electric field capable of producing anti-bunching.)

⁴The terminology here is slightly problematic; light with this statistical nature is sometimes referred to as coherent, random, or Poissonian. Observing Poissonian statistics does not imply coherence (though the reverse is true). Random is insufficient by itself, as there are infinitely many other possible “random” probability distributions besides that observed. Poissonian, then, is perhaps the least problematic term, though care must be taken not to conflate super-Poissonian and sub-Poissonian statistics with bunching and anti-bunching, because while these effects often occur together, they are not equivalent, and sub-Poissonian and super-Poissonian statistics can in principle accompany photon bunching and anti-bunching, respectively [55].

the independent modes will not interfere with each other but will instead average out to a flat intensity, resulting in Poisson statistics in the limit of many modes (the same will happen even in a single mode if taking a time average over a period longer than the intensity fluctuations). This averaging over modes and time made photon bunching difficult to observe fully until the relatively recent availability of fast and efficient single-photon detectors.⁵ With modern sources and detectors, photon statistics are readily and routinely observed, and measurements are precise enough to determine even the number of thermal modes being averaged, which we will take advantage of in this section.

4.1.2 Electric Field Correlation Functions

But first, we'll briefly consider photon bunching in terms of the first- and second-order electric field correlation functions $g^{(1)}(\tau)$ and $g^{(2)}(\tau)$ (roughly following Chapter 3 of Loudon [60]; see the text for a more complete treatment). The first can be written in terms of time-averaged products of the electric field $E(t)$ as

$$g^{(1)}(\tau) = \frac{\langle E^*(t)E(t+\tau) \rangle}{\langle E^*(t)E(t) \rangle}. \quad (4.1)$$

This quantifies the first-order coherence time, which can be interpreted as the achievable visibility in an interferometer in which one arm has a delay of τ relative to the other. For monochromatic light, $g^{(1)}(\tau)$ is 1 for all values of τ , with a minimum of 0 for incoherent light (and also generally approaching 0 for $\tau \rightarrow \infty$).

However, this first-order coherence has nothing to say about bunching or anti-bunching. For this, we turn to a higher-order function based on intensity (the second power of the electric field),

$$g^{(2)}(\tau) = \frac{\langle I(t)I(t+\tau) \rangle}{\langle I(t) \rangle^2}. \quad (4.2)$$

This describes the statistics of intensity fluctuations in the electric field, or equivalently fluctuations in photon number. To see how, consider an electric field produced by a large number of incoherent emitters (e.g., atoms). In the case of a second-order (i.e., two-photon) emission, it is far more likely that the two photons arose from separate emitters rather than twice from the same emitter. We take advantage of this

⁵The Hanbury Brown-Twiss intensity interferometry experiment observed a signature of thermal stellar light in 1956 using slow and inefficient (by today's standards) detectors, but the correlation observed was much smaller than theoretically allowed.

to write, in terms of the individual emitters' intensity contributions I_i ,

$$\langle I(t)I(t-\tau) \rangle = \sum_{a,b \in n} \langle I_a(t)I_a(t-\tau) + I_a(t)I_b(t+\tau) + I_b(t)I_a(t+\tau) \rangle \quad (4.3)$$

$$= \langle nI_a(t)I_a(t-\tau) + nI_a(t)(n-1)I_b(t+\tau) + nI_b(t)(n-1)I_a(t+\tau) \rangle \quad (4.4)$$

$$\approx 2n^2 \langle I_a(t) \rangle \langle I_a(t+\tau) \rangle \quad (4.5)$$

$$= 2 \langle I(t) \rangle \langle I(t+\tau) \rangle, \quad (4.6)$$

where we have made the approximation that $n \gg 1$. For $\tau = 0$, the entire expression in Eq. 4.2 reduces to $g^{(2)}(0) = 2$. Note that the specific expansion here is valid only because the emitters are all incoherent and a pair of emitters a and b are distinguishable by their phases. For a coherent source, intensity does not vary in time, and $g^{(2)}(\tau) = 1$.

4.1.3 Measuring Photon Correlation

Having established how $g^{(2)}(\tau)$ relates to the statistical character of the light, we consider how it is measured. The second-order correlation function is straightforward to measure with a Hanbury Brown-Twiss interferometer [61], as shown in Fig. 4.2(a). This scheme uses single-photon detection and coincidence analysis, relying on the property that the photon flux $n(t)$ is proportional to the intensity $I(t)$, so we can write $g^{(2)}(\tau)$ as the ratio of coincidence and singles counts in two single-photon detectors after a beamsplitter as

$$g^{(2)}(\tau) = \frac{\langle n_1(t)n_2(t+\tau) \rangle}{\langle n_1(t) \rangle \langle n_2(t) \rangle}. \quad (4.7)$$

This measurement is simple to perform with single-photon detectors, though one must take care that the probability of multiple photons arriving during the detector “dead-time” is near zero,⁶ or that photon-number-resolving detectors are used. We satisfy this condition by using a pump with an average photon number per pulse much less than 1 (approximately 0.001). However, Eq. 4.7 also assumes that the detector response time is fast compared to the coherence time, which is not the case in our source: our broadband pulses have coherence times in the tens of femtoseconds, while APD's have typical response times in the hundreds of picoseconds! For a continuous-wave source, any photon bunching would be entirely washed out by this slow response. Fortunately, this is not the case for a pulsed source, as we will see. With a long detector response compared to a single pulse, we instead measure the time-integrated correlation function

⁶Specifically, the number of missed counts n_{dead} should be much less than the number of detected counts $n_{detected}$.

[62]

$$g^{(2)} = \frac{\int dt_1 dt_2 \langle n_1(t_1) n_2(t_2) \rangle}{\int dt_1 \langle n_1(t_1) \rangle \int dt_2 \langle n_2(t_2) \rangle}, \quad (4.8)$$

where the integral is taken over the detection window, assumed to be long compared to the pulse duration.

This appears intimidating at first, but if we consider the pulse as a mixed state of K spatial/temporal/polarization modes, then we can take this integral as the sum over those modes,

$$g^{(2)} = \sum_{i=1}^K \frac{\left\langle \left(\sum_{i=1}^K \hat{n}_i \right)^2 \right\rangle}{\left\langle \sum_{i=1}^K \hat{n}_i \right\rangle^2}, \quad (4.9)$$

where \hat{n}_i is the photon number operator for mode i .⁷ Let's consider a concrete example of two independent polarization modes, H and V, each in a thermal state:

$$g^{(2)} = \frac{\langle (\hat{n}_H + \hat{n}_V)^2 \rangle}{\langle \hat{n}_H + \hat{n}_V \rangle^2} \quad (4.10)$$

$$= \frac{\langle \hat{n}_H^2 + 2\hat{n}_H\hat{n}_V + \hat{n}_V^2 \rangle}{\langle \hat{n}_H \rangle^2 + \langle \hat{n}_H \rangle \langle \hat{n}_V \rangle + \langle \hat{n}_V \rangle^2} \quad (4.11)$$

$$= \frac{\langle \hat{n}_H^2 \rangle + 2\langle \hat{n}_H\hat{n}_V \rangle + \langle \hat{n}_V^2 \rangle}{4\langle \hat{n} \rangle^2} \quad (4.12)$$

$$= \frac{1}{2} \left(\frac{\langle \hat{n}^2 \rangle}{\langle \hat{n} \rangle^2} + \frac{\langle \hat{n}_H\hat{n}_V \rangle}{\langle \hat{n} \rangle^2} \right), \quad (4.13)$$

where we have assumed for simplicity that the two modes are equally occupied, so, e.g., $\langle \hat{n}_H \rangle^2 = \langle \hat{n}_V \rangle^2 \equiv \langle \hat{n} \rangle^2$. The first term represents a single-mode thermal state, and has a value of 2. The second term, however, depends on correlations between the H and V modes. These are independent, uncorrelated modes, and so no photon bunching occurs, and this term takes a value of 1. Thus, the sum for our two-mode state is $g^{(2)} = 3/2$.

This generalizes to the sum over K thermal modes⁸ as

$$g^{(2)} = 1 + \frac{1}{K}, \quad (4.14)$$

which is shown in Fig. 4.2(b). So, measuring $g^{(2)}$ directly determines the effective number of modes as $K = 1/(g^{(2)} - 1)$. But recall from Chapter 2 that the heralded single-photon purity is also related to

⁷Note on notation: we let the product of photon number operators follow normal ordering of creation and annihilation operators.

⁸Above we assumed equally occupied modes. For unequally occupied modes, K follows the definition of the Schmidt number from Eq. 2.4.

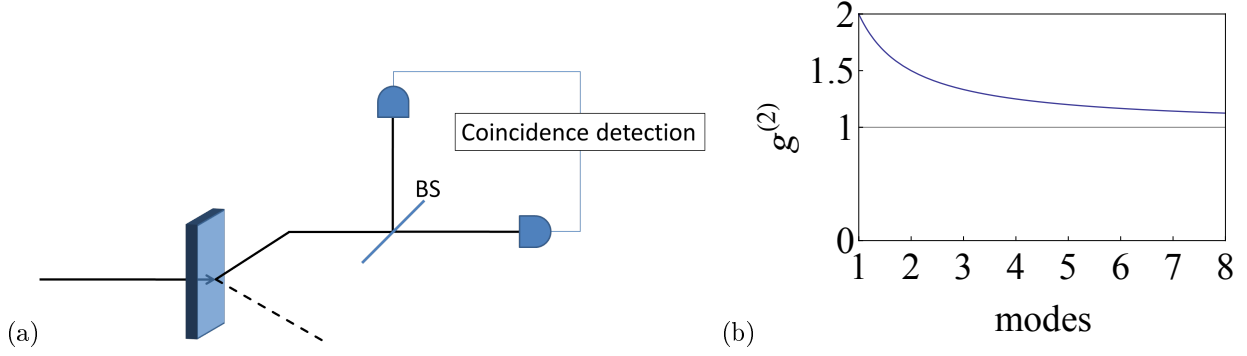


Figure 4.2: (a) Setup for measuring $g^{(2)}$ in one arm of SPDC using a Hanbury Brown-Twiss interferometer and (b) calculated relationship between $g^{(2)}$ for a source with K (effective) thermal modes.

the number of modes as $P = 1/K$. It's worth considering that we get this information from measuring only one arm of SPDC! This works because degenerate Type-I SPDC is invariant under the exchange of the signal and idler photons. This does not mean that the overall experiment is also invariant under this exchange, as the collection optics for the signal and idler arms could be collecting different sets of modes. For pair collection, as long as our collection is symmetric and we collect the same set of modes in each arm, this single-arm measurement is a valid characterization of the two-photon state. Additionally, unlike the previously described methods, this measurement is sensitive to the total number of independent modes, not just those that lead to intensity correlations (e.g., it also depends on pump temporal chirp which leads to phase correlations like those of Fig. 3.1).

This solves two important problems in our quest for characterizing an engineered SPDC source. First, we previously had no way of measuring correlations present in the joint spectral phase (see Fig. 3.1). Second, we knew such correlations could be caused by a temporally chirped pump, but we also had no convenient way to measure this chirp, as our pump wavelength is outside the range accommodated by typical autocorrelation techniques (see Appendix A). The $g^{(2)}$ measurement is sensitive to these phase correlations, and thus indirectly also describes the degree of temporal chirp in the pump. Fig. 4.3 shows the results of applying this technique to optimize dispersion compensation in the pump. With optimal dispersion compensation, we measure $g^{(2)} = 1.66 \pm 0.02$ without spectral filtering, and $g^{(2)} = 2.02 \pm 0.04$ with a 20-nm bandwidth filter. The exact nature of the reduction in $g^{(2)}$ seen in the absence of filtering is not known, but is likely due to higher-order dispersion in the pump. A model based on second- and third-order dispersion in the pump is shown in Fig. 4.3, but this does not completely account for the effect observed.

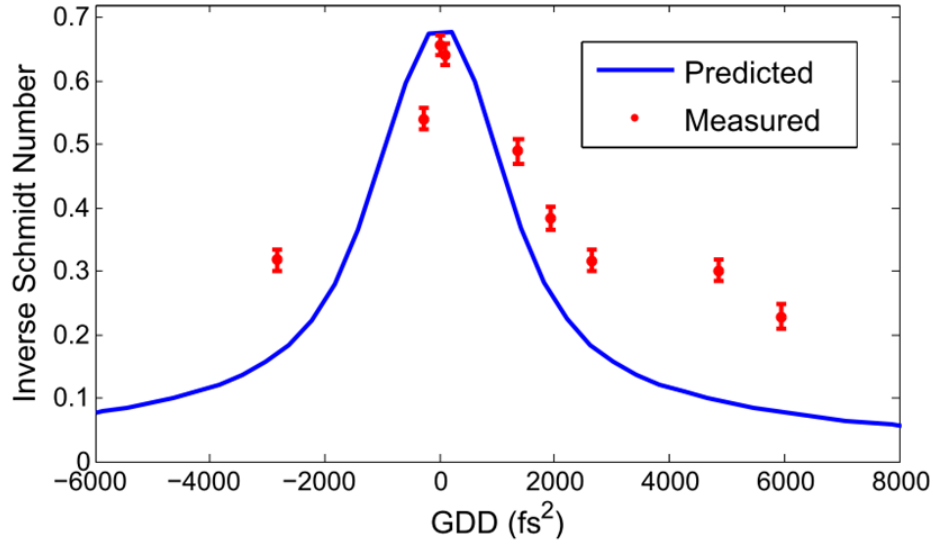


Figure 4.3: Values of inverse Schmidt number $1/K$, measured from the correlation function. This is equal to heralded single-photon purity or $g^{(2)}(0) - 1$. The horizontal axis shows a variable amount of group delay dispersion (GDD) applied to our pump, controlling pump temporal chirp. The dispersion is controlled using a prism pair compressor as described in Sec. A.4, and the results are used to determine the optimal dispersion compensation. A simple prediction based only on second- and third-order dispersion, done in collaboration with Alfred U'Ren, is shown in blue.

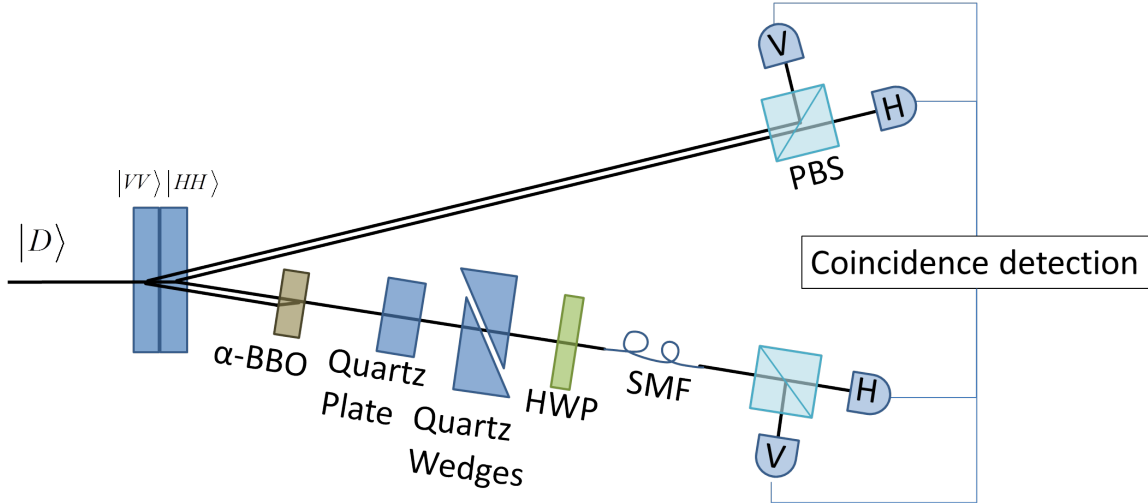


Figure 4.4: Two-crystal common-path HOM interferometer. A diagonally polarized beam pumps two crystals orthogonally oriented to produce vertical and horizontal photon pairs. In the signal arm, these distinguishable photons are directed to two detectors, heralding the presence of one photon pair from each crystal. In the idler arm, we use walk-off in birefringent α -BBO to combine the photons into a single spatial mode. The quartz plate and quartz wedges compensate for the temporal delay between the photons, which are coupled into a single-mode fiber and rotated into the diagonal/anti-diagonal basis. An HOM dip can be observed as a suppression of four-fold coincidence counts as the temporal compensation is adjusted.

4.2 Two-Source Hong-Ou-Mandel Interference

Ultimately, the usefulness of a pure state is in its ability to interfere with other indistinguishable pure states, potentially produced by arbitrary independent sources. In previous measurements, we indirectly inferred this property by characterizing the spectral modes produced by our source. However, a direct measurement is also possible, though considerably more resource-intensive. Recall from Sec. 1.1.2 that Hong-Ou-Mandel interference describes the reduction of coincidence counts observed due to interference between identical single photons on a beamsplitter (see Figs. 1.2 and 1.3). In a two-source HOM interferometer, these identical photons originated from independent sources, in our case the two sources are two orthogonal SPDC crystals. Our implementation of the two-source HOM interferometer is functionally equivalent to the schematic of Fig. 1.2(b), but the precise implementation details differ, as shown in Fig. 4.4. The most significant difference is that we employ a common-path polarization scheme with a similar motivation to the polarization interferometer of Sec. 3.2.3. Thus, rather than being distinguished by their spatial mode, the two sources in fact share the same spatial mode, but have orthogonal polarization modes. How then do we get HOM interference when the two photons arrive on the same beamsplitter input port? This is achieved by rotating the heralded photons into the D/A basis and using a polarizing beamsplitter in the H/V basis. Specifically, a half-wave plate takes $H \rightarrow D$ and $V \rightarrow A$, so our two-photon input state becomes

$$|H\rangle |V\rangle \xrightarrow{HWP} |D\rangle |A\rangle = (|H\rangle + |V\rangle)(|H\rangle - |V\rangle). \quad (4.15)$$

If two photons are identical, then the cross-terms cancel (because photons are bosons and symmetric under exchange), and we are left with a superposition of two horizontally- or vertically-polarized photons. These will then exit on the same port of a polarizing beamsplitter, giving the same HOM interference effect as Eq. 1.6. If the photons are partially distinguishable, recall from Sec. 1.1.2 that the HOM visibility V is related to heralded single-photon purity P through the density matrix ρ by

$$V = \text{tr} [\rho^2] \equiv P. \quad (4.16)$$

Another important implementation detail is the use of birefringent walk-off in α -BBO for spatial compensation in the idler arm, as described in to Sec. 2.3. As in the polarization-entanglement scheme, this removes which-crystal distinguishing information at the beamsplitter, allowing, in this case, two-source heralded single-photon interference.

The results of applying this measurement under different conditions are shown in Fig. 4.5. With no

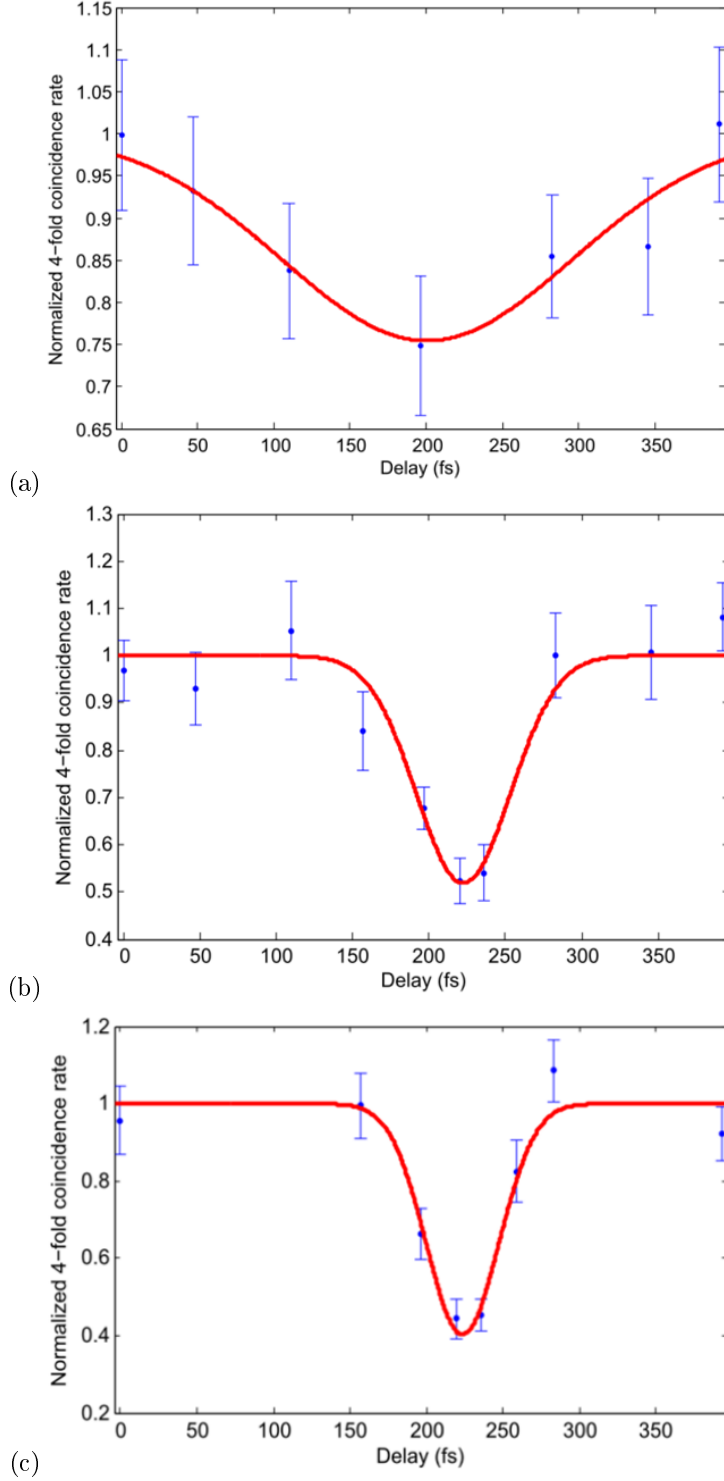


Figure 4.5: Results from two-source HOM with varying alignment and dispersion compensation. The visibilities of the HOM dips are (a) 0.24 ± 0.05 , (b) 0.48 ± 0.04 , and (c) 0.61 ± 0.05 . These show good agreement with accompanying $g^{(2)}$ measurements, which imply a maximum visibility of (a) 0.26 ± 0.02 and (b-c) 0.66 ± 0.02 . The low visibility in (a) is due to intentional misalignment of the dispersion compensation. The difference between (b) and (c) is due to imperfect collection mode matching in (b), which was improved to obtain the result in (c). This demonstrates how collection asymmetries can affect the two-source single-photon interference.

spectral filtering, we observe a maximum two-source HOM visibility of 0.61 ± 0.05 , which is consistent with the measured $g^{(2)}$ -implied purity of 0.65 ± 0.02 . Indeed, the $g^{(2)}$ -implied purity is an upper limit on the HOM visibility, as the HOM visibility is sensitive not just to the heralded single photons being in a pure state, but also being in the *same* pure state. That we are essentially able to reach this limit serves as an important confirmation between the information provided by these two measurements. Importantly, it validates the use of the correlation function measurement as a useful proxy for heralded single-photon purity. This is useful because, although the two-source HOM measurement provides unambiguous evidence for a lower bound on heralded single-photon purity, it is extremely time intensive. Each point on Fig. 4.5 requires several hours of photon counting due to the low rate of two-pair events, leading to a full day or more of data collection to obtain the HOM visibility. The correlation function measurement, on the other hand, can be performed on our source in under an hour.

Chapter 5

Detector Operation and Characterization

Astonishing True Tales of Quantum Light

Alternate dissertation title, comic book edition

The ability to reliably detect single photons is assumed as part of most optical quantum information protocols, and though this can be done quite well, there remains room for improvement. As discussed in Sec. 1.2, some schemes (including linear optical quantum computing and loophole-free tests of nonlocality) require extremely high system detection efficiency thresholds of 66-83% [2, 8, 63].

The efficiency of single-photon detection can be framed as a decision problem: given a pulse which may or may not contain a single photon, incident on some experimental apparatus, can the researcher correctly state whether or not a photon was present? This includes the possibility of both false negatives (failing to detect a photon), and false positives (indicating a photon when none is actually present). In the literature, the former is defined by the quantum efficiency¹ (QE), which is $1 - \beta$ for a false negative rate β . The latter is characterized by the dark count rate (assuming all background light has been eliminated), which is intrinsic to the device, and typically does not scale with the number of trials.

In a digital age, detection ultimately involves recording electronically whether the photon was present.² This is done most directly by optically exciting electrons, for example in a photodiode. However, the energy of a single photon of visible light is on the order of 10^{-19} joules, far too small to directly measure or even amplify with transistor-based devices. Instead, efficient single-photon detection relies on an avalanche gain process, for example in a photomultiplier tube (PMT) or avalanche photodiode (APD). Although the photon will only liberate a single electron, that electron can in turn excite additional electrons, leading to exponential gain. This is facilitated by the application of a bias voltage, which accelerates free electrons and supplies the necessary energy for additional impact-ionization events.

¹Confusingly, quantum efficiency is also sometimes conflated with quantum yield as $N_{\text{electrons}}/N_{\text{photons}}$ or incorrectly defined as $N_{\text{counts}}/N_{\text{photons}}$, which can be greater than 1 due to secondary emission or dark counts respectively. In this work, we always take QE to mean the detection efficiency—the conditional probability of a detector count at time t given the presence of an incident photon at time t , $\eta = P(\text{count}, t | \text{photon}, t)$.

²Of course, there can be an intermediary. For example, current research in our group is being done by Rebecca Holmes to determine whether human observers can see single photons.

PMTs and APDs are the best available off-the-shelf single-photon detectors, but are limited in QE to about 40% and 70% respectively [28]. Better-performing detectors are a subject of very active ongoing research [64, 65] (see Sec. 1.2), but here we focus on our work with one specific promising device, the visible light photon counter (VLPC). The VLPC was originally developed for high-energy applications at Fermilab; the device history is briefly discussed at the beginning of Chapter 6. As we will see, the VLPC has compelling advantages for quantum optics: it has a near-perfect intrinsic quantum efficiency ($95 \pm 5\%$), fast, low-jitter, response (approximately 250 ps jitter), photon number resolving capability, and a reasonable dark count rate (approximately 10 kHz per mm^2 detector area) [35–39]. We will also encounter its disadvantages: it requires cryogenic cooling to approximately 7 K, saturates at a relatively low count rate, is sensitive to background room-temperature blackbody radiation up to $25 \mu\text{m}$, and produces fast, difficult-to-detect signals (approximately 1-ns pulses of $150 \mu\text{V}$). This chapter discusses the basic operating principles of the VLPC and our cryogenic system for detector operation, while Chapter 6 describes the efficiency optimizations we undertook to achieve a high QE, as well as potential future improvements.

5.1 VLPC Operation

From top to bottom, as shown in Figure 5.2, the VLPC consists of an intrinsic silicon layer, an arsenic-doped gain layer, and a heavily doped substrate/contact layer [66]. Additionally, an anti-reflection coating and transparent electrical contact are located on top of the device. The electrical contact is used to apply a bias voltage of approximately 7 volts across the device. Thus, when a photon is absorbed in either the intrinsic layer or the gain layer, the freed electron is accelerated towards the top contact, while the corresponding hole is accelerated towards the substrate. In the gain layer, the hole impact ionizes an arsenic atom; only 54 meV is required to excite an electron into the conduction band. The electron in turn causes impact ionization of additional arsenic atoms, resulting in avalanche gain. The ionization of arsenic atoms is an important feature because the resulting holes are left in the arsenic impurity band, rather than in the intrinsic valence band. The As-doping concentration is chosen such that holes can travel between nearby arsenic atoms via conduction hopping (tunneling), creating a slowly drifting cloud of positive charge that accumulates with each additional electron-hole excitation, and limits and localizes the avalanche. This effect is central to the behavior of the VLPC, and leads to two desirable properties and one undesirable property, which must be balanced against each other.

For the layer thicknesses and doping concentrations in a typical VLPC, the avalanche is localized to a filament of $\sim 12 \mu\text{m}^2$, which is much smaller than the detector area of $\sim 1 \text{ mm}^2$ [67, 68]. This property is

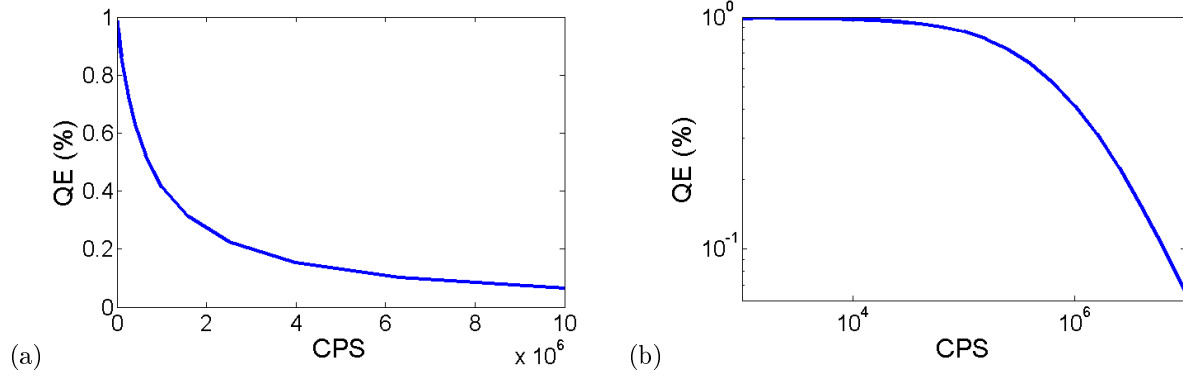


Figure 5.1: Simulated reduction in count rate for VLPC detectors assuming a 300-μm beam waist, 1-mm detector area, 15-μm filament radius, and 650-μs filament recovery time. Quantum efficiency versus count rate is shown on (a) linear and (b) logarithmic axes.

the source of the photon-number-resolving capabilities of the VLPC, as a single device has $\sim 10^5$ locations which can absorb a photon. Provided that N photons hit the detector at different physical locations—a safe assumption for $N \ll 10^5$ if the beam is spread evenly over the detector area—the resulting signal will be proportional to N . This also means that, when operating at low counting rates, the VLPC has effectively no dead-time. Instead, the expected quantum efficiency of the device decreases as an increasing count rate gradually saturates the device, shown in Fig. 5.1 and further discussed in Sec. 6.3.

An additional benefit of the self-limiting avalanche is that it leads to a very consistent multiplication gain. This can be quantified by the excess noise factor (ENF), defined as

$$ENF = \frac{\langle M^2 \rangle}{\langle M \rangle^2}, \quad (5.1)$$

where M is the number of charge carriers generated in each detection event. The greater the excess noise, the less reliably photon number can be inferred from the number of carriers observed, with the maximum number of resolved photons given by $N = (ENF - 1)^{-1}$. VLPCs have an ENF of 1.03, compared to 2 and 1.2 for APDs and PMTs respectively, implying a potential photon-number-resolution capability for the VLPC of up to 30 photons [38].

The above benefits come with a cost: the slowly relaxing holes limit the count rate of the VLPCs, as a new avalanche cannot be supported in the depleted region until the holes fully relax. This happens on a relatively slow millisecond timescale, exacerbating the saturation effect. Furthermore, the relatively small energy gap between the arsenic impurities and the conduction band causes technical challenges. First, at high temperatures, thermal effects can easily excite electrons from arsenic into the conduction band. This is avoided by operating the detectors at approximately 7 K, mostly freezing out the carriers. Similarly, this

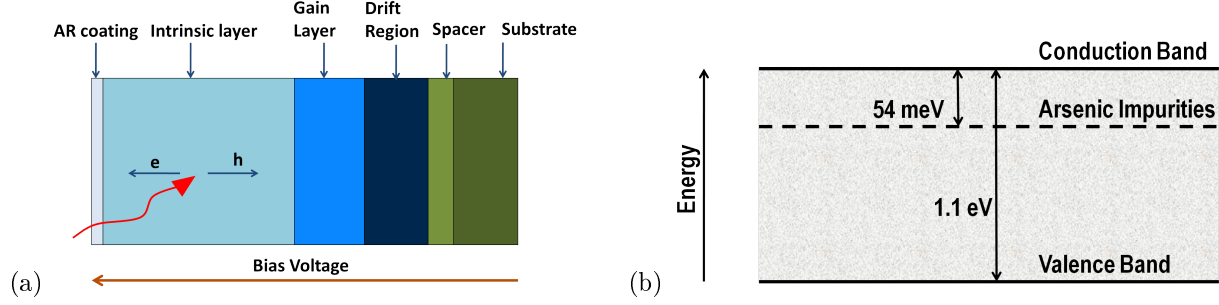


Figure 5.2: (a) Schematic diagram of VLPC device structure, and (b) the electron band structure of VLPC.

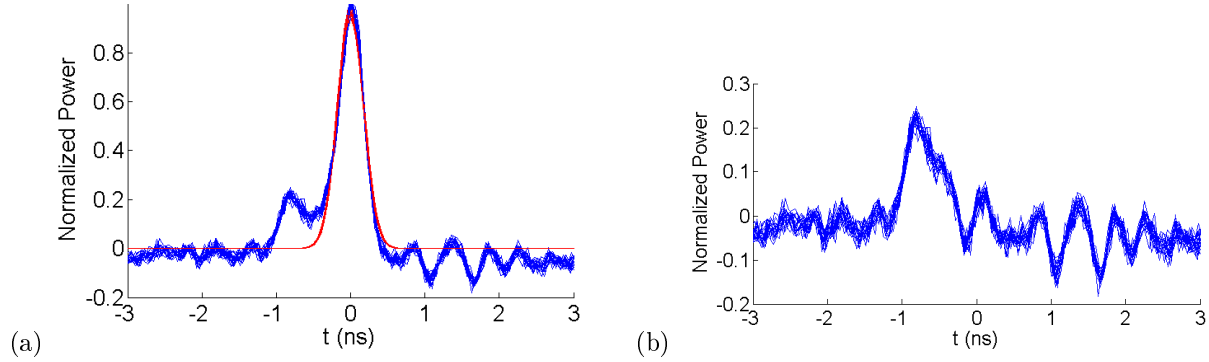


Figure 5.3: Jitter measurement of VLPC detectors showing (a) detector autocorrelation with Gaussian fit and (b) residuals with respect to the fit, using the measurement described in Sec. 3.3.1. The FWHM of the Gaussian fit corresponds to a 290 ps FWHM jitter, which agrees with other published data [39]. We speculate that the appearance of the secondary peak may be due to optical reflections or absorption of the photon in the gain/drift layer of the VLPC rather than the intrinsic silicon layer.

gap makes the detectors partially sensitive to infrared blackbody photons up to approximately $25 \mu\text{m}$. Since such light is abundant at room temperature, any attempt to couple in visible light must carefully exclude such infrared photons, or else become dominated by background counts.

5.2 Measurement Apparatus

We have tested two distinct systems for cooling the detectors to their operating temperature while blocking thermal radiation and allowing coupling of desired light: a helium cryostat and a liquid helium dunking probe. The cryostat has the advantage of being a self-contained system, needing only an input of liquid helium. However, it also has the disadvantage of having limited cooling power, leading to difficulty with increased dark counts. The dunking probe is a simpler system which cools the VLPC by inserting the probe directly into a helium dewar, but it has the disadvantage of requiring 1.5-m of fiber optic cable, which leads to more difficulty in efficiently coupling in light. Solutions to this problem are discussed in Sec. 6.2. The

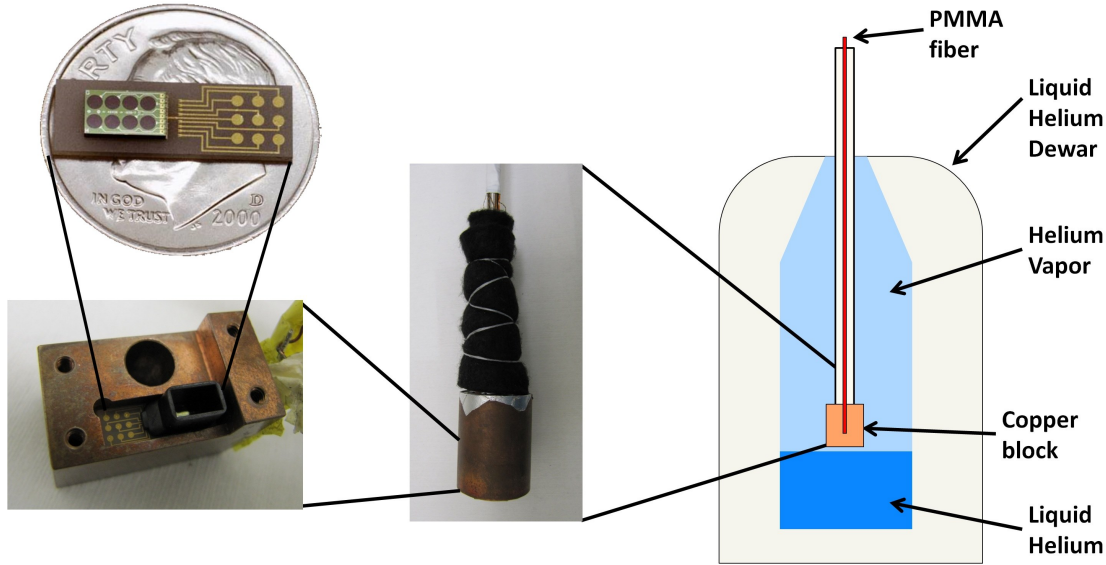


Figure 5.4: Dunking probe system for operating the VLPC. The detector is placed in a copper block and surrounded by a copper radiation shield. The VLPC is shown with 8 detectors mounted on a chip and wire-bonded to gold contact pads. Push pins (not shown) are used to make contact with these pads. PMMA (or glass, see Sec. 6.2) fiber couples visible light into one of the detectors, while blocking thermal radiation. This assembly is lowered into a liquid helium dewar, with the height above the liquid helium used to control temperature, and fine-tuning obtained by a heating element and temperature sensor connected to a temperature controller.

measurements discussed in this work were performed with the dunking probe setup, as shown in Figure 5.4. Other measurement systems are detailed in Chapter 7 of the dissertation of Radhika Rangarajan [15].

The dunking probe has several distinct parts which we will consider from bottom to top. A 60-liter liquid helium dewar³ forms the base of the apparatus, holding the liquid helium coolant and providing physical support to the rest of the assembly. The dewar also essentially forms a cold Faraday cage around the detectors, preventing RF noise and room-temperature thermal blackbody radiation from reaching them. Inside the dewar, the copper block shown in Fig. 5.5 is held just above the liquid helium. The copper block consists of a detachable base and top, fixed together by four 2-56 brass screws. The copper block base has recessed holes which contain a Lakeshore DT-470-LR low-temperature diode and 50- Ω resistive heater. These are used to regulate the device temperature via a PID loop controlled by a Lakeshore Model 331 Temperature Controller. The base also has a 3-mm recessed rectangular hole which holds the VLPC chip. A *thin* layer of Apiezon N thermal contact grease is applied to the bottom of the VLPC, as well as around the heater and temperature sensor.

The copper block top holds a set of 9 Everett Charles Tech A-S-R pins which make contact with the

³Though the helium dewars are theoretically identical and interchangeable, we have noticed some variation in performance between dewars, particularly in terms of the typical background count rate. Consistently lower background counts were observed with UIUC Physics Helium Facility dewar 50-11.

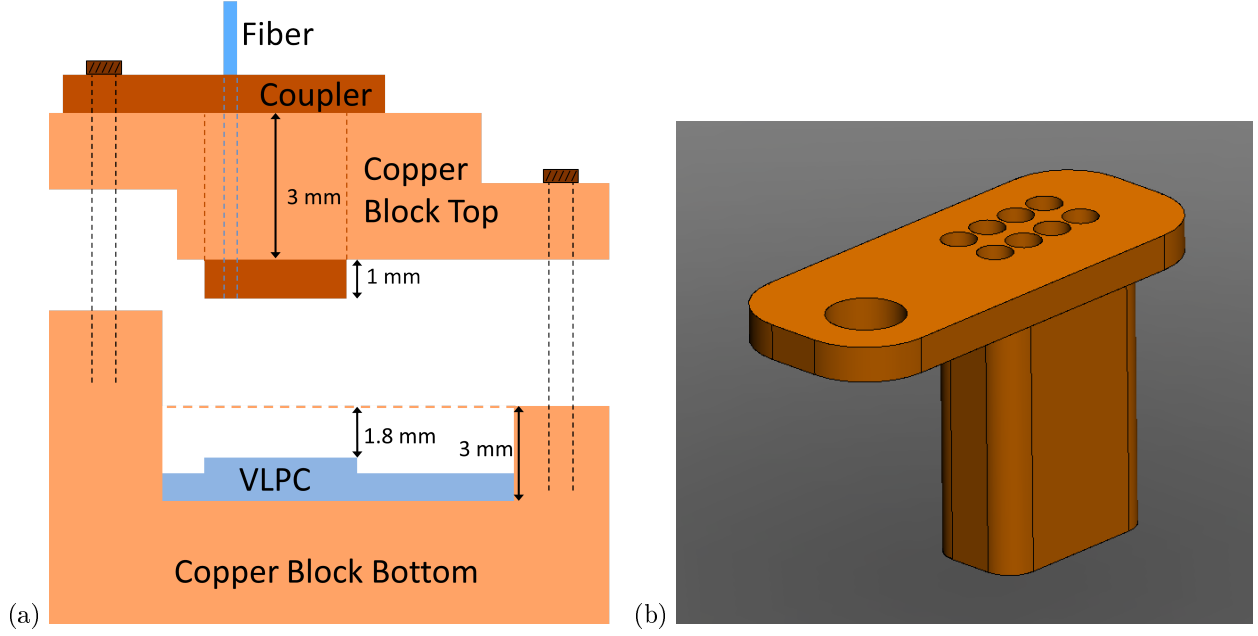


Figure 5.5: (a) Detailed cross-section view of copper block assembly from Fig. 5.4, with some relevant dimensions indicated (not to scale). (b) Rendered CAD drawing of fiber coupler (brass). Eight 1-mm diameter holes are aligned to position fibers relative to the eight detectors of the VLPC chip.

bias and detector contact pads on the VLPC chip. The copper block top also has a hole directly above the VLPC detectors, originally to allow pass-through of the 1-mm PMMA fibers held directly against the detector surface by a plastic connector “boot”, part of the original Fermilab design. Our current VLPC system iteration includes a brass fiber coupler which fits precisely in this hole, and has eight 1-mm diameter holes positioned directly above the detectors.⁴ Around the copper block, a copper radiation shield provides some thermal blockbody shielding as well as physical protection to the delicate wiring.⁵

A 1/4” hole is drilled through the radiation shield and copper block, allowing a stainless steel support rod which holds the block and radiation shield in place. Twisted-pair wires connect to the push pins and run loosely coiled along the length of the steel rod, together with the optical fibers, as well as wires connecting to the heater and temperature sensor. A layer of teflon tape holds the wires and fiber in place against the rod, surrounded by a layer of black felt in two locations for light blocking. The felt is located directly above the radiation shield and higher on the rod where it meets the surrounding 3/8” diameter, 1-m-long stainless

⁴The design of this fiber coupler was a challenge due to the need to precisely position fibers relative to the VLPC in a system that could not be practically tested at room temperature. We initially used 3D printing / rapid prototyping to test many possible coupler dimensions to find the best fit, but the tolerances on these parts were too coarse and the material did not hold up to cryogenic temperature cycling.

⁵The radiation shield is not light-tight, and likely only provides minimal shielding. This could be improved in a future design to further reduce background counts.

steel tube.⁶ The tube begins approximately 5" above the radiation shield and provides additional physical support and radiation-blocking. A custom flange coupler connects the tube to the top of the helium dewar and allows the tube/rod assembly to be raised and lowered within the dewar.

On the top of the tube/rod assembly, a breakout box completes the Faraday cage and allows external coupling to the fiber optics, temperature sensor, heater, and detector output. Amplification of the VLPC signal is done inside of the breakout box, and the heater and temperature sensor D-sub connectors use 243A100y0X Conec filters to minimize RF coupling into the system. Signal amplification, readout electronics and photon counting with this device are discussed in Sec. 5.3. Detection efficiency measurements were also performed on the dunking probe setup, yielding an overall system efficiency of $91 \pm 3\%$. Chapter 6 discusses efficiency optimizations that were employed to achieve this result.

5.3 Photon Counting

A technical hurdle arises from the electronic characteristics of the fast, low-amplitude signal pulses produced by the VLPC. We use a Miteq Au-1525 300-MHz amplifier with a gain of 60 dB to amplify the detector signal for our readout electronics. After this amplifier, the signal we observe from a single-photon detection event has a pulse height of approximately 150 mV⁷ and a FWHM of 1.5 ns. The high degree of amplification means that our system is especially sensitive to pickup noise in the twisted pair wires connecting to the detectors. This noise primarily enters into the system in two ways: either by incomplete shielding on the cryostat/dunking probe or by entering through the heater/temperature sensor wires and then coupling to the detectors. We counter the first problem by ensuring that the exterior of the system is a well-grounded Faraday cage, and the second by applying low pass filters to the heater and temperature controller wires.

5.3.1 Pulse Height Analysis

The amplified pulse is fed into a custom-built four-channel analyzer (FCA), necessary because of the extremely fast VLPC signal pulses [69]. The FCA uses digital potentiometers to set reference voltages against which the height of the input pulse is compared. The potentiometers define four voltage ranges, corresponding to four output channels on the FCA. When an input pulse is detected in one of these voltage ranges,

⁶This tube was an addition to the original system design, which suffered severely from RF pickup that could only be mitigated by excessive application of aluminum foil, and even this did not always help. The tube contributes to a much more consistent Faraday cage around the detector assembly.

⁷Pulse height depends on many variables. It increases with bias voltage and temperature, decreases at high count rates, and exhibits random variation due to intrinsic multiplication gain and amplification noise. We have also observed significant chip-to-chip gain variation (though detectors on the same chip have similar intrinsic gain). This was a significant challenge during our VLPC system development, as most of the chips we had available to test happened to be "low-gain" devices which produced signals too small to resolve from background noise.

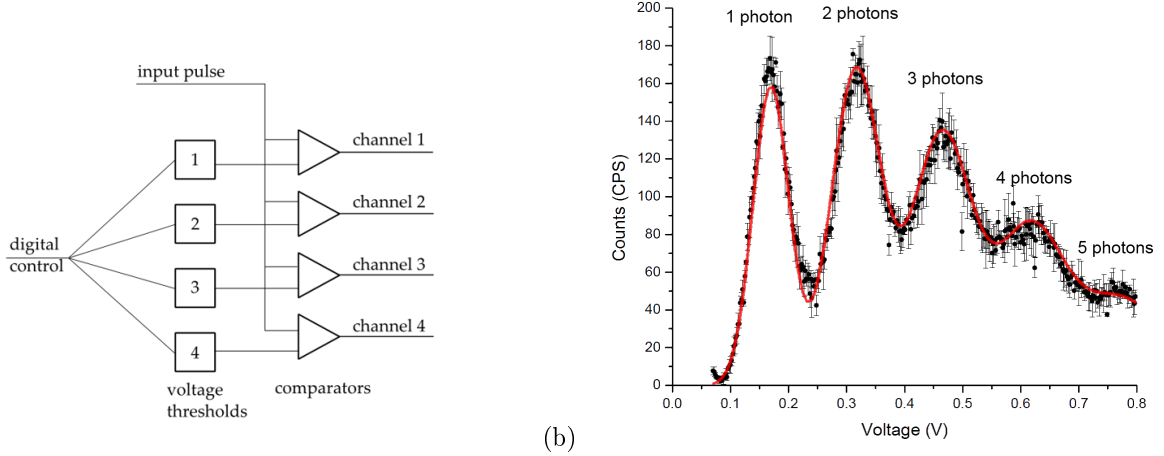


Figure 5.6: (a) Schematic of four-channel analyzer circuit used for pulse-height discrimination. Four digitally controlled potentiometers set voltage thresholds. If an input pulse exceeds the first threshold, a TTL pulse is produced on channel 1. Failing this, if it exceeds the second threshold, a TTL pulse is produced on channel 2, and so on. (b) Typical pulse height distribution plot showing multi-photon detection. The peaks correspond to laser pulses containing 1-5 detected photons.

an output TTL signal is produced on the corresponding channel. To test photon number resolution, we require a source which can deliver multiple photons within the detection time response of the VLPC. We use a Nd:YAG laser, frequency-doubled to 532 nm, and attenuated to the single-photon level. The laser outputs short pulses (approximately 600 ps) with a repetition rate of 40 kHz. The short pulse duration is essential for multi-photon detection because photons must arrive within an approximately 1-ns window to be registered as a single detection event. Gating with a photodiode is used to reduce dark counts by only allowing signals to be registered during a laser pulse.

As shown in Figure 5.6, we are able to detect 1-5 simultaneous photons. The plot is constructed by using the FCA to select a narrow voltage bin, and then counting all input pulses within that bin. By breaking up the desired voltage range into many such bins, a histogram of the pulse height distribution can be constructed. The small bin size of the FCA enables us to obtain a finely resolved picture of the pulse height distribution, facilitating comparison with theoretical predictions of the characteristics of the distribution. The center of each peak in the distribution corresponds to the mean peak height of a detection event from a laser pulse with a given number of photons. The first peak at about 170 mV is the typical height of a pulse produced by a single photon, the second peak at about 315 mV is the typical height for two simultaneous photons, and so on. The width of the peaks is determined by both the intrinsic noise of the VLPC and the electronic noise of the system.

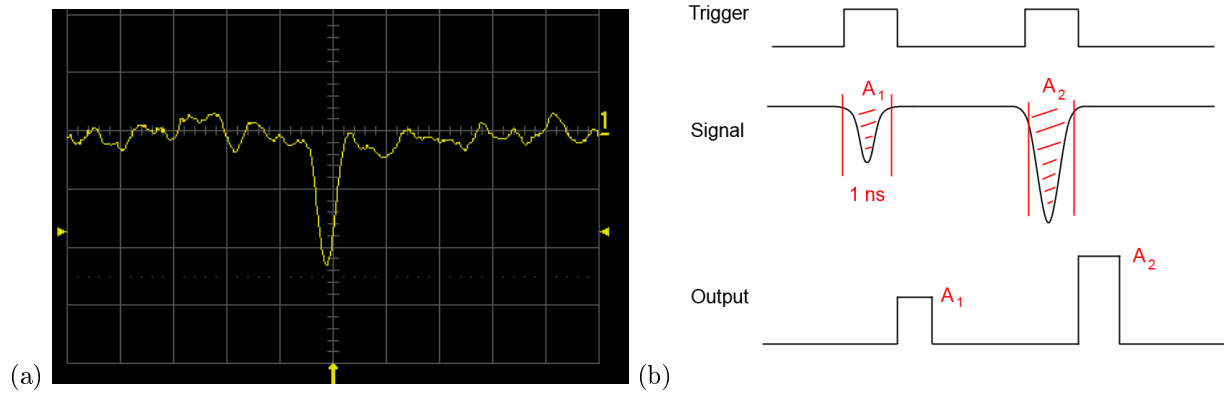


Figure 5.7: (a) Oscilloscope trace of a typical VLPC single-photon detection event. The vertical scale is 100 mV per division and the horizontal scale is 5 ns per division. The peak height is approximately 220 mV. (b) Desired behavior of a proposed pulse area analysis circuit. The ideal circuit should integrate the signal over a triggered, approximately 1-ns window, and output either an analog pulse with amplitude corresponding to the integral of the input signal, or a digital value corresponding to the discretely-sampled integral.

5.3.2 Photon Number Resolution

Figure 5.6 also shows a curve fit consisting of a sum of Gaussian peaks, constructed with all available theoretical constraints. The area of each peak is determined from a Poisson distribution with $n_{avg} = 2.8$. Ideally, the center of each peak would be located at an integer multiple of the first peak. However, the estimated 600-ps duration of laser pulses is a sizable fraction of the 1-ns VLPC pulse width. Therefore, when two photons arrive at the detector slightly offset in time, the resulting pulse is slightly shorter and broader than when they arrive simultaneously, causing peaks beyond the first to be at a lower voltage than expected. This effect is significant, reducing the second peak to 93% of its expected value. A calculation of this shift is included in the fit in Fig. 5.6. This effect can be eliminated by using either a faster source (pulses on the order of 100 ps or shorter⁸), or using detection electronics that respond to pulse area rather than pulse height (see Sec. 5.3.3).

5.3.3 Pulse Area Analysis

Our current system triggers on the pulse height of the VLPC signal, but this is not ideal for several reasons. First, if using photon-number resolved triggering, it requires calibration to set the discrimination thresholds between photon numbers: a pulse height distribution like that of Fig. 5.6 must be measured to determine the ideal location of the thresholds. This distribution must be remeasured if the temperature, bias voltage,

⁸We have short-pulse VCSEL laser diode circuit provided by Dan Gauthier which emits 130-ps pulses and should be sufficient for this purpose.

or average count rate of the VLPC changes, and a measurement requires about 30-60 minutes. Second, pulse height analysis is compromised by the possibility of multiple pulses arriving slightly offset in time. Third, the accuracy of the voltage threshold comparison limits the accuracy of the measurement, having an error of approximately 10 mV.

Rather than an analyzer with a binary response of triggering or not triggering based on pulse height either exceeding or not exceeding a threshold, we could employ an integrator which measures the total charge of an input pulse (see Fig. 5.7). This is a much more direct measurement, since the VLPC is intrinsically a charge-based rather than voltage-based device. It is insensitive to pulses arriving slightly offset in time, as the total charge is constant regardless of the time offset. Finally, measuring the area of a pulse rather than whether or not it exceeded a pre-set threshold provides much more information about each pulse. This allows much faster construction of the pulse-height distribution as it is no longer necessary to individually measure each bin independently.

Simple and inexpensive FPGA-based digitizing circuits are readily available, but tend to be limited to rates on the order of 0.1-1 samples per nanosecond, which is not sufficient for our signals. To maintain reasonable fidelity with the VLPC signal, we would require a minimum sampling rate of approximately 3-5 samples in a 1-ns period. However, though the speeds required prevent a simple solution, the problem is certainly not beyond modern semiconductor technology. High-speed signal sampling and digitization is routinely done at even higher rates⁹ in conventional digital oscilloscopes. Thus, a commercially available digitizer/oscilloscope (such as the NI PXI-5153 digitizer module) could provide a feasible, though expensive, solution. Instead, we could design and fabricate an application-specific sample-and-hold integrator circuit [70].

⁹Analog bandwidths of 1 GHz or higher and sample rates of over 10 gigasamples per second (GS/s) are common among high-end oscilloscopes, and even sampling above 100 GS/s is available. 10 GS/s corresponds to 10 samples in a 1 ns period, easily sufficient for our needs.

Chapter 6

Detector Optimization

The worst enemy of life, freedom and the common decencies is total anarchy; their second worst enemy is total efficiency.

Aldous Huxley

The historical context of the VLPC has important implications for optimizing its properties. The VLPC was based on a previous detector, the Solid State Photomultiplier (SSPM), developed by Rockwell International¹ and originally used by Fermilab as a detector for fiber scintillators [71]. The VLPC was developed by Rockwell as a visible-light-optimized version of the infrared-sensitive SSPM, designed to have an optimized QE near 550 nm and to operate at higher count rates, with superior time resolution and with reduced sensitivity to IR photons than the SSPM [72]. This was achieved partially by eliminating a heavily doped layer (located beyond the gain layer) which was responsible for absorbing IR photons in the SSPM, and replacing it with the smaller spacer region of Fig. 5.2. [73]. Around the same time, the growing field of quantum optics was in search of high-QE detectors, based on the theoretical concerns motivated in Sec. 1.2. It was found that the SSPM (and its successor, the VLPC) had potentially nearly ideal properties for implementing previously theorized quantum information schemes [74].

However, the fact that these detectors were originally designed for use in high-energy experiments leads to some mismatch of performance characteristics when adapting the VLPC for use with optical quantum information. In particular, high quantum efficiency was only one desirable property for the original high-energy application, while it is often absolutely critical for quantum information. Achieving the highest possible QE is a significant practical challenge. Even if the intrinsic QE of the detector is 100%, it is not trivial to ensure that every photon one wishes to detect actually reaches the device rather than being lost or reflected along the way. Additionally, if not avoided, saturation effects can easily lead to reduced QE. This chapter describes our work in optimizing VLPC performance at 710 nm, a wavelength chosen for compatibility with our Bell test experiments. Anyone attempting to work with VLPCs in the high-QE limit

¹Rockwell was acquired by Boeing in 1996, and later sold to DRS Technologies in 2001. DRS was acquired by—and operates as a wholly owned subsidiary of—Finmeccanica as of 2008.

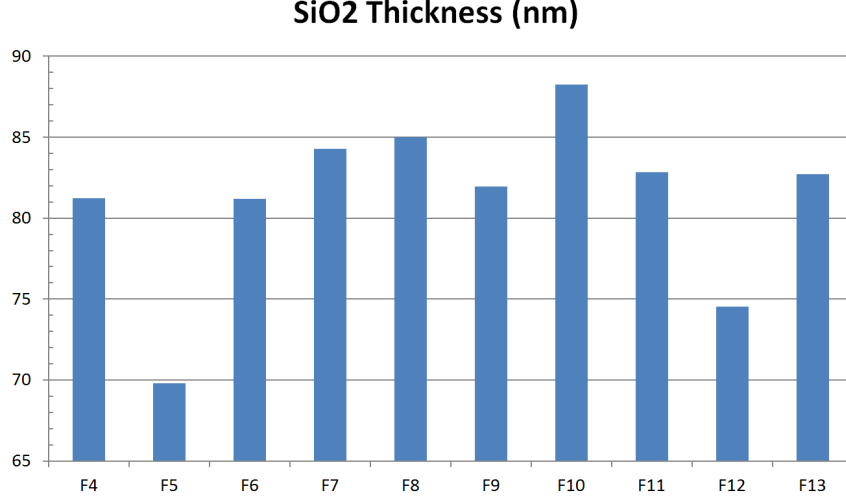


Figure 6.1: Thickness of SiO₂ layer for a selection of VLPC chips, measured with Woollam VASE ellipsometer. Due to significant chip-to-chip variation in SiO₂ thickness, it is critical to carefully measure this layer before applying anti-reflection coating.

may especially wish to consult Table 6.1, which details many problems that can lead to sub-optimal detector performance and describes how these problems can be diagnosed and remedied.

6.1 Anti-reflection Coating

The original VLPC design has a silicon-dioxide layer grown on top of the silicon chip. This acts as a single-layer AR coating designed to minimize reflection near the design wavelength of 550 nm, but leads to a Fresnel reflection of 12% at our desired wavelength of 710 nm. We independently measured the silicon-dioxide layer with a Woollam VASE ellipsometer, and saw significant variation of coating thickness between different chips (see Fig. 6.1). This variation must be accounted for if a new AR coating layer is to be applied on top of the existing layer.

Previous efforts to coat the VLPCs in-house with a plasma-enhanced chemical vapor deposition technique lead to peeling of the newly-applied coating under stresses induced by thermal cycling [15]. Instead, we had our detectors coated independently by two companies: Evaporated Coatings, Inc. (ECI) and Institut National d’Optique (INO). INO used reactive low-voltage ion plating, a stress-free coating process, while ECI used a proprietary coating method which they specified as being able to withstand our operating conditions. The resulting coatings both exhibited less than 0.1% reflection at the design wavelength, and showed no signs of de-adhesion after 30 cycles of cooling to 7 K and warming to room temperature. Ellipsometer reflectivity measurements for an uncoated VLPC and the custom-coated devices are shown in Fig. 6.2.

Problem	Diagnosis	Cause	Solution
High background counts	Counts vanish when light source is turned off.	Insufficient attenuation of light source	Make sure light source is properly attenuated
	Counts persist when VLPC bias voltage is removed; oscilloscope shows transitory oscillating signal or high amplitude white noise.	Electronic pickup noise	Improve shielding / grounding / electronic isolation
	Note current bias voltage, then turn off bias. Gradually increase bias voltage back to previous level. A large discontinuous jump in count rate is seen above a threshold bias voltage.	Breakdown voltage exceeded	Operate bias below breakdown voltage
	Decrease VLPC temperature until background count level is reasonable. Negligible reduction in quantum efficiency is observed.	VLPCs too warm	Operate VLPC at a lower temperature
No counts	[None of the above]	Thermal blackbody leak	Improve low-temperature radiation shielding
	Oscilloscope shows VLPC peaks.	FCA malfunction	Check FCA connection cables, power-cycle FCA
	Increase temperature and bias voltage of VLPC until counts are seen (do not exceed 8V / 9K). With VLPC disconnected from amplifier, check for low resistance between detector and bias. This should be above 20 M Ω at 7K, and 40-100 Ω at room temperature.	Bias/temperature too low	Operate at higher bias / temperature
	At room temperature, with VLPC disconnected from amplifier, check for high resistance between detector and bias. This should not be over 100 Ω .	Electrical short	Find and fix short
Low quantum efficiency	Increase temperature and/or bias voltage of VLPC, but do not exceed breakdown voltage.	Electrical break	Find and fix break
	Background count rate with light source off exceeds 100 kHz.	Bias/temperature too low	Operate at higher bias / temperature
	Total count rate with light source on exceeds 100 kHz	Saturation due to high background	Reduce background counts (see above)
	Check for cross-talk onto physically adjacent detectors on VLPC chip.	Saturation due to high photon flux	Increase attenuation of light source
	Check for low fiber transmission at room temperature.	Poor fiber alignment	Adjust relative transverse and/or longitudinal position of fiber relative to VLPC
	Check VLPC reflectivity at room temperature.	Damaged fiber or fiber AR coating	Replace fiber
	[None of the above]	Damaged VLPC AR coating	Use chip with proper AR coating
		Poor intrinsic VLPC efficiency	Try different VLPC chips

Table 6.1: Common problems and solutions for VLPC detector operation.

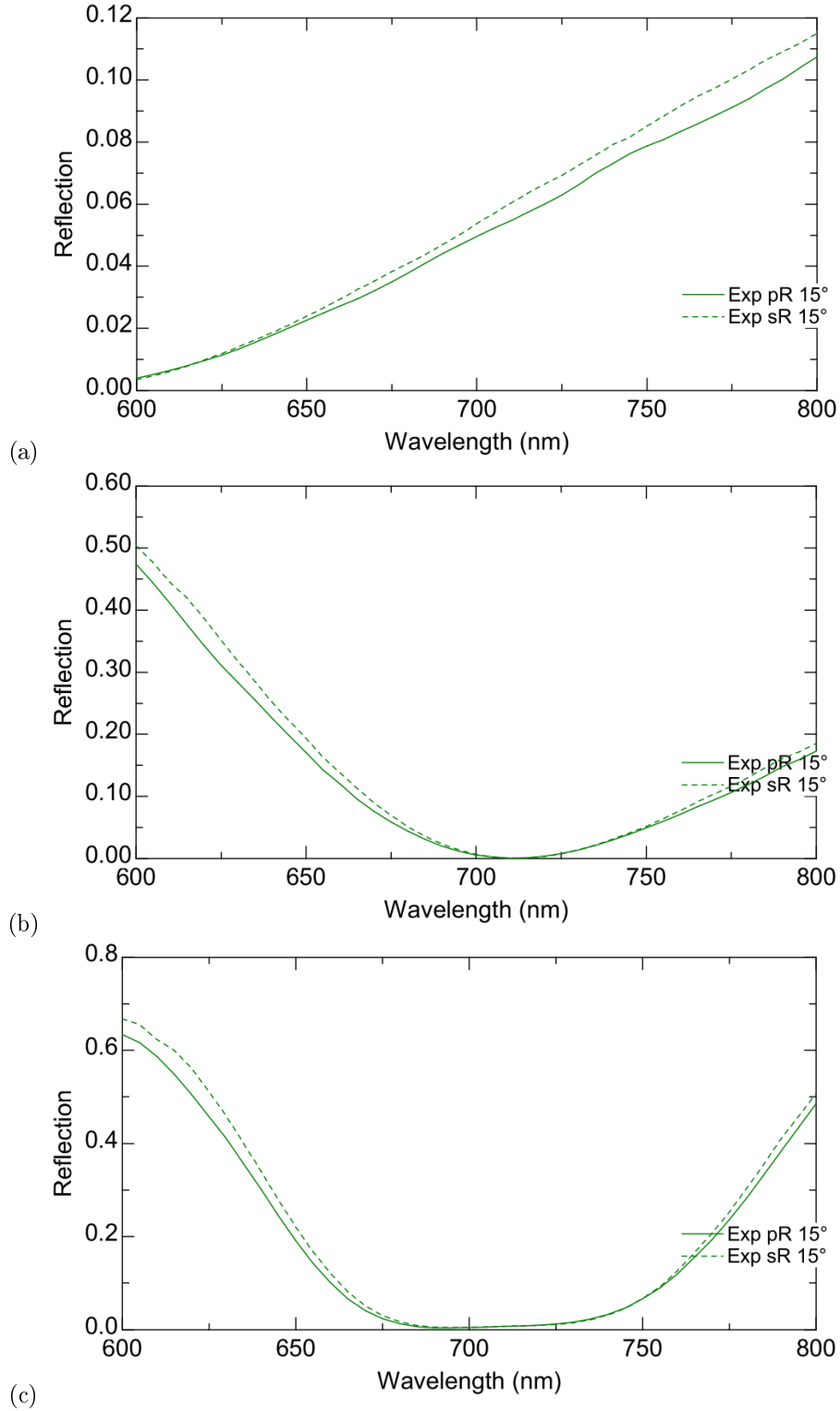


Figure 6.2: Ellipsometer measurements of reflectivity (reflected power divided by incident power) as a function of wavelength for (a) uncoated VLPC, (b) VLPC with coating by Evaporated Coatings, Inc (ECI), (c) VLPC with coating by Institut National d'Optique (INO). Due to ellipsometer geometry, reflectivity measurements are made 15° off of normal incidence. Also, the ellipsometer is not a precisely calibrated tool for absolute reflectivity measurements, so the vertical scale on these measurements should not be viewed as definitive.

6.2 Fiber selection

From an efficiency perspective, the optical fibers are perhaps the most important component of the VLPC system, other than the detectors themselves. First, if fibers capable of transmitting room-temperature blackbody radiation are used, the VLPCs will be overwhelmed by background counts. Second, reflection and absorption losses in the fiber will prevent some photons from being transmitted to the detectors. Third, if the fibers are not well-positioned with respect to the VLPC detectors, the transmitted photons may not have a chance to be detected.

The first problem prohibits the use of what would otherwise be the most versatile and desirable type of optical fiber: multimode glass fiber. The large, 62.5- μm core of this fiber easily supports transmission of far-IR light. Instead, we can use standard telecom SMF28e+ fiber, which has a core diameter of 8.2 μm and does not support transmission of far-IR light (cutoff wavelength is 3.5- μm). This fiber is slightly multimode at 710 nm, and we have successfully transmitted 710-nm light through telecom with near-perfect coupling. Single-mode fiber at the desired wavelength is also available, we have used Nufern 630-hp fiber, which is designed for a wavelength range of 600-770 nm and a core diameter of 3.5 μm . An alternative technique is to use plastic (PMMA) fibers, which are strongly absorbing in the infrared.

The second problem—reflection and absorption—is a major issue with the PMMA fibers. Although they are easy to couple into and provide good IR attenuation, they have a sizable attenuation in the visible spectrum, with a measured 85% transmission for 1.5 m of PMMA fiber at our test wavelength, including an expected 4% reflectivity at each interface. The interface reflectivity can be reduced by AR coating, but this is impractical on the cryogenic end of the fiber, as the large thermal expansion coefficient of plastic will ruin the coating. Further, the internal attenuation of PMMA cannot be avoided, except by using a shorter length of fiber.² For this reason, we switched from PMMA to glass fibers, which experience much less thermal contraction and thus are more practical to AR-coat. With AR coating from ECI, our glass fibers have a reflection of less than 0.1% at the design wavelength, and have demonstrated robustness after 10 rounds of 293 \leftrightarrow 7 K temperature cycling.

The third problem—fiber positioning—is one of the most vexing, as it is ultimately only accurately tested by operating the detectors in the full cryogenic system.³ Here, the PMMA fibers have an additional benefit of being compatible with the boot coupler design of the original Fermilab VLPCs. Our other fibers are

²A potential alternative is to use a combination of a long glass fiber and short piece of PMMA for IR attenuation, but the thermal contraction of the PMMA would still limit the practicality of AR coating, and thus the overall transmission.

³We employed various other tests, including precise position measurements with a microscope, and a photographic paper alignment method. In the latter, we replaced the VLPC with a plastic assembly holding a VLPC-sized piece of photographic paper, which we exposed with light from our positioned optical fibers. Developing the photographic paper and measuring the position of the exposed spot indicated the position and beam size illuminated by the fibers.

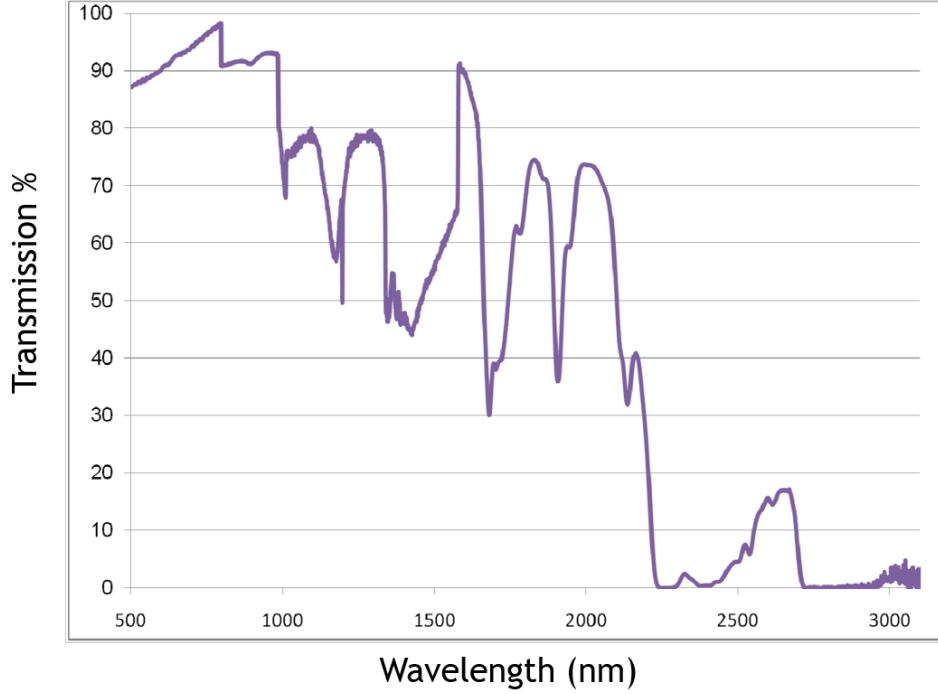


Figure 6.3: Transmission through 1.8 mm of PMMA fiber as a function of wavelength, corrected for Fresnel surface reflections, measured by Onur Hosten.

not compatible with this design, having an outer cladding diameter of $125\ \mu\text{m}$. This was a challenge for producing a custom fiber coupler as well. Ultimately, we found the best solution was a custom-machined brass coupler (see Fig. 5.5) with 1-mm diameter holes. We use JNS borosilicate glass ferrules with a 0.99-mm outer diameter and 0.126-mm inner diameter as an adapter between the fiber and brass coupler. Our initial fibers were hand-threaded through these ferrules after AR coating and fixed to the ferrule with GE varnish (VGE-7031). However, we found this could easily damage the AR coating, and future fibers were ordered from ECI attached to ferrules before AR coating.

6.3 Saturation Effects

While APDs are characterized by a dead-time during which they are blind to subsequent photons, VLPCs have essentially no dead-time when operated at low count rates. This occurs for the same reason as the PNR capability discussed in Chapter 5: localized avalanches mean that individual photon detection events are spatially isolated from each other. However, each detection event does leave a small spot on the detector “dead” for some time, and at high count rates, this will lead to saturation effects. In principle, one can determine the saturation rate through simple modeling based on two device parameters: the cross-section

area of the “filament” region depleted by a detection event, and the recovery time of that region. There is some debate in the literature about the correct values for these parameters (published values range from 15-micron-radius filaments with 2-microsecond dead-times to 2-micron-radius filaments with 3.5 millisecond dead-times [36, 67]). Moreover, these parameters may vary with temperature and bias voltage, and even from chip to chip (considerable gain variation has been observed between chips, so it is reasonable to expect that other device parameters may vary as well). For our investigation of saturation effects, we focused on a single detector on a single chip for consistency.

We have observed maximum count rates of approximately 10 MHz on some VLPCs, so we can roughly estimate saturation by comparing the filament radius to the 0.5-mm detector radius. noting that $10 \text{ MHz} = (0.5^2/0.015^2)/111 \text{ } \mu\text{s} = (0.5^2/0.002^2)/6.25 \text{ ms}$, suggesting a dead-time per filament on the order of 100 μs for 15-micron-radius filaments, or 6.25 ms for 2-micron-radius filaments.

To better understand the saturation rate of VLPCs, we took a series of saturation measurements (see Fig. 6.4) and conducted a detailed Monte Carlo simulation. Previous work treated the VLPC as an array of independent detectors to simplify the simulation, but there is no physical basis for this assumption. In fact, this misses an important effect: if an avalanche is initiated near a depleted region, it will receive less gain than an avalanche in a non-depleted region. Thus, we instead treat the VLPC as a continuous surface without subdividing it into a discrete array. We assume that each detected photon initiates an avalanche unless it strikes a region depleted by a previous avalanche. That region is marked as depleted until after a recovery time τ has passed. Detection events are recorded only if an avalanche with sufficient gain is observed (corresponding to an experimental 70-mV cutoff voltage).

Running our simulation iteratively with a simulated annealing optimization algorithm indicates that 15- μm filaments with a 650- μs recovery time accurately describe the tested VLPC when operating in a high-QE regime. However, it is difficult to decouple filament size and recovery time based on efficiency measurements alone, as similar results are obtained as long as the product of filament area and recovery time are constant.⁴ Thus, it would be more accurate to state that the product of filament area and recovery time consistent with our simulation and measurements is 460 $\mu\text{m}^2\text{-ms}$. It is also quite likely that this varies significantly between chips and operating conditions. In particular, saturation measurements suggest that devices operating with high quantum efficiency tend to saturate more quickly, as shown in Fig. 6.4. This seems reasonable, as both gain and QE increase with bias voltage, and one might expect that a higher gain might correspond to a larger filament radius and thus lower saturation point.

⁴In principle, one could determine filament size by focusing a test source onto an increasingly small detector spot. The saturation point should decrease proportional to the area of the illuminated spot as fewer independent filaments can be used, but this reduction would plateau once the spot size becomes smaller than the size of a single filament.

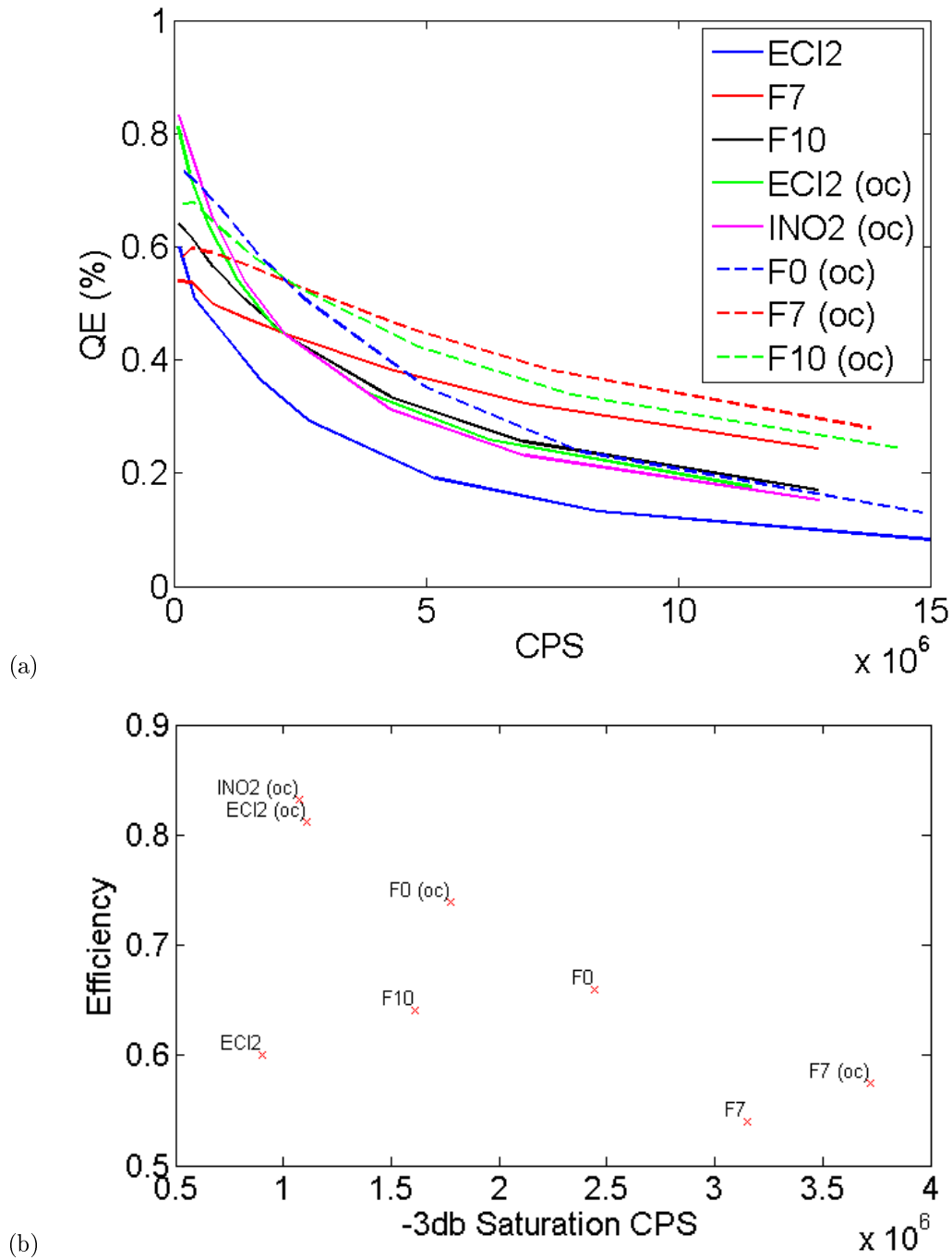


Figure 6.4: (a) Measured QE as a function of incident photon flux in counts per second. (b) Peak efficiency vs saturation observed for various detectors. Saturation is given as the count rate in counts per second at which a 3-dB reduction in efficiency is observed. Several factors affect peak efficiency: detectors INO2 and ECI2 are anti-reflection coated, while other detectors have a 12% Fresnel reflection. Additionally, two different fiber couplers were used; detectors marked (oc) use the optimized coupler.

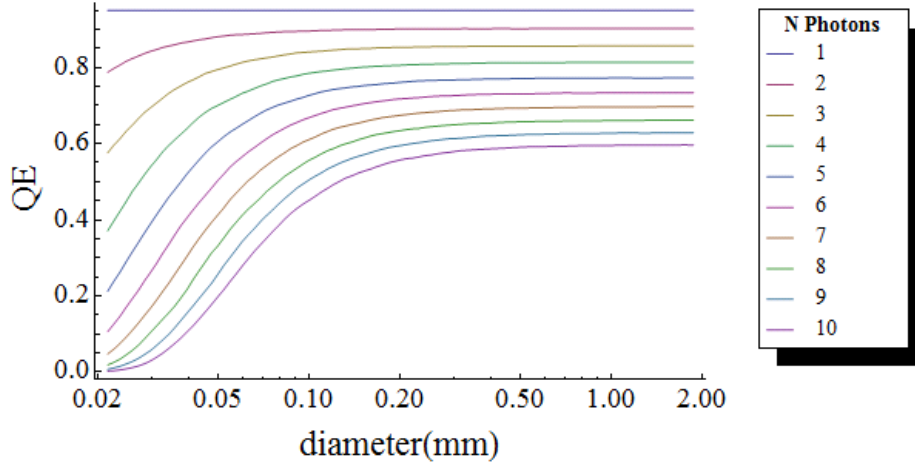


Figure 6.5: The calculated ideal probability of correctly identifying N input photons as a function of modeled detector diameter, assuming a 95% detection efficiency and a $12\text{-}\mu\text{m}$ square effective avalanche filament area. This is determined from a simulation of photons in a Gaussian beam hitting random locations on the detector surface. A successful N -photon detection event is recorded if all photons create an avalanche, and no two avalanches overlap.

6.4 Proposed Modifications

VLPCs were originally designed for high energy physics at Fermilab’s $D\bar{O}$ experiment rather than for quantum information applications. So, it is reasonable to suspect that further optimization is possible for our ideal criteria of fast response time, low dark counts, and high quantum efficiency at a variety of wavelengths of interest. In this section, we discuss some proposed modifications to improve these properties.

6.4.1 Detector Area

While increasing the efficiency of our system is a high priority, it would also be desirable to have detectors with a lower dark count rate. Dark counts are indistinguishable from true photon detection events, and thus skew photon detection results. Since the number of dark counts is proportional to the detector surface area, cutting the detector diameter by a factor of 10 should reduce dark counts by a factor of 100. An achievable dark count rate for the current 1-mm diameter detectors is around 10,000 counts per second, so by moving to $100\text{-}\mu\text{m}$ detectors (comparable in size to many commercially available APDs), we should be able to achieve a level of approximately 100 dark counts per second (lower than many commercially available APDs). However, there is a limit to how much reduction in size would be desirable. Each photon detection “uses up” a filament with radius of $2\text{--}15\text{ }\mu\text{m}$, so if two incident photons arrive with too little spatial separation, they will not both be able to trigger avalanche events. Thus, a possible concern is that by reducing the detector area, we will reduce our ability to detect multiple simultaneous photons. However, for a $100\text{-}\mu\text{m}$

detector, our calculation shows that the associated loss relative to a 1-mm diameter detector is negligible for two simultaneous photons and acceptable for higher numbers of simultaneous photons (see Fig. 6.5). It should also be noted that the saturation point is also reduced proportional to the area, potentially leading to measurable efficiency reduction for count rates on the order of a kilohertz. It may be possible to mitigate this if the carrier recovery time of the VLPC can be improved, but this requires additional research and detailed device modeling [75].

6.4.2 Wavelength Sensitivity

VLPCs are a visible-light-optimized version of the original SSPMs, but for some applications, a high QE detector for infrared or UV photons would be very desirable. Potential modifications to the VLPC to enhance sensitivity at other wavelengths of interest have been proposed [75]. The SSPM had a high QE for far-IR photons around 10-20 μm , but low efficiency for photons in the telecom band of 1-2 μm , due to the low absorption coefficient for this wavelength in both the intrinsic silicon layer and the arsenic-doped gain layer. However, an edge-illuminated design would allow photons to travel through a greatly increased thickness of silicon, allowing a much higher chance of absorption, with an expected detection efficiency of over 50% in the telecom region.

On the other end of the spectrum, the UV performance of the VLPC is limited because UV photons are absorbed in the top contact layer and do not lead to avalanche gain events. This could be eliminated by using advanced semiconductor growth or annealing techniques to create an ultra-thin contact layer of much less than 50 nm.

Chapter 7

Conclusions

Curious Properties of Light, Relating to the Joint Spectrum of Spontaneous Parametric Down-Conversion, and also Efficient Detectors of Single Photons, of Promising Application to the Field of Optical Quantum Information Processing

Alternate dissertation title, 1689 edition

Here we will try to briefly sum up the results of the work described in this dissertation, as well as discuss a few of the most promising future directions for related research. Finally, we will say a few words about how this work fits into the present and future of the field of quantum information.

7.1 Unentangled Source

Using a broad bandwidth pump laser and group velocity matching, we were able to generate entangled pairs of photons with a purity of 0.88 ± 0.02 with no spectral filtering, and a purity of 0.99 ± 0.01 with 20-nm filters. Downconversion-based entanglement sources not engineered for high purity typically use filters narrower than 1 nm to achieve the same result. In this respect, our source is a successful proof-of-principle: the group-velocity matching, broad-bandwidth approach can generate high-purity entanglement without narrow-band spectral filtering.

However, we also found that there is a trade-off between heralding efficiency and purity. Stronger correlations between SPDC photons can improve heralding efficiency, and after eliminating most of these correlations to achieve high purity, our heralding efficiency was limited to about 20%. This efficiency limits the usefulness of our source in applications where heralding efficiency is crucial, such as an on-demand single-photon source.

Recently, waveguide sources [76] and telecom-wavelength sources [77] have shown promising results, achieving higher count rates for similar purity, with higher heralding efficiency. (One advantage of a telecom source is that group velocity matching at these wavelengths occurs naturally in a co-linear downconversion source, eliminating the need for a large opening angle). These approaches generally appear more promis-

ing for optical quantum information applications, particularly with the increasing availability of efficient telecom-wavelength detectors. In the process of characterizing and improving our source, we developed and tested several useful methods for measuring spectral correlations. Correlation function measurements were particularly helpful due to the relative simplicity of the measurement. The techniques we explored can be applied to the characterization of other sources.

7.2 Detectors

Our work with visible light photon counters has also, in a sense, served as a proof of principle. We employed careful optimization to a device designed for high-energy applications, demonstrating a quantum efficiency of 91%. This is sufficient to make the VLPC an attractive option for experiments where photon-number resolution and quantum efficiency are critical, such as an on-demand Fock-state source.

While the VLPC does not yet exist in a turn-key system, they are easier to operate than other ultra-high QE detectors like transition-edge sensors. Our system is a working prototype, and could be made more robust with improved optical and electrical isolation. Our characterization of the behavior of VLPCs could also assist with the design of new VLPC-based devices, specifically optimized for quantum information applications.

7.3 Final Thoughts

You’ve been very patient, dear reader, and now we’ve reached the end. But does it all mean anything? Does it all tie together? Did we really do anything interesting? Let’s take a step back and get some perspective.

In 1948, Claude Shannon published *A Mathematical Theory of Communication*, simultaneously establishing the field of information theory and solving many of the new field’s most interesting problems. At the same time (and in the same building!), the first experiments were being performed with the transistor. However, the transistor was little more than an interesting amplifier until after the 1954 development of the more commercially viable silicon transistors. Through a long process of incremental improvements, this technology and the theoretical framework of information theory laid the groundwork for the digital revolution of the last three decades.

The birth of quantum information is more difficult to pin down, but David Deutsch’s 1985 formulation of a universal quantum computer based on the classical Turing machine is a reasonable place to start

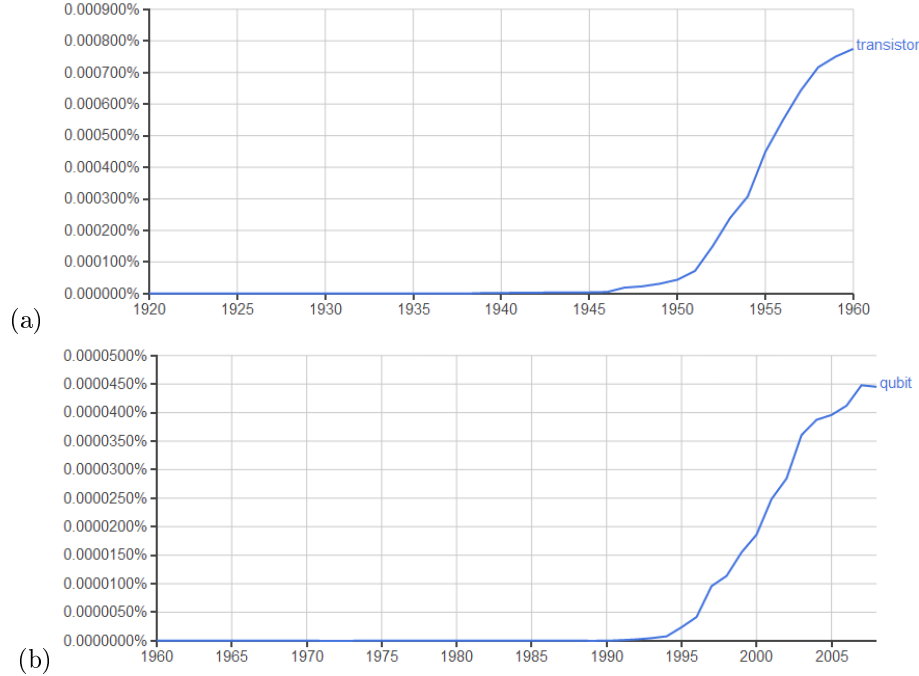


Figure 7.1: Word frequency as a percentage of words in published works from Google Ngram viewer for (a) transistor and (b) qubit.

[78].¹ Around this time, too, the experimental tools of quantum optics were being developed, with Hong and Mandel producing and measuring a single photon state in 1986 [17]. Today, experiments that were once landmark demonstrations of fundamental quantum properties are now commonplace components of increasingly more complex and involved quantum information schemes. Quantum cryptography systems are commercially available (but limited in range), and attempts have been made to commercialize an adiabatic quantum computer.²

While it is interesting to examine the parallels of these similar fields, it would be irresponsible to say that this implies that we are on the cusp of a “quantum revolution” in which quantum information will have as much impact on technology relative to classical information as the transistor had relative to the vacuum tube. In a sense, we are in a similar position to Donald Fink, who quipped of the transistor in 1953, “Is it a pimply adolescent, now awkward, but promising future vigor? Or has it arrived at maturity, full of languor, surrounded by disappointments?” [81]. In 1953, the promise of the transistor was clearly evident, but its various shortcomings also seemed potentially insurmountable. Similarly, today, we can be optimistic and look towards potential future applications enabled by wide-spread use of quantum computing. For example,

¹Other important early developments include Holevo’s 1973 description of the information content of a quantum channel [79], Feynman’s 1981 proposal of a quantum computer for simulating quantum systems [80], Bennett and Brassard’s 1984 quantum cryptography proposal [5], and Shor’s 1994 factoring algorithm [11].

²I’m referring of course to D-Wave, which may or may not have a computer that exploits quantum effects, but almost certainly does not at present have a product that offers any advantage over a classical computer other than novelty.

could Feynman's dream of quantum simulation lead to discovery of new material properties, solving key problems in room-temperature superconductivity, nuclear fusion or space flight? It's possible, but also none of this may happen: the development of the qubit need not mirror the development of the bit. The problems of scaling a quantum information system may prove too daunting. Or even if achieved, it just might not be as useful as we hope. We could be stuck with disappointments.

That sounds depressing, so why do we bother? Why spend years pushing the limits of sources and detectors of non-classical light? To loosely paraphrase Kennedy, we choose to do these things not because we know they will work, but because we don't. Not because they are straightforward, but because they are interesting. This is the peculiar realm of academic science: we take on projects that sometimes appear too speculative, too big, too uncertain. In the best case, we hope to change the world. But even falling short of that, we still learn something, about the universe, and about ourselves.

Appendix A

Dispersion Effects

A.1 Introduction to Dispersion

Dispersion describes the variation of index of refraction as a function of wavelength that is seen in most optical media: The index of refraction depends on the interaction between the electromagnetic field and the optical medium, and this interaction varies with wavelength. Though this sounds like a somewhat esoteric property, it is the same everyday effect that separates colors of white light in a prism or a rainbow. Dispersion in the eye also affects human vision, as seen¹ in Fig. A.1.

Dispersion in a typical optical medium is described quite well by the Sellmeier equation

$$n^2(\lambda) = 1 + \sum_{i=1}^N \frac{B_i \lambda^2}{\lambda^2 - C_i}, \quad (\text{A.1})$$

where the constants are determined empirically. The general form of this equation can be determined by analyzing the oscillation of the charge distribution in a medium driven by an electric field; see for example the more complete description of dispersion given in Chapter 3 of Hecht [46]. Roughly, the B_i correspond to polarizability, and the C_i to an absorption resonance peak for each of N resonance wavelengths. In a typical optical material, the visible region of the spectrum is not near resonance, and the index of refraction is monotonically decreasing with wavelength. This is referred to as normal dispersion. The opposite effect, anomalous dispersion, occurs near the absorption region in typical materials, or can be engineered in a structured material or system (see Sec. A.4).

One can additionally quantify the behavior of a dispersive medium using a Taylor expansion of the spectral phase [82]. In this Appendix, we are primarily concerned with the second-order effect, group velocity dispersion (GVD), which is given in terms of the second derivative of $n(\lambda)$ as

$$\text{GVD} = \frac{\lambda^3}{2\pi c^2} \frac{d^2 n(\lambda)}{d\lambda^2}. \quad (\text{A.2})$$

¹Literally!

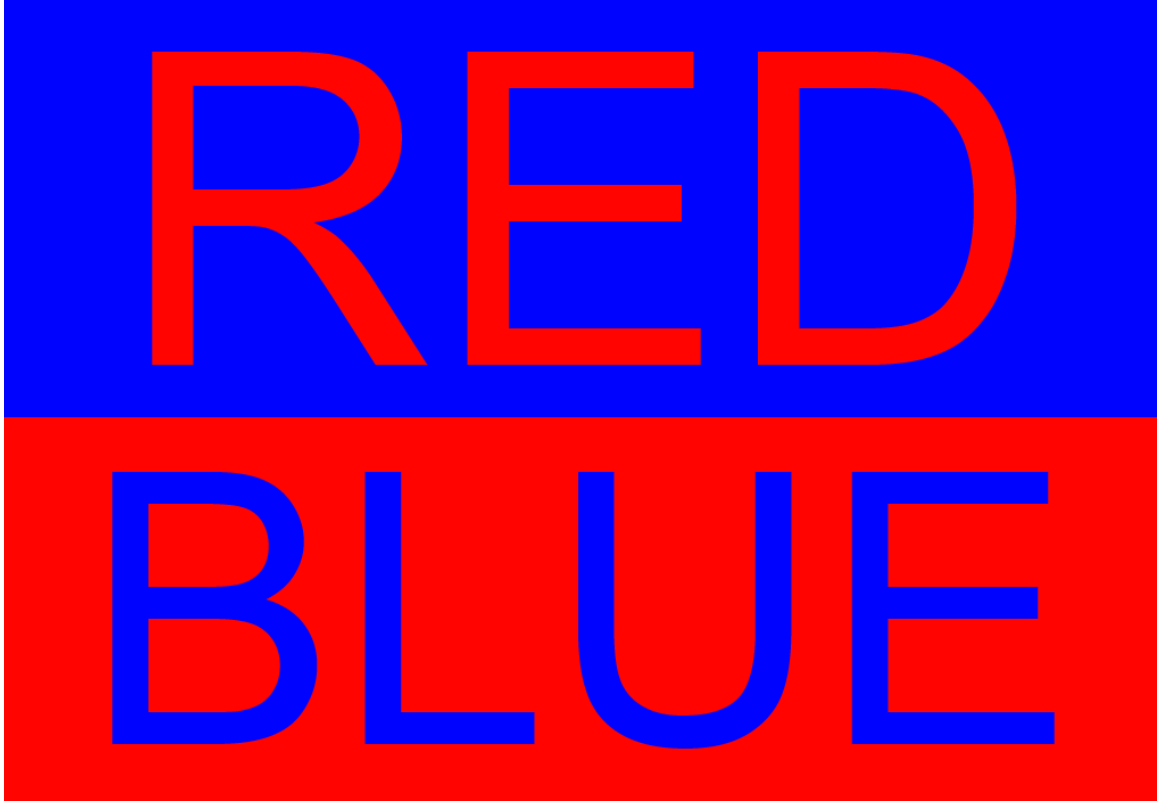


Figure A.1: Demonstration of dispersion in the eye. The red letters appear to be slightly in front of the blue background, while the blue letters appear to be slightly inset behind the red background.

GVD accumulates proportional to the length L of dispersive material, and the total quantity, group-delay dispersion (GDD), is defined as $\text{GDD} = L \times \text{GVD}$.² Higher derivatives give higher order dispersive terms, such as third-order dispersion (TOD), fourth-order dispersion, and so on. As we will see in the following section, GDD has a significant impact on the temporal profile of an ultrashort pulse.

A.2 Transform-Limited Pulses

It is often useful to characterize a short pulse in terms of the (complex-valued) temporal envelope $f(t)$ and its Fourier transform, the frequency envelope $\tilde{f}(\nu)$. The frequency or time envelope describes the amplitude and relative phase of the electric field as a function of frequency or time, respectively, such that (at a given spatial position)

$$E(t) = \frac{1}{2}f(t)e^{2\pi i\nu t} + c.c., \quad (\text{A.3})$$

²In fiber optics, dispersion is often quantified instead by the dispersion parameter $D = -\frac{\lambda}{c} \frac{d^2 n}{d\lambda^2}$. This has units of, e.g., ps/(nm km), representing relative time delay in ps for two pulses differing in wavelength by 1 nm and traveling through 1 km of optical fiber. Note that this has the opposite sign of GVD, which is why the terms normal and anomalous dispersion are preferred rather than positive and negative dispersion.

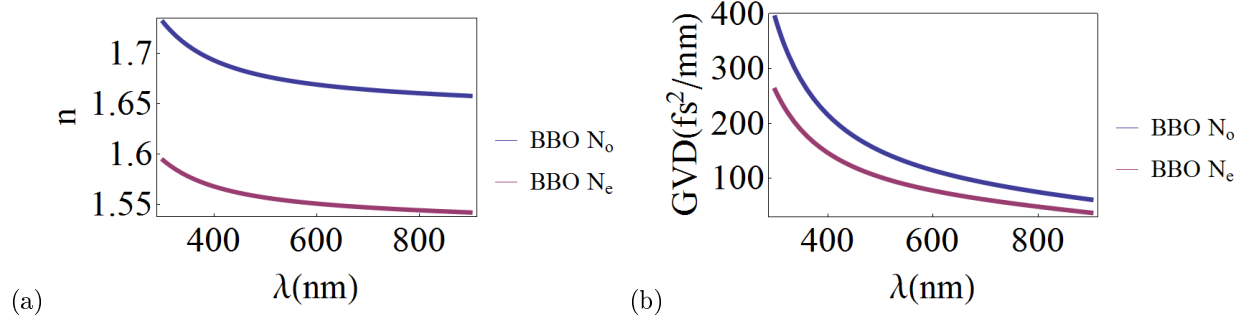


Figure A.2: (a) Dispersion curve from Sellmeier equation for ordinary and extraordinary polarization in β -BBO. (b) Resulting group velocity dispersion (GVD), proportional to the second derivative of $n(\lambda)$.

Gaussian	$\delta\nu\delta t \geq \frac{2\log 2}{\pi}$	≈ 0.4413
Hyperbolic Secant	$\delta\nu\delta t \geq \left(\frac{2\log(1+\sqrt{2})}{\pi}\right)^2$	≈ 0.3148
Lorentzian	$\delta\nu\delta t \geq \frac{2\log(2\sqrt{\sqrt{2}-1})}{\pi}$	≈ 0.142

Table A.1: Minimum time-bandwidth products for various pulse shapes.

where the electric field has been decomposed into an envelope and a carrier wave. When trying to minimize pulse duration, the Fourier transform relation between $f(t)$ and $\tilde{f}(\nu)$ determines the minimum “transform-limited” pulse duration for a given bandwidth. An infinitesimally short pulse, for example, can only be obtained with an infinitely broad frequency bandwidth, and vice-versa. We can quantify this using the time-bandwidth product $\delta\nu\delta t$, where δt and $\delta\nu$ are the FWHM (full width at half maximum) of $|f(t)|^2$ and $|\tilde{f}(\nu)|^2$, respectively. This product has the flavor of an uncertainty relation, but is a purely classical effect that depends on the shape of the pulse. The minimum time-bandwidth product for a given pulse shape is achieved when the phase of $f(t)$ is flat (i.e., independent of time), and can be calculated straightforwardly from the Fourier transform. Minimum time-bandwidth products for some common pulse shapes are shown in Table A.1.

It can be useful to write the time-bandwidth product in terms of wavelength; starting with $\delta\nu$, we have

$$\delta\nu = \left(\bar{\nu} + \frac{\delta\nu}{2}\right) - \left(\bar{\nu} - \frac{\delta\nu}{2}\right) \quad (\text{A.4})$$

$$= \frac{c}{\lambda_+} - \frac{c}{\lambda_-}, \quad (\text{A.5})$$

where $\bar{\nu}$ is the center frequency of $\tilde{f}(\nu)$ and

$$\lambda_{\pm} = c / \left(\bar{\nu} \pm \frac{\delta\nu}{2} \right) \quad (\text{A.6})$$

$$= \frac{c}{\bar{\nu}} \left(\frac{1}{1 \pm \frac{\delta\nu}{2\bar{\nu}}} \right), \quad (\text{A.7})$$

with λ_+ and λ_- corresponding to the upper and lower half-maximum of \tilde{f} . If we then solve for $\delta\nu$ we obtain

$$\delta\nu = \frac{-2c\bar{\lambda}^2 - 2\sqrt{c^2\bar{\lambda}^2(\delta\lambda^2 + \bar{\lambda}^2)}}{\delta\lambda\bar{\lambda}^2}. \quad (\text{A.8})$$

Since this is somewhat unwieldy, we could alternatively Taylor-expand Eq. A.7 in terms of $\delta\nu/2\bar{\nu}$ to second order, which gives

$$\lambda_{\pm} \approx \frac{c}{\bar{\nu}} \left(1 \pm \frac{\delta\nu}{2\bar{\nu}} + \left(\frac{\delta\nu}{2\bar{\nu}} \right)^2 \right). \quad (\text{A.9})$$

So, applying $\delta\lambda \equiv \lambda_+ - \lambda_-$ and $\bar{\nu} = c/\bar{\lambda}$,

$$\delta\lambda \approx \frac{\bar{\lambda}^2 \delta\nu}{c}, \quad (\text{A.10})$$

or, in terms of $\delta\nu$ ³

$$\delta\nu \approx \frac{c\delta\lambda}{\bar{\lambda}^2}. \quad (\text{A.11})$$

Thus, the time-bandwidth product for a Gaussian pulse can be written in terms of wavelength as

$$\delta t \delta\lambda \gtrsim \frac{0.4413\bar{\lambda}^2}{c}. \quad (\text{A.12})$$

The transform limit is just a lower-bound; a pulse with a given spectrum can have an arbitrarily long temporal profile. Dispersion is a common cause of temporal profile broadening in ultrafast optics, as dispersive effects in bulk optics become increasingly significant for the broad bandwidths involved in ultrashort pulses. Since short wavelengths are delayed more than long wavelengths, a short pulse will become spread out in time in a “chirped” manner, with long wavelength components arriving before short wavelength components. This is illustrated in Fig. A.3. GDD is often the dominant contribution to chirp. The calculated pulse broadening due to this effect is shown in Fig. A.4. The following two sections discuss how temporal profiles are measured for ultrafast pulses (Sec. A.3), and how dispersive effects can be compensated (Sec. A.4).

³We would obtain the same relationship by noting that $\nu = c/\lambda$ and so $d\nu/d\lambda = c/\lambda^2$. However, as we show, this is only correct in the limit of small bandwidth; Eq. A.8 gives the exact relationship.

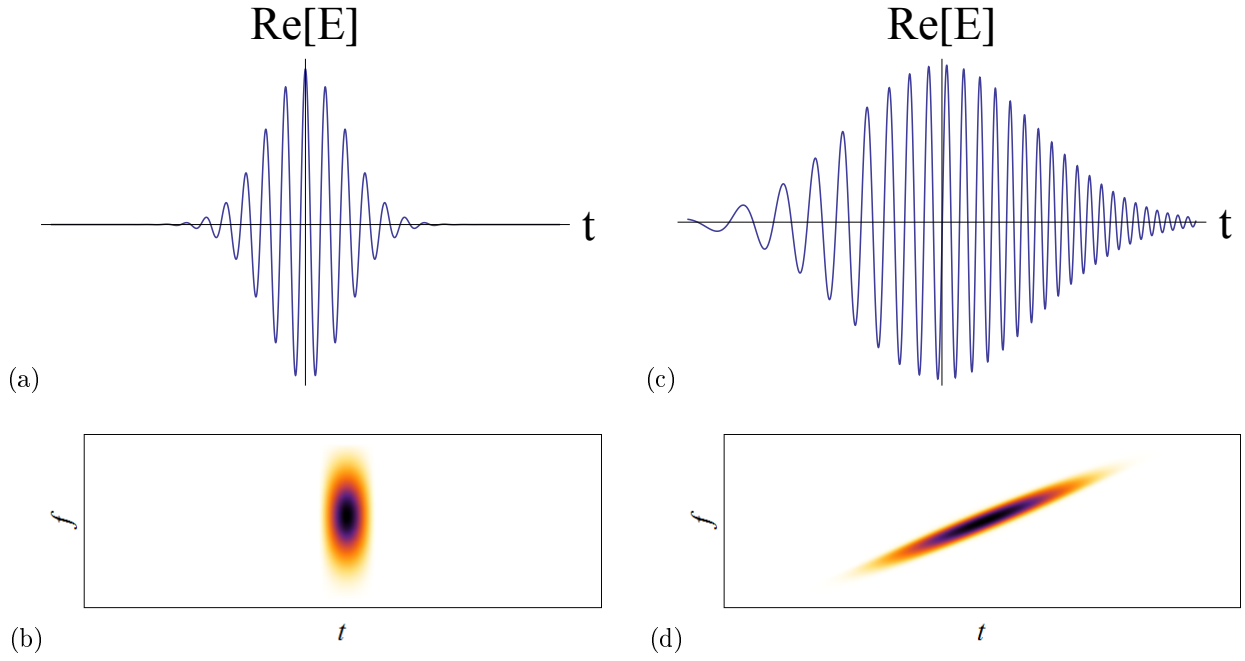


Figure A.3: (a) Electric field and (b) spectrogram for a transform-limited Gaussian pulse, and (c-d) a temporally chirped pulse. For the transform-limited pulse, the frequency is constant across the pulse, while in the chirped pulse there is a spectral gradient across the pulse.

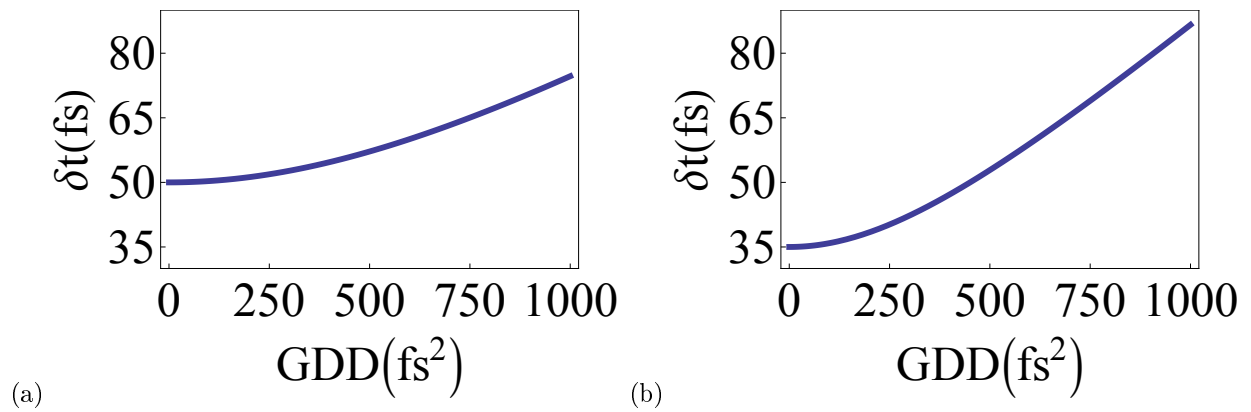


Figure A.4: Pulse broadening effect of dispersion as a function of group delay dispersion (GDD) on (a) a 50-fs transform-limited pulse and (b) a 35-fs transform-limited pulse. Shorter pulses have broader spectral bandwidths, and thus are more susceptible to dispersive effects.

A.3 Temporal Profile Measurement

A.3.1 Autocorrelation

The broad bandwidths encountered in ultrafast optics result in an easily measured frequency envelope $|\tilde{f}(\nu)|$ and bandwidth $\delta\nu$. However, the time-domain measurement is much more difficult. Typically, fast events are measured by comparing them with even faster events: a runner with the ticks of a clock, a clock tick with oscillations of a quartz resonator, and so on. But an ultrashort pulse of light is one of the fastest things we know how to controllably produce, so what to compare it with? The only answer is to compare it with itself, and this is the heart of autocorrelation.

A standard autocorrelator, shown in Fig. A.5(a), splits a pulse into two components which acquire a relative time offset, and then are combined in a nonlinear medium. At first glance, it might appear that an interferometer would be sensitive to pulse duration, as it involves two copies of a pulse with a variable time delay. However, as we saw in Sec. 3.2, this is in fact a Fourier spectrometer, and is sensitive to the spectrum, not the temporal profile, of a pulse. In the example of Fig. A.3, the two pulses shown have approximately equal spectra, despite having significantly different temporal profiles.

For this reason, autocorrelation is sometimes referred to as intensity autocorrelation, as it requires a nonlinear effect which is proportional to the intensity of the signal. This is typically provided by second-harmonic generation. However, this breaks down for UV pulses, where second-harmonic generation crystals are not available. Instead, to measure the temporal profile of our doubled 405 nm pulses, we use two-photon absorption in a silicon carbide (SiC) photodiode. This material has broad-band absorption above a bandgap of 3.23 eV. Our doubled light has an average energy per photon of 3.06 eV, and a maximum of approximately 3.14 eV, so direct absorption is expected to be minimal. Instead, the dominant excitation mechanism is two-photon absorption, so we should measure a photodiode output current proportional to the square of the input intensity. This is confirmed in Fig. A.6(a), which compares the output of a transimpedance amplifier (which converts the current output of the photodiode to voltage) to the optical power direct at the photodiode. We observe a power law dependence between optical power and photodiode current with an exponent of 1.79 ± 0.05 , clearly demonstrating a nonlinear effect. Using a piezoelectric stage, we were able to use this effect to construct a simple UV autocorrelator.

A.3.2 FROG

Frequency-Resolved Optical Gating (FROG) [84] is an extension of autocorrelation which measures an additional degree of freedom, and thus provides a more complete measurement of the electric field. The basic

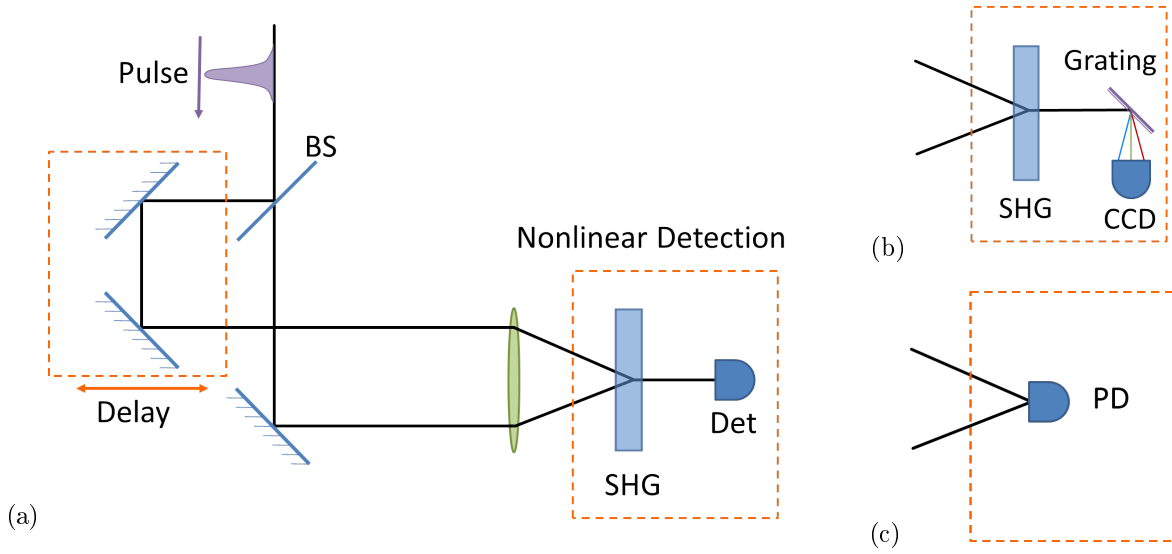


Figure A.5: Schematic of autocorrelation. A typical autocorrelation measurement involves splitting a pulse into two paths on a beamsplitter, then scanning a relative delay between the paths before recombining them on a nonlinear medium. Options for nonlinear detection include (a) second-harmonic generation (SHG) in a $\chi^{(2)}$ -nonlinear crystal, (b) SHG followed by a grating spectrometer (see Sec. A.3.2) and (c) two-photon absorption in a photodiode.

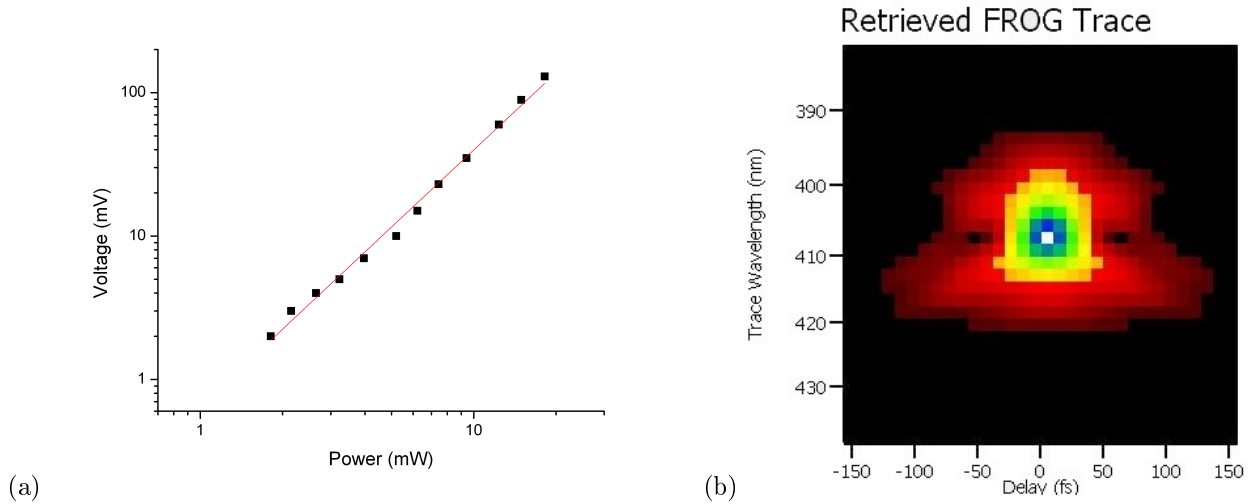


Figure A.6: Autocorrelation-related measurements. (a) Plot of photodiode voltage vs optical power, demonstrating two-photon absorption in a SiC photodiode at 405 nm. The slope of 1.79 ± 0.05 on the log-log plot clearly indicates a nonlinear effect. (b) FROG trace measured by Swamp Optics GRENOUILLE, showing the wavelength-time spectrogram of a 35-fs FWHM, 40-nm FWHM pulse train from our Tsunami Ti-Sapph laser. The central wavelength of the pulse is 810 nm, while the FROG trace displays the SHG-doubled wavelength of 405 nm. The data correspond to a time-bandwidth product of 0.632.

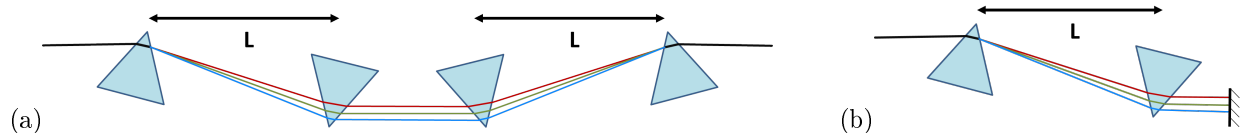


Figure A.7: (a) Prism compressor using a set of four prisms to provide anomalous dispersion. Due to refraction, longer wavelengths follow a longer optical path-length (as they travel significantly farther within the central prisms). (b) A “folded” two-prism compressor can provide the same negative dispersion as the four-prism scheme. The mirror on the right is angled slightly into the page so another mirror (not shown) can pick off the reflected beam. In both designs, the amount of anomalous dispersion can be controlled by varying the prism separation L .

schematic is an extension of the autocorrelator, except instead of an intensity detector measuring the SHG-output, there is a spectrometer (see Fig. A.5(c)). This allows the direct construction of a spectrogram, shown in Fig. A.6(b). This method, however, is only one of many related FROG measurement schemes, which have various advantages and disadvantages that are outside the scope of this work. We use a Swamp Optics GRENOUILLE⁴ to characterize our Tsunami Ti-Sapph laser, as well as to optimize the dispersion compensation. This device avoids moving parts, beamsplitters, and optical gratings using a clever arrangement of cylindrical lenses, a Fresnel biprism, and a thick SHG crystal.

A.4 Prism Compression

Having a transform-limited pulse is often desirable, but dispersive optics can be unavoidable. Thus, we would like to be able to “correct” a chirped pulse by compensating with dispersion in the opposite direction. Unfortunately, typical materials have *normal* dispersion, sharing the property that short wavelengths travel more slowly than long wavelengths, that is,

$$\frac{dn}{d\lambda} < 0. \quad (\text{A.13})$$

This dispersion accumulates, and can only be compensated by optical elements with *anomalous* dispersion,

$$\frac{dn}{d\lambda} > 0. \quad (\text{A.14})$$

Anomalous dispersion can be obtained in practice by constructing a system in which the longer wavelengths follow a longer optical pathlength. This is typically accomplished using diffraction in gratings, reflection in a dielectric stack in a mirror, or refraction in prisms. We employ this last technique, the prism compressor [85], shown in Fig. A.7. The exact analysis of the prism compressor would be superfluous here, as it is

⁴Grenouille is the French word for frog, and in a rather strained abbreviation, stands for GRating-Eliminated No-nonsense Observation of Ultrafast Incident Laser Light E-fields.

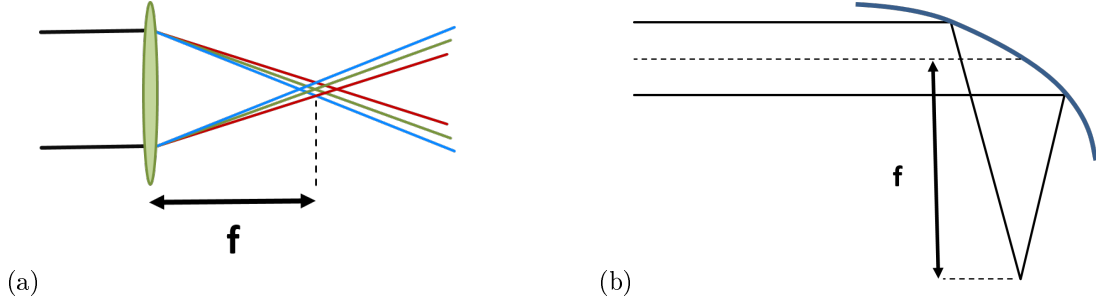


Figure A.8: (a) Chromatic aberration due to dispersion in a glass lens. (b) Parabolic mirror with no dispersive elements, focusing at 90° off-axis.

covered extensively in other sources; of particular practical use is Newport Application Note 29, which includes conveniently tabulated values of dispersion for various wavelengths, types of glass, and prism pair separations [82].

A.5 Doubling $810 \rightarrow 405$ nm

As described in Chapter 2, our source is designed for downconversion of 405-nm pump photons into pairs of 810-nm photons. In particular, the engineered source relies on a pump capable of producing extremely short (femtosecond-scale) pulses at 405 nm. Unfortunately, a source with these capabilities is not commercially available. Instead, we use a mode-locked Ti:Sapph to generate pulses at 810 nm, which we then frequency-double via SHG to the desired 405 nm.

Doubling ultrashort pulses is a double-edged sword. On one hand, because SHG conversion efficiency scales with instantaneous intensity,⁵ ultrashort pulses are desirable for concentrating pulse energy into a short time. On the other hand, the short pulse lengths and broad bandwidths involved complicate the doubling process. For example, for efficient doubling of ultrashort pulses, we require *two* prism compressors: one to compensate dispersion in the 810-nm pump immediately before doubling, and a second to compensate the doubled 405-nm light before SPDC. Additionally, one must use care in selecting lenses for focusing into the SHG crystal, as well in choosing the thickness of the SHG crystal.

A.5.1 Lens Selection

Since doubling efficiency scales with optical power, we would like to further enhance our SHG conversion by focusing to a small spot in the SHG crystal. This too is complicated by our source's broad spectral

⁵In the approximation of a non-depleted pump, SHG efficiency is proportional to the square of the intensity of the pump. Eventually, nearly all of the pump energy will convert to the doubled frequency, and then downconvert back to the original frequency. This is not encountered in our source, and pump non-depletion remains a reasonable approximation.

Wavelength	810 nm (30-nm FWHM bandwidth)		405 nm (10-nm FWHM bandwidth)	
Lens Type	Achromat	Plano-convex	Achromat	Plano-convex
Thorlabs Part #	AC127-025-B	LA4647-B	AC127-050-A	LA4148-A
Δ Focal Length (μm)	1	20	41	106
Δ Path Length (μm)	7	2	33	6

Table A.2: Comparison of focal plane shift (due to chromatic aberration) and optical path-length difference (due to dispersion) for achromatic and plano-convex lenses. Numerical values were obtained from Zemax by David Schmid, and refer to the difference in the focal plane position or optical path length difference between light on the high and low end of the corresponding bandwidth. Bandwidths were chosen based on typical values for our source.

bandwidth. The focal length of a simple glass lens depends on its index of refraction, which as we’ve seen, can vary appreciably with wavelength (see Fig. A.8(a)). Fortunately, lenses which reduce this effect are readily available: these achromatic doublets are constructed from different types of glass, which act together to minimize the focal plane shift experienced by light of different colors. However, this comes at a cost: achromatic doublets use more glass, which adds more dispersion, further distorting the *temporal* profile of the pulse. Because we suspected that additional dispersion was compromising the quality of our source, we tried switching from achromatic doublets to plano-convex lenses. However, the purity of the resulting single-photon states actually decreased, likely due to the chromatic focusing aberration. Also, doubling efficiency was severely reduced relative to achromatic doublets (approximately 40 mW vs 120 mW, for a 600 mW pump).

Some trade-off between dispersion and chromatic aberration is unavoidable for glass lenses (see Tab. A.2). Thus, we eventually switched to parabolic mirrors, which achieve focusing by reflection from a curved surface, shown in Fig. A.8(b). This lens design contains no dispersive elements and thus performs the same focusing on all wavelengths, but it is much more sensitive to alignment.

With parabolic mirrors, we were able to achieve even higher doubling efficiency than with achromatic doublets, though without further improvement in the heralded single-photon purity. With proper dispersion compensation and lens selection, we are able to achieve a doubling efficiency of over 20%, converting approximately 600 mW of 810-nm light to 140 mW of 405-nm light.

A.5.2 Crystal Thickness

We want tight focusing for efficient doubling, but this also comes with a trade-off. SHG must conserve energy and momentum between the pump and doubled photons, analogous to the SPDC phasematching conditions described in Chapter 2. Tight focusing complicates this, as it increases the spread of \mathbf{k} -vectors over which phase-matching must hold. If focusing is too tight, the extremal \mathbf{k} -vectors will not support phase-matching

across the entire spectral bandwidth. This can be compensated by simply focusing less tightly, or by choosing a shorter crystal to relax the longitudinal phase-matching constraint. Short SGH crystals are also desirable because dispersion in the crystal leads to different group velocities for different wavelengths, causing the pump and doubled light to “walk off” from each other temporally while propagating through the crystal. In our system, we focus to an approximately $15\text{-}\mu\text{m}$ spot in a $200\text{-}\mu\text{m}$ β -BBO crystal for SHG.

References

- [1] P. G. Kwiat. [Ph.D. thesis](#), University of California at Berkeley, United States – California (1993).
- [2] P. G. Kwiat, *et al.* Proposal for a loophole-free Bell inequality experiment. *Physical Review A*, [49\(5\):3209–3220](#) (1994). ISSN 1094-1622.
- [3] C. H. Bennett, *et al.* Teleporting an unknown quantum state via dual classical and Einstein-Podolsky-Rosen channels. *Phys. Rev. Lett.*, [70:1895–1899](#) (1993).
- [4] D. Bouwmeester, *et al.* Experimental quantum teleportation. *Nature*, [390\(6660\):575–579](#) (1997). ISSN 0028-0836.
- [5] C. H. Bennett, G. Brassard, *et al.* Quantum cryptography: Public key distribution and coin tossing. In *Proceedings of IEEE International Conference on Computers, Systems and Signal Processing*, vol. 175, p. 8. New York (1984).
- [6] A. K. Ekert. Quantum cryptography based on Bell’s theorem. *Phys. Rev. Lett.*, [67\(6\):661–663](#) (1991). ISSN 0031-9007.
- [7] A. Barenco, *et al.* Conditional Quantum Dynamics and Logic Gates. *Phys. Rev. Lett.*, [74\(20\):4083–4086](#) (1995). ISSN 1079-7114.
- [8] E. Knill, R. Laflamme, and G. J. Milburn. A scheme for efficient quantum computation with linear optics. *Nature*, [409\(6816\):46–52](#) (2001). ISSN 0028-0836.
- [9] N. Gisin, *et al.* Quantum cryptography. *Rev. Mod. Phys.*, [74\(1\):145–195](#) (2002). ISSN 1539-0756.
- [10] M. A. Nielsen and I. L. Chuang. *Quantum Computation and Quantum Information (Cambridge Series on Information and the Natural Sciences)*. Cambridge University Press (2000). ISBN 0521635039.
- [11] P. W. Shor. Polynomial-Time Algorithms for Prime Factorization and Discrete Logarithms on a Quantum Computer. *SIAM Review*, [41\(2\):303–332](#) (1999). ISSN 1095-7200.
- [12] W. P. Grice, A. B. U’ren, and I. A. Walmsley. Eliminating frequency and space-time correlations in multiphoton states. *Physical Review A*, [64\(6\):63815](#) (2001). ISSN 1094-1622.
- [13] A. B. U’Ren, K. Banaszek, and I. A. Walmsley. Photon engineering for quantum information processing. *Journal of Quantum Information and Computation*, [3:480–502](#) (2003).
- [14] C. K. Hong and L. Mandel. Theory of parametric frequency down conversion of light. *Phys. Rev. A*, [31:2409–2418](#) (1985).
- [15] R. Rangarajan. [Ph.D. thesis](#), University of Illinois at Urbana-Champaign, United States – Illinois (2010).
- [16] R. W. Boyd. *Nonlinear Optics, Second Edition*. Academic Press (2003). ISBN 0121216829.
- [17] C. Hong and L. Mandel. Experimental realization of a localized one-photon state. *Phys. Rev. Lett.*, [56\(1\):58–60](#) (1986). ISSN 0031-9007.

- [18] C. K. Hong, Z. Y. Ou, and L. Mandel. Measurement of subpicosecond time intervals between two photons by interference. *Phys. Rev. Lett.*, **59**(18):2044–2046 (1987). ISSN 1079-7114.
- [19] H.-J. Briegel, *et al.* Quantum Repeaters: The Role of Imperfect Local Operations in Quantum Communication. *Phys. Rev. Lett.*, **81**:5932–5935 (1998).
- [20] L.-M. Duan, *et al.* Long-distance quantum communication with atomic ensembles and linear optics. *Nature*, **414**(6862):413–418 (2001).
- [21] Z. Zhao, *et al.* Experimental Realization of Entanglement Concentration and a Quantum Repeater. *Phys. Rev. Lett.*, **90**(20) (2003).
- [22] W. K. Wootters and W. H. Zurek. A single quantum cannot be cloned. *Nature*, **299**(5886):802–803 (1982).
- [23] K. Mattle, *et al.* Dense Coding in Experimental Quantum Communication. *Phys. Rev. Lett.*, **76**(25):4656–4659 (1996).
- [24] J.-W. Pan, *et al.* Experimental Entanglement Swapping: Entangling Photons That Never Interacted. *Physical Review Letters*, **80**(18):3891–3894 (1998). ISSN 1079-7114.
- [25] J. S. Bell. On the problem of hidden variables in quantum mechanics. *Reviews of Modern Physics*, **38**(3):447–452 (1966). ISSN 1539-0756.
- [26] J. F. Clauser, *et al.* Proposed experiment to test local hidden-variable theories. *Phys. Rev. Lett.*, **23**(15):880–884 (1969). ISSN 1079-7114.
- [27] G. Weihs, *et al.* Violation of Bell’s inequality under strict Einstein locality conditions. *Phys. Rev. Lett.*, **81**(23):5039–5043 (1998). ISSN 1079-7114.
- [28] R. H. Hadfield. Single-photon detectors for optical quantum information applications. *Nature Photonics*, **3**(12):696–705 (2009). ISSN 1749-4885.
- [29] A. E. Lita, A. J. Miller, and S. W. Nam. Counting near-infrared single-photons with 95% efficiency. *Opt. Express*, **16**(5):3032–3040 (2008). ISSN 1094-4087.
- [30] D. Fukuda, *et al.* Titanium-based transition-edge photon number resolving detector with 98 Optics Express, **19**(2):870 (2011). ISSN 1094-4087.
- [31] D. Fukuda, *et al.* Photon number resolving detection with high speed and high quantum efficiency. *Metrologia*, **46**:S288 (2009).
- [32] A. J. Kerman, *et al.* Constriction-limited detection efficiency of superconducting nanowire single-photon detectors. *Appl. Phys. Lett.*, **90**(10):101110 (2009). ISSN 0003-6951.
- [33] D. Rosenberg, *et al.* High-speed and high-efficiency superconducting nanowire single photon detector array. *Optics Express*, **21**(2):1440 (2013). ISSN 1094-4087.
- [34] F. Marsili, *et al.* Detecting single infrared photons with 93% efficiency. *Nature Photonics*, **7**(3):210–214 (2013). ISSN 1749-4893.
- [35] J. Kim, *et al.* Multiphoton detection using visible light photon counter. *Appl. Phys. Lett.*, **74**:902 (1999).
- [36] J. Kim, S. Somani, and Y. Yamamoto. *Nonclassical light from semiconductor lasers and LEDs*. Springer (2001). ISBN 9783540677178.
- [37] S. Takeuchi, *et al.* Development of a high-quantum-efficiency single-photon counting system. *Appl. Phys. Lett.*, **74**:1063 (1999).

- [38] E. Waks, *et al.* High-efficiency photon-number detection for quantum information processing. Selected Topics in Quantum Electronics, IEEE Journal of, **9(6)**:1502–1511 (2004). ISSN 1077-260X.
- [39] B. Baek, *et al.* Single-photon detection timing jitter in a visible light photon counter. Quantum Electronics, IEEE Journal of, **46(6)**:991–995 (2010). ISSN 0018-9197.
- [40] J. H. Eberly. Schmidt analysis of pure-state entanglement. Laser Physics, **16(6)**:921–926 (2006).
- [41] C. K. Law, I. A. Walmsley, and J. H. Eberly. Continuous Frequency Entanglement: Effective Finite Hilbert Space and Entropy Control. Phys. Rev. Lett., **84(23)**:5304–5307 (2000).
- [42] L. E. Vicent, *et al.* Design of bright, fiber-coupled and fully factorable photon pair sources. New Journal of Physics, **12(9)**:093027 (2010). ISSN 1367-2630.
- [43] D. Branning, *et al.* Engineering the Indistinguishability and Entanglement of Two Photons. Phys. Rev. Lett., **83(5)**:955–958 (1999). ISSN 1079-7114.
- [44] A. B. U'Ren (2010). Private communication.
- [45] P. G. Kwiat, *et al.* Ultrabright source of polarization-entangled photons. Physical Review A, **60(2)**:R773 (1999).
- [46] E. Hecht. *Optics, 2nd Edition*. Addison-Wesley (1987). ISBN 020111609X.
- [47] O. Gühne and G. Toth. Entanglement detection. Physics Reports, **474(1-6)**:1–75 (2009). ISSN 0370-1573.
- [48] J. Schwinger. Unitary operator bases. Proc. Natl. Acad. Sci. U. S. A., **46(4)**:570 (1960).
- [49] M. Krenn, *et al.* Generation and confirmation of a (100× 100)-dimensional entangled quantum system. Proceedings of the National Academy of Sciences, p. 201402365 (2014).
- [50] A. Migdall. Polarization directions of noncollinear phase-matched optical parametric downconversion output. Journal of the Optical Society of America B, **14(5)**:1093 (1997). ISSN 1520-8540.
- [51] M. Avenhaus, *et al.* Fiber-assisted single-photon spectrograph. Opt. Lett., **34(18)**:2873 (2009). ISSN 1539-4794.
- [52] P. Hariharan. *Optical Interferometry*. Academic Press (2003). ISBN 0123116309.
- [53] W. Wasilewski, *et al.* Joint spectrum of photon pairs measured by coincidence Fourier spectroscopy. Opt. Lett., **31(8)**:1130–1132 (2006). ISSN 1539-4794.
- [54] W. H. Richardson. Bayesian-Based Iterative Method of Image Restoration. Journal of the Optical Society of America, **62(1)**:55 (1972). ISSN 0030-3941.
- [55] X. Zou and L. Mandel. Photon-antibunching and sub-Poissonian photon statistics. Phys. Rev. A, **41(1)**:475–476 (1990). ISSN 1094-1622.
- [56] M. Fox. *Quantum Optics: An Introduction (Oxford Master Series in Physics)*. Oxford University Press, USA (2006). ISBN 0198566727.
- [57] B. Mollow and R. Glauber. Quantum Theory of Parametric Amplification. II. Phys. Rev., **160(5)**:1097–1108 (1967). ISSN 1536-6065.
- [58] F. Paleari, *et al.* Thermal photon statistics in spontaneous parametric downconversion. Opt. Express, **12(13)**:2816–2824 (2004).
- [59] B. Blauensteiner, *et al.* Photon bunching in parametric down-conversion with continuous-wave excitation. Phys. Rev. A, **79(6)** (2009). ISSN 1094-1622.

- [60] R. Loudon. *The Quantum Theory of Light (Oxford Science Publications)*. Oxford University Press, USA (2000). ISBN 0198501765.
- [61] R. H. Brown and R. Twiss. A test of a new type of stellar interferometer on Sirius. *Nature*, **178**(4541):1046–1048 (1956).
- [62] A. Christ, *et al.* Probing multimode squeezing with correlation functions. *New Journal of Physics*, **13**(3):033027 (2011).
- [63] P. H. Eberhard. Background level and counter efficiencies required for a loophole-free Einstein-Podolsky-Rosen experiment. *Physical Review A*, **47**:747 (1993).
- [64] M. D. Eisaman, *et al.* Invited Review Article: Single-photon sources and detectors. *Review of Scientific Instruments*, **82**(7):071101 (2011). ISSN 0034-6748.
- [65] A. Migdall, *et al.* *Single-Photon Generation and Detection: Physics and Applications*. Academic Press (2013). ISBN 0123876966.
- [66] J. Kim, *et al.* Novel Semiconductor Single-Photon Detectors. In *Single-Photon Generation and Detection: Physics and Applications*, chap. 5, pp. 147–180. Academic Press (2013).
- [67] A. Bross, *et al.* Localized field reduction and rate limitation in visible light photon counters. *Appl. Phys. Lett.*, **85**(24):6025–6027 (2004).
- [68] A. Bross, *et al.* Gain dispersion in visible light photon counters as a function of counting rate. *Appl. Phys. Lett.*, **87**:214102 (2005).
- [69] G. Khoury. *Ph.D. thesis*, University of California, Santa Barbara, United States – California (2006).
- [70] C. Guiberteau, M. Le Paih, and S. Ruggeri. Sample-and-hold unit with high sampling frequency (1991). US Patent 5,017,924.
- [71] M. Petroff and M. Attac. High energy particle tracking using scintillating fibers and solid state photomultiplier. *Nuclear Science, IEEE Transactions on*, **36**(1):163–164 (1989).
- [72] M. Atac, *et al.* Scintillating fiber tracking for the SSC using visible light photon counters. *Nuclear Instruments and Methods in Physics Research Section A: Accelerators, Spectrometers, Detectors and Associated Equipment*, **314**(1):56–62 (1992).
- [73] D. Adams, *et al.* First large sample study of visible light photon counters (VLPC’s). *Nuclear Physics B-Proceedings Supplements*, **44**(1):340–348 (1995).
- [74] P. Kwiat, *et al.* High-efficiency single-photon detectors. *Phys. Rev. A*, **48**(2):R867–R870 (1993). ISSN 1094-1622.
- [75] J. Kim, *et al.* Opportunities for single-photon detection using visible light photon counters. In *SPIE Defense, Security, and Sensing*, pp. 80330Q–80330Q. International Society for Optics and Photonics (2011).
- [76] J. B. Spring, *et al.* On-chip low loss heralded source of pure single photons. *Optics Express*, **21**(11):13522 (2013). ISSN 1094-4087.
- [77] P. G. Evans, *et al.* Bright Source of Spectrally Uncorrelated Polarization-Entangled Photons with Nearly Single-Mode Emission. *Physical Review Letters*, **105**(25) (2010). ISSN 1079-7114.
- [78] D. Deutsch. Quantum Theory, the Church-Turing Principle and the Universal Quantum Computer. *Proceedings of the Royal Society A: Mathematical, Physical and Engineering Sciences*, **400**(1818):97–117 (1985). ISSN 1471-2946.
- [79] A. S. Holevo. Bounds for the quantity of information transmitted by a quantum communication channel. *Problemy Peredachi Informatsii*, **9**(3):3–11 (1973).

- [80] R. P. Feynman. Simulating physics with computers. *Int J Theor Phys*, **21(6-7):467–488** (1982). ISSN 1572-9575.
- [81] Science: Problem Child. *Time* (1953).
- [82] Newport Corporation. *Newport Application Note 29: Prism Compressor for Ultrashort Laser Pulses* (2006).
- [83] D. Reid, *et al.* Commercial Semiconductor Devices for Two Photon Absorption Autocorrelation of Ultrashort Light Pulses. *Appl. Opt.*, **37(34):8142** (1998). ISSN 1539-4522.
- [84] R. Trebino. *Frequency-Resolved Optical Gating: The Measurement of Ultrashort Laser Pulses*. Springer (2002). ISBN 1402070667.
- [85] R. L. Fork, O. E. Martinez, and J. P. Gordon. Negative dispersion using pairs of prisms. *Opt. Lett.*, **9(5):150** (1984). ISSN 1539-4794.